UNIVERSITY OF GENOA

PHYSICS DEPARTMENT

Ph.D. IN PHYSICS

CHARGE AND HYDROPHOBICITY EFFECTS AT NANO–BIO INTERFACES

SEBASTIAN SALASSI

Supervisor: Dr. Giulia Rossi

Genoa, March 2020

Curiously enough, the only thing that went through the mind of the bowl of petunias as it fell was "Oh no, not again".

Douglas Adams – The Hitchhiker's Guide to the Galaxy

ABSTRACT

Gold nanoparticles coated with bio-compatible ligands are promising tools for biomedical applications due their water solubility, bio-compatibility and efficient light-to-heat conversion. In *in vivo* applications, nanoparticles come in contact with many biological molecules before being delivered to cells. The understanding of the physical and chemical nature of these different nano-bio interfaces is crucial to the rational design of nanoparticles with biomedical applications. The aim of this thesis is to understand, by molecular dynamics, how the composition, hydrophobicity and charge of the ligand shell of a small gold nanoparticle can influence its interaction with *i.* the solvent, *ii.* model biological membranes and *iii.* serum proteins. For each of these relevant interfaces we address a specific case of study.

In our first case study, we address the role of ligands during the transfer of heat from a hot irradiated gold nanoparticle to the surrounding solvent (water). Indeed, in photothermal therapies laser-irradiated resonant nanoparticles convert light into heat, which is then released to the surrounding biological tissues. Nevertheless, no clear physical interpretation is currently available to explain thermal transport at the nanoparticle surface, where a solid-liquid (metal–ligand) interface is coupled to a liquid-liquid (ligand–solvent) interface. We use computer simulations to show that thermal transport at the nanoparticle surface depends on solvent diffusivity at the ligand–solvent interface. Furthermore, using physical indicators of water confinement around hydrophobic and hydrophilic ligands, we develop a predictive model to allow engineering of nanoparticle coatings with the desired thermal conductivities at the nanoscale.

The second case study is the interaction between an anionic, monolayer-protected gold nanoparticle and a model neutral lipid membrane. The cell membrane is the first barrier that gold nanoparticles meet in cell-targeted applications. Here we show how the nanoparticle surface functionalization, and in particular its charge state, can drive the mechanism of interaction with a zwitterionic lipid membrane.

Our third case study is the interaction between a monolayer-protected gold nanoparticle and a serum protein, ubiquitin. Indeed, when nanoparticles circulate in the bloodstream, they come in contact with many serum proteins, which can irreversibly bind to nanoparticles, thus changing the surface they expose to the biological environment. We combine computer simulations and experimental results to study how the ligand charge and composition influence the interaction between nanoparticles and ubiquitin. We find that interfacial water molecules are more bound to the nanoparticles with the largest negative charge and this reflects in an increase of their hydrodynamic radius and in a slower kinetics of binding to the protein during unbiased simulations.

LIST OF PUBLICATIONS

Book chapter

1. Chapter 9: "Nanoparticle–membrane interactions: surface effects"; G. Rossi, S. Salassi, F. Simonelli, A. Bartocci and M. Monticelli; Book title: Biomembrane simulations: computational studies of biological membranes; Edited by Max L. Berkowitz; Published by CRC Press, 2019

Papers published on peer-reviewed journals

2. Anionic nanoparticle-lipid membrane interactions: the protonation of anionic ligands at the membrane surface reduces membrane disruption; S. Salassi, E. Canepa, R. Ferrando and G. Rossi; *RSC Advances*, 2019, 9, 13992-13997

3. Tailored Ag-Cu-Mg multi-element nanoparticles for wide-spectrum antibacterial coating; G. Benetti, E. Cavaliere, R. Brescia, S. Salassi, R. Ferrando, A. Vantomme, L. Pallecchi, S. Pollini, S. Boncompagni, B. Fortuni, M. Van Bael, F. Banfi and L. Gavioli; *Nanoscale*, 2018

4. A Martini coarse-grained model of the calcein fluorescent dye; S. Salassi, F. Simonelli, A. Bartocci and G. Rossi; *J. Phys. D: Appl. Phys*, 2018, *51*, 384002

5. Au Nanoparticles in Lipid Bilayer: A Comparison between Atomistic and Coarse–Grained Models; S. Salassi, F. Simonelli, D. Bochicchio, R. Ferrando and G. Rossi; *J. Phys. Chem C*, 2017, *121*, 10927–10935

Papers submitted to peer-reviewed journals

6. Controlling Thermal Transport at the Interface of Irradiated Nanoparticles: the Interplay of Surface Chemistry and Water Confinement; S. Salassi, A. Cardellini, P. Asinari, R. Ferrando and G. Rossi; *Advanced Science*

Papers in preparation

7. Anionic gold nanoparticles perturb phase separation and form ordered supramolecular aggregates in multidomain lipid membranes; E. Canepa, S. Salassi, A. L. de Marco, C. Lambruschini, D. Odino, D. Bochicchio, F. Canepa, C. Canale, S. Dante, R. Brescia, F. Stellacci, G. Rossi and A. Relini

This thesis is based on the content of papers n. 1, 2, 3, 5 and 6.

CONTENTS

LIST OF ACRONYMS

C11 undecane thiol
CG coarse grained
COM center of mass
CV collective variable
DOF degrees of freedom
FES free energy surface
FF force field
MC11 6-methyl-undecane thiol
MD molecular dynamics
MMUA 7-methyl-mercaptoundecanoic acid
MUA mercaptoundecanoic acid
MUS mercaptoundecane sulfonate
NMR nuclear magnetic resonance
NP nanoparticle
OT octanethiol
PBC periodic boundary conditions
PDB protein data bank
PEF potential energy function
PEG polyethylene glycol
pMBA para-mercaptobenzoic acid
PME particle mesh Ewald
PMF potential of mean force
POPC 1-palmitoyl-2-oleoyl-*sn*-glycero-3-phosphocholine
PW polarizable water
RDF radial distribution function
SAM self assembled monolayer
SPC/E extended simple point charge
UA united-atom
vDOS vibrational density of states

1 ENGINEERED NANOMATERIALS IN THE BIOLOGICAL ENVIRONMENT

1.1 ENGINEERED NANOMATERIALS

Nanostructures and nanomaterials are assemblies of materials with at least one dimension shorter than 100 nm. Nanomaterials diTffer considerably from the bulk materials, offering better functionality, sensitivity, efficiency and specificity in a wide range of applications. It is nowadays possible to rationally design and engineer a variety of nanomaterials, manipulating and controlling their surface properties. These human created nanomaterials with unusual and tunable properties are called *engineered nanomaterials*. Thanks to their nanoscale size and high surface to volume ratio, engineered nanomaterials exhibit unique physicochemical properties. Also, these properties are often subject to significant variation as a function of the size owing to quantum confinement effects. The optical, electronic, magnetic properties and chemical reactivities of engineered nanomaterials have attracted nowadays much interest and generated a wide variety of applications [1–5].

Recently, the investigations on engineered nanomaterials have expanded in the biological field, as they constitute a versatile platform in many biomedical applications. In particular, the small size of nanomaterials allow them to penetrate into vessels, tissues and even cells for *in vitro* and *in vivo* imaging, drug-delivery and therapy. The combination of diagnostic and therapeutic actions of these multivalent nanoagents have led to coin the term theranostic nanomaterials [6].

As recently pointed out by Karrina McNamara [7], Dong Liu [8] and Liang Yan [9], the commonly used materials to develop engineered nanoparticles (NPs) for biomedical applications are inorganic and metal or metal oxide nanoparticles, quantum dots, carbon based materials (carbon nanotubes, fullerens, nanodiamonds, graphene), liposomes, biopolymers, dendritic polymers and many others (see Figure 1). Unfortunately, many of them are inorganic materials with poor biological compatibility and stability. Biofunctions, biocompatibility and biostability are generally realized introducing an *organic functionalization* on the nanomaterial surface. Thus, surface chemistry functionalization, surface physics (topography and roughness) and surface thermodynamics (wettability and free energy) are important parameters to control the nanomaterial toxicity and optimize their nanoconstruct for its specific biomedical application.

1.1.1 Engineered nanomaterials for biomedical applications

Among the different materials that can be engineered to be used in nanomedicine, metal nanomaterials and, in particular, Au, Ag or metal oxides, have been proven a

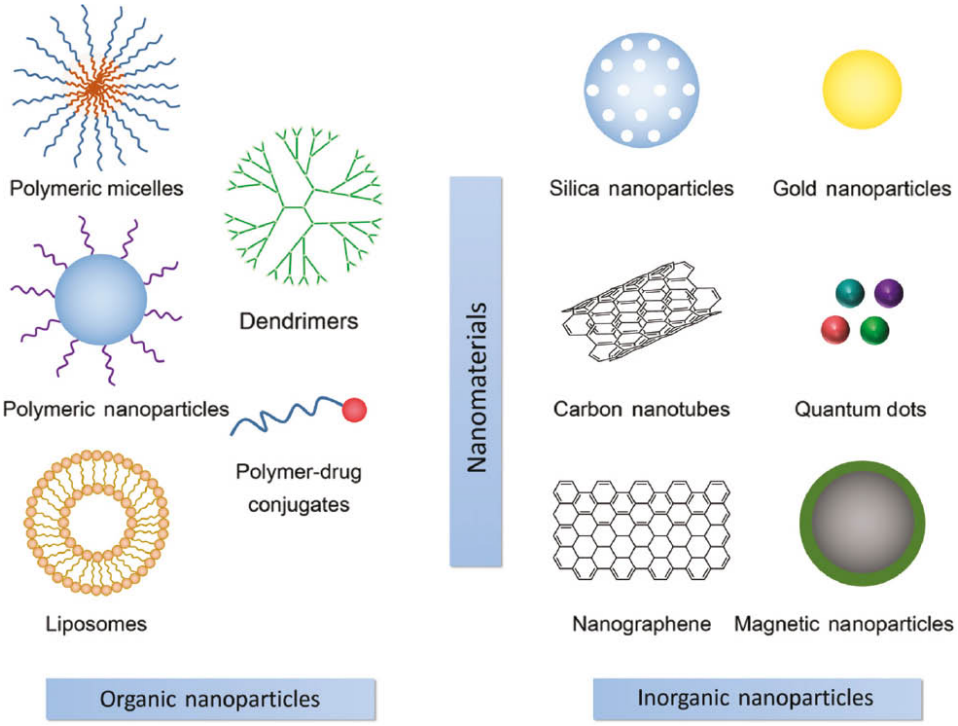

Figure 1: Representation of engineered nanomaterials, including organic and inorganic nanomaterials, applied for biomedical therapies. Taken from [6].

convenient and powerful platform due to their unique optical, physical and chemical properties. For example, the strong optical absorption at the surface plasmon resonance of metal NPs make them suitable for imaging, sensing and photothermal therapies [10]. Au nanorods or nanostars, which absorb light in the near-infrared region with high efficiency, have been used to monitor the blood flow *in vivo* using photoacoustic imaging [4]. Ag NPs have also attracted interest in the biomedical field. For example, biosensing devices are based on spectral modifications due to aggregated Ag NPs. Moreover, it is well-known the anti-bacterial activity and anti-inflammatory action of Ag NPs [11]. Metal oxide nanomaterials can also be employed as antimicrobial agents, as in the case of ZnO and CuO NPs or as drug delivery systems [12]. Moreover, the intrinsic fluorescence of ZnO nanowires, for example, has been employed to image cancer cells [13], while functionalization of the ZnO surface with specific biomolecules creates photosensitive biosensors [14]. TiO_2 NPs also show a wide range of biomedical applications. These NPs can be functionalized to achieve specific targeting and the drug load can be released upon irradiation with UV light to which TiO_2 NPs are sensitive [15]. TiO_2 NPs are also used in bone-substituting materials: the biofluid first makes contact with a thin TiO_2 layer that spontaneously emerges on the top surface of Ti [16]. This has motivated the use of TiO_2 NPs for bone regeneration. ZrO_2 has recently been used for dental implants because, like Ti, it is compatible with the same type of hard tissues [17]. Furthermore, exploiting the magnetic or superparamagnetic character of certain metal oxide NPs, such as Fe oxide NPs, it is possible to realize contrast

agents in magnetic resonance imaging, magnetic particle imaging and magnetic hyperthermia [18].

Organic NPs like polymers and liposomes can be successfully employed in biomedicine as nanocarriers to deliver water-insoluble anticancer drugs, peptides, proteins, DNA and others to the desidered site. As liposomes are potentially atoxic, degradable under physiological conditions and non-immunogenic, they can be expected to deliver drugs with a low degradation rate and diminished collateral effects. Thanks to the combination of their small size and high branching, stimuli-responsive polymeric nanomaterials such as dendrimers, polymers of branched repeated units that depart from a central core and extend outwards, are also useful for drug/gene delivery applications since they can improve the solubility and stability of encapsulated drugs, as well as their therapeutic effects due to a greater fraction of drug reaching the target site [19]. Polymer dendrimers can be use also as imaging tools. Other biomacromolecules, such as assemblies of peptides, proteins and DNA-based nanomaterials, due to their chemical versatility, biocompatibility, and biological recognition capability, have been extensively studied for biosensors, nanocarriers and bioscaffolds for tissue repair and regeneration [1, 2, 4, 7, 9].

In addition to metal/metal oxide or liposome/polimer nanomaterials, carbon based materials such as fullerenes, nanotubes or graphene are also important nanomaterials for biomedical applications. Fullerenes, graphene and their derivatives have shown to be possible candidate for biomedical applications especially for bio-sensing, imaging and drug delivery. Nevertheless, research has indicated that graphene and its derivatives (especially nanotubes) may cause aggregation and cytotoxicity in *in vitro* and *in vivo* conditions [3, 9].

Quantum dots have emerged as novel fluorescent probe for *in vivo* biomolecular and cellular imaging. Quantum dots are materials exhibiting quantum confinement in all three spatial dimensions. Due to their size-tunable light emission, improved signal brightness, resistance toward photo-bleaching and simultaneous excitation of multiple fluorescence colours, they are widely used as optical labels in immunoasseys for proteins, DNA, bacteria and toxin analysis. Compared to standard fluorescent dyes, quantum dots have additional advantages of high photochemical stability and offer improved detection sensitivity and application lifetime. Moreover, they are used to probe and track single biomolecules in live cells owing to their high photostability and strong luminescence. Quantum dots are also used as photosensitizers to generate singlet oxygen in photodynamic cancer therapy, as well as radiosensitizers in radiotherapy [1, 3].

1.1.2 Nanomaterial surface functionalization

Engineered nanomaterials have to be soluble in the water phase in order to be exploited for biomedical applications. However, most of the nanomaterials described above are neither biocompatible nor water-soluble. For example, the surface of bare metallic or metal oxide nanoparticles is highly reactive so that they are prone to aggregation and precipitation and also they may cause undesired cytotoxic effects. A possible strategy to avoid these issues is to coat the NP surface with

organic molecules either by non-covalent physisorption or chemisorption. Charged molecules are employed to achieve ionic stabilization, through Coulomb repulsion, while neutral molecules, zwitterionic molecules or polymers, such as polyethylene glycol (PEG) chains, act as steric stabilizing agents [20]. For example, the citrate capping layer physisorbed on the surface of bare Au NPs allows the colloidal dispersion of Au NPs in the water phase [1, 21]. Another surface functionalization method is based on chemisorption, which offers the advantage of robust linkage and thus a better stability of the surface ligand shell. For example, the Au NP functionalized by a mixture of mercaptoundecane sulfonate (MUS) and octanethiol (OT) exibit high water solubility and membrane embedding and fusion activity [22, 23]. Other general examples are thiols on metals and semiconductors, silanes on oxide NPs, and phosphates on metal oxide nanomaterials (Fe oxides or TiO_2 NPs).

A highly effective surface engineering strategy for chemisorption of ligands is the *ligand exchange technique*, in which the ligand of interest displaces the stabilizing capping layer on the nanomaterial surface (for example citrate molecules for Au NPs) [24]. In this case the ligand should have at least equal or higher affinity than the capping molecule towards the nanomaterial in order to partially or fully displace it. The same strategy is frequently applied also in quantum dot synthesis where a capping agent is used to stabilize the CdSe or CdSe – ZnS core-shell NPs. Subsequent treatment with thiols introduces the ligand shell to the quantum dots [1].

For en effective use of NPs for biomedical applications, the surface coating need to be also biocompatible [25]. For example, the well known PEG stealth effect is base on functionalize the nanomaterial surface with PEG chains to improve the biocompatibility, the colloidal stability and the blood circulation time of metal NPs [9, 26].

Beyond the ability to confer colloidal stability and biocompatibility, the nanomaterial coating can be exploited to target, deliver drugs to, image or damage the biological environment. Typical organic ligands used to functionalize nanomaterials for biomedical applications are organic chains, small peptides and DNA strands, which can be used in targeted delivery or sensing. Fluorescent molecules can also be anchored to nanomaterials for imaging applications. Here, due to the large variety of biomolecules that can be used to functionalize the nanomaterial, as reviewed by Thanh and collaborators [21], different methods can be used to functionalize the nanomaterial surface. [3, 9, 20, 27].

Surface functionalization has its own drawbacks, too. The complexity of the target biological environment is such that it is often difficult to predic what will be the effect of a specific functionalization in terms of absorption of biological molecules dispersed in the serum. Interactions at the NP surface may contribute to structural reorganization of the surface itself, decreased bioactivity, redox reactions with biological molecules, all of which may cause unintended and unexpected biological outcomes. For example, the adsorption of proteins at the surface of a nanomaterial can affect its cellular uptake and mask its original surface functionality. The challenge, then, is to rationally design the nanomaterial coating so as to mitigate its toxicity, improve its targeting capabilities, reduce the undesidered

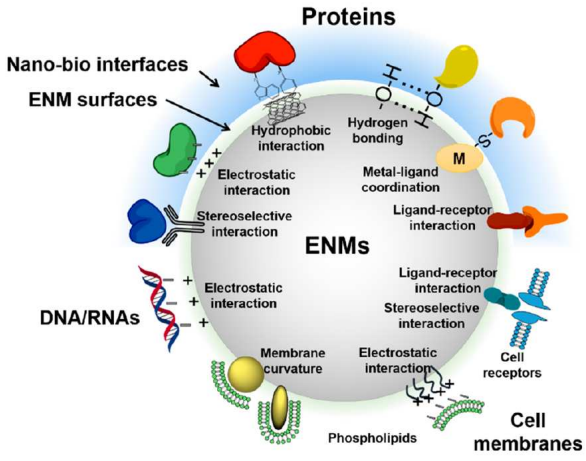

Figure 2: The functionalized surface of engineered nanomaterials (ENMs) is at the interface between the nanomaterial and several biological systems: biofluids, proteins and membranes. Different physical interactions take place, such as electrostatic interactions, hydrogen bonding, hydrophobic interactions, ligand–receptor interactions, and mechanical interactions (e.g. membrane curvature driven interactions). Taken from [5].

adsorption of biomolecules at its surface, control drug delivery and so on. Therefore, a comprehensive understanding of the mechanisms taking place at the nano–bio interface is of paramount importance for the design of safe and effective nanomaterials for biomedical applications [2, 5, 28–30].

1.2 INTERACTIONS AT NANO–BIO INTERFACES

When a nanomaterial interacts with biological systems, the biological and synthetic worlds merge at the *nano–bio interface*. The knowledge-based design of this interface is crucial to a safe and efficient use of nanomaterials for biomedical applications. As shown in Figure 2, the functionalized surface of engineered nanomaterials is at the interface between the nanomaterial and several biological systems: biofluids, proteins and membranes. The nano–bio interface is often a double interface or a three-component interface, comprising the nanomaterial core, its surface functionalization and the biological system. Both the solid-liquid core–coating and liquid-liquid coating–bio interfaces need to be fully characterized to achieve control on the nanomaterial fate in the biological environment. At the nano–bio interface several physical interactions take place: non-covalent interactions (Van der Waals, electrostatic, hydrophobic/hydrophilic), hydrogen bonds and solvation forces, but also chemical reactions (for example ligand-receptor interactions), and even mechanical interactions, such as membrane curvature driven effects. All of these interactions are influenced by the nanomaterial physicochemical properties: size, charge, material, crystallinity and surface functionalization, as well as by the components of the surrounding biological environment and by the biological parameters at the contact zones. To further complicate the matter, the out of equilibrium, complex and heterogeneous nature of the biological milieu inevitably influences the identity of nanomaterials in a dynamic way.

The wide variety of NPs studied in literature and the non-trivial nature of the problem itself makes it difficult to fully understand what happens when NPs are

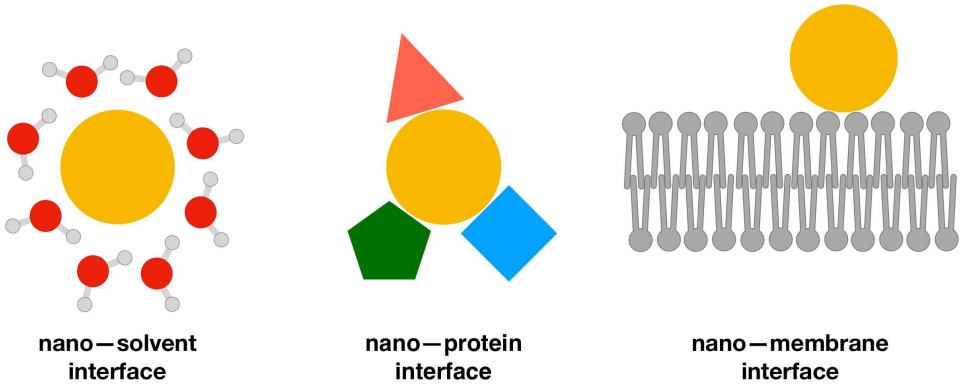

Figure 3: Schematic representation of the nano–bio interfaces considered in this thesis.

administered to the body. Different routes of administration cause NPs to interact with different biological environments.

In this thesis, we imagine following NPs, delivered by intravenous injection, in their journey through the organism. Initially, the NPs come in contact with the bloodstream: here, the NP interacts with water and with serum proteins. The final target of the NP is the cell, and in order to reach the cell interior the NP has to cross the cell membrane. To efficiently develop and engineer effective nanoagents for biomedical applications and guide their fate in the body it is of paramount importance to understand the mechanisms and interactions that occur at each of the following interfaces: the *nano–biofluid interface*, the *nano–protein interface* and the *nano–membrane interface* (Figure 3).

1.2.1 Nano – biofluid interface

The ubiquitous biofluids are complex and crowded biological environments, such as blood or serum, which are vital for life activities. Biofluids are aqueous solutions with dissolved proteins, small organic molecules, ions and cells and mediate the energy and substance exchanges between different biological environments. Biofluids are the first biological environment the NPs meet once they are injected in the body.

On the mesoscopic scale, flow velocity, viscosity, stiffness and diffusivity of biofluids can influence the transportation and the nano–biofluid interaction of nanomedicines *in vivo*. These properties determine the biological fate of nanomaterials, such as protein corona formation, blood circulation time, targeting to the desired site, particle wrapping at the cell surface and nanomedicine biodistribution [31, 32].

On the microscopic scale, the local biofluid environment has a profound impact on the nanomaterial surface. Unfortunately, these complex but important effects have not been addressed comprehensively in the literature, mainly because of the experimental difficulties in characterizing the interactions this soft interface. Thus, the system needs to be simplified. A first step is to consider the interactions at the simpler nanomaterial–solvent interface. For example, the synthesis of Fe – Au

core-shell NPs for biomedical application is highly influenced by the interaction at the solvent–metal interface: the used solvent governs the internal structure and chemical ordering of the core-shell NP. In organic solvents, the NP has a gold shell covering a non-oxidized Fe core, while in aqueous media a gold core is covered by a Fe_3O_4 layer [33]. Hydrogen bonding between the NP surface and the solvent can influence the bioimaging capabilities of quantum dots. For example, it is found that $NaGdF_4$ quantum dots functionalized with polyacrilic acid show better performance as contrast agents for bioimaging than those capped with PEG or polyethylenimine, a fact that is attributed to the strong hydrogen-bond formation between polyacrylic acid and water molecules [34].

A way to provide insights on what happens at nano–solvent interfaces is to use *in silico* simulations to provide molecular-level characterizations of the nano–solvent interface. For example, Yamanaka and co-workers [35] used molecular dynamics (MD) simulations to characterize the interfacial structure of Au NPs functionalized by zwitterionic ligands in aqueous physiological solutions. Depending on the ligand–solvent interactions, they found changes in the NP shape: from an asymmetric and elongated shape to a spherical one with less packed chains. The resulting shape comes from the complex interplay between ligands and solvent and finally could influence the fate of the NP in the organism. In photothermal therapies, it is crucial to understand how the heat is released from the heated-up nanomaterials to the surrounding cold biological environment. For example, MD simulations are used to provide insights in the heat transfer, at molecular-level, between a hot-bare Au NPs or a hot polymer functionalized Au NP and a cold water bath [36, 37]. Also, numerical simulations are used to provide thermodynamic investigations of Au NPs immersed in water and illuminated by a femtosecond-pulsed laser at their plasmonic resonance [38].

All these reports suggest the nano–biofluid interface interactions are in urgent need of study and can be utilized for improving the efficiency of nanomaterials for biomedical applications [5].

1.2.2 Nano – protein interface

Whatever the administration route of engineered nanomaterials, soon or later they come in contact with many different proteins that are present in the biofluids. These different proteins can non-specifically interact with the nanomaterial and adhere on its surface leading to the creation of a highly complex *protein corona* [28, 39–41]. The *nano–protein interface* undergoes dynamic changes as the particles move and interact with the biofluids. The highly dynamic protein corona inevitably leads to the exposure of the newly created nanomaterial to altered functions, as well as, to important shaping of the nanomaterial surface, charge, resistance to aggregation and hydrodynamic size. The dominating driving forces are electrostatic and hydrophobic interactions and hydrogen bonding. The role of each driving force is dependent on charge, amino acid sequence distribution, size and structure of the protein, as well as on the physicochemical properties of the nanomaterial, particularly including hydrophobicity, surface charge and molecular structure. The

interaction site, direction, rate, duration and stability of protein corona are also influenced by the temperature, pH and ion strength of the surrounding biological environment.

Once the protein corona is formed, it constitutes the new "biological identity" of the nanomaterials, which is what cells really see. Thus, it is of paramount importance to understand the effects that proteins on nanomaterial surface can have on the body response. Depending on the specific application the protein corona could be either useful or undesired. For example, if nanomaterials are functionalized for targeted drug delivery applications, the adsorption of proteins on their surface alters their interactions with the specific target, loosing delivery efficiency. Moreover, the nano–protein interface could be recognized by the immunological system that remove the nanoparticle from blood circulation, affecting again the delivery efficiency and requiring a higher administered dose. Thus, it is of paramount importance to control the adsorption of proteins on nanomaterials. Different strategies have been used to prevent corona formation. The most promising is the PEGylation of the nanomaterial surface [26], which consists in the functionalization of the surface with PEG molecules. This approach is considered an efficient way to reduce the protein adsorption. Zwitterionic polymers proved even more efficient as anti-fouling coatings due to the presence of both positive and negative moieties in the same molecule. The strong solvation shell around ions guarantees a more stable surface hydration compared to the simple hydrogen bonding network formed around hydrophilic polymers [42]. Zwitterionic polymers have been and still are intensively studied both experimentally and with computer simulations [25]. Moyano *et al.* [43], for example designed and tested zwitterionic molecules with tunable hydrophobicity. Small gold NPs functionalised with these molecules showed good resistance to protein corona formation. Recentely, MD simulations was performed by Simonelli and co-workers [44] to study how different ligands can influence the interaction of NPs with the most abundant protein in blood, human serum albumin. They tested two zwitterionic ligands with different hydrophobic content and found that ligand conformation, which is affected by ligand hydrophobicity, promotes different adhesion strengths between NPs and albumin.

The adsorption of proteins on the nanomaterial surface could be also toxic for the effects that organic molecules cause on the nanomaterial itself (Figure 5). For example, proteins, but also other organic substances, increase the dissolution rates of particles like ZnO, CdSe, Fe and Ag oxides. The dissolution process of nanomaterials can cause extraction of surface metal atoms, creation of electron-hole pairs that lead to oxydative damage and promoting the creation of reactive oxygen and nytrogen species that lead to cell oxidative stress. Nevertheless, these mechanisms are sometimes useful, for example, in the antimicrobial activity of ZnO or Ag NPs. Of paramount importance, is also studying the reverse effects of nanomaterials on proteins, such as protein conformational changes, fibrillation, denaturation, exposure of new antigenic epitopes and loss of protein function (enzymatic activity) caused by the interaction with nanomaterials (Figure 5). For example, NPs could act as catalyst exposing protein interaction domains that induce aggregation and

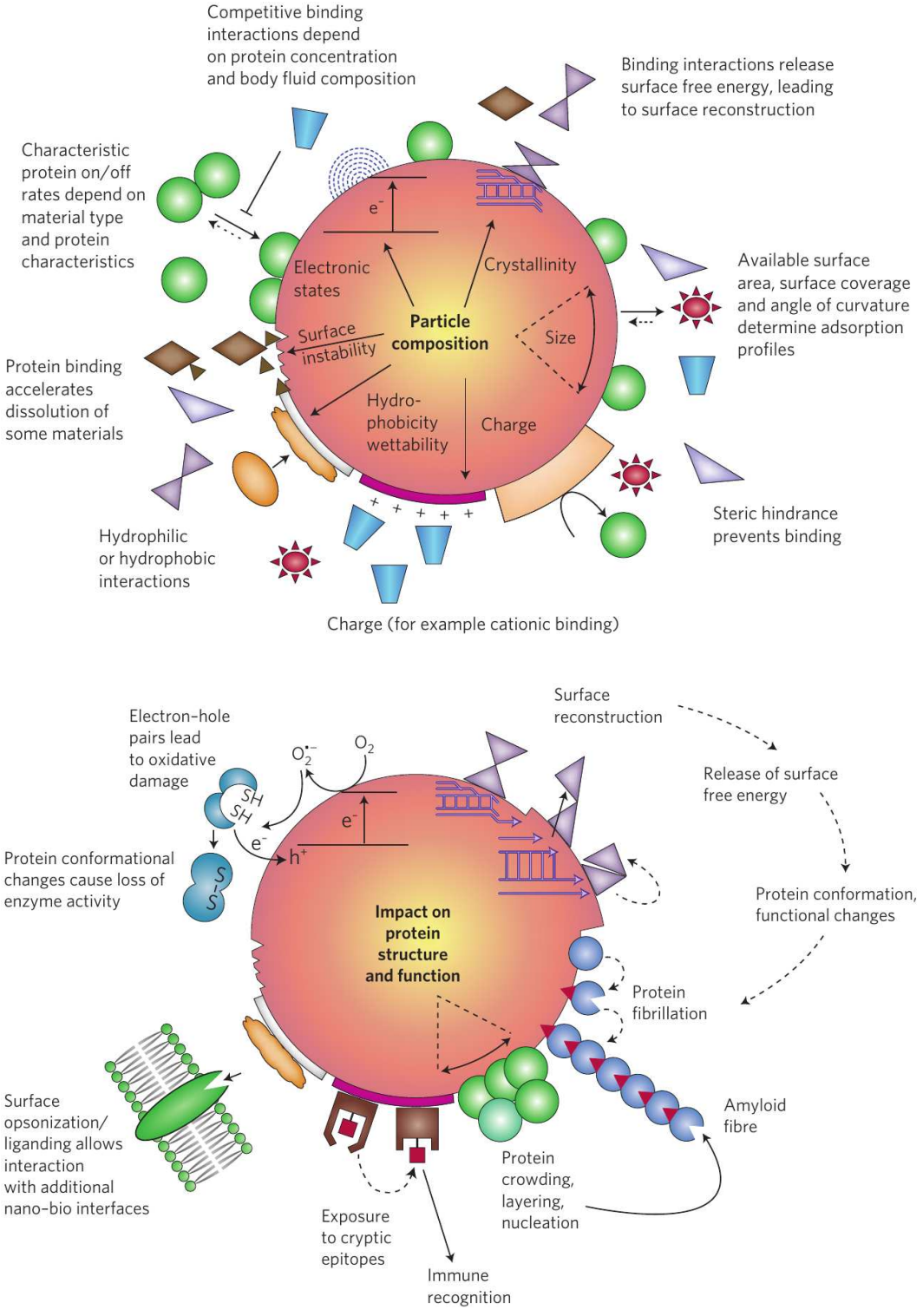

Figure 4: Top: Nanomaterial characteristics that contribute to the formation of the protein corona. Moreover, the characteristic protein attachment/detachment rates, the competitive binding interactions, the steric hindrance by detergents and adsorbed polymers and the protein profile of the body fluid lead to dynamic changes in the corona. Bottom: Effects of protein corona surrounding a NP and potential changes in protein structure and function. The interaction of proteins and biomolecules with the nanomaterial surface, can lead to potential molecular mechanisms of injury that could contribute to disease pathogenesis. The coloured symbols represent various types of proteins. Taken from [28].

the formation of disease-promoting fibrils.

Controlled adsorption of proteins onto nanomaterials can be used to guide NPs in their journey to and inside cells. Thus, it is of paramount importance to understand which physicochemical properties of nanomaterials drive the nano–protein interactions. In this perspective computational studies can coordinate with experiments to first track the composition of the protein corona and then study if a pattern exists to drive the nano–protein interaction [45]. Thus, being able to efficiently engineer nanomaterials with specific molecules which bind only selected proteins will allow to control the fate of nanomaterials for biomedical applications.

1.2.3 Nano – membrane interface

In the biomedical and pharmaceutical applications, nanoparticles are often required to be transferred into the cell and localize at the targeted cellular component. The interaction between nanomaterials and cells is non trivial and strongly depends on the cell type, its environment and on nanomaterial size, shape and surface composition. When nanomaterials are transported into cells, the most critical barrier is the cell membrane. The cell membrane is a fundamental biological barrier that divide the interior and exterior of the cell and it is mainly composed by different phospholipids, glycolipids, cholesterol and membrane proteins. Transport of extracellular matters into a cell, and *vice-versa*, is selectively regulated by the cell membrane. Therefore, a key issue to realize the potential biomedical applications of NPs is the development of a technology that can control the nanomaterial interaction with the cell membrane, and eventually, the translocation across the membrane itself. To develop such a technology, it is necessary to understand the molecular mechanism at the *nano–membrane interface* (Figure 5) [28, 46].

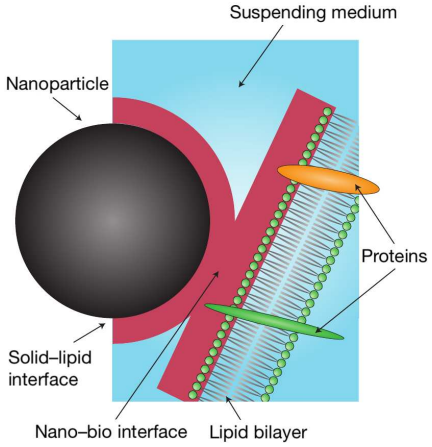

Figure 5: Schematic representation of the interface between a nanoparticle and a model lipid membrane. The red area indicates the nanobio–interface. Taken from [28].

The different properties at nano–membrane interface, not only governs the adsorption and engulfment of nanomaterials at the membrane surface but also its possible internalization pathway. Small and slightly polar compounds can passively cross the cell membrane. Polar or charged small molecules can be exchanged using trans-membrane proteins which serve as membrane channels. Larger molecules are internalised in cells by endocytosis: the cell membrane engulfs the object to be

transferred forming a vesicle which eventually detaches from the membrane and travels in the interior of the cell. It has been found that NPs are able to penetrate cells both via direct permeation, that is NPs can pass through the cell membrane without being trapped into liposomes, and endocytosis [48, 49] which is the major translocation pathway. Direct permeation would be preferable to endocytosis since NPs cannot often escape from lipid vesicles, thus reducing delivery efficiency. As recently reviewed by Nakamura *et al.* [46], size and shape of nanomaterials seems to play a crucial role in selecting the cell penetration mechanism. Nanomaterials with size in range of tens to hundreds of nanometers are usually internalized *via* a nonspecific endocytosis or ligand-receptor mediated endocytosis process. On the contrary, for nanoagents in the sub-10 nm range a passive and direct penetration process seems to be favored. Shape could also be another factor. For example, it has been suggested that rod-shaped and cylindrical NPs usually taken up with less efficiency than spherically shaped nanomaterials [28].

Nanomaterial surface charge plays also an important role in NP interactions with cell membranes, especially when the NPs have a charge of opposite sign with respect to the membrane or to specific membrane protein domains [48]. For example, cationic, anionic or zwitterinic nanoparticles have been shown to favorably interact with cell membranes, even in the sub-10 nm size scale [49, 50]. Consistent body of experimental work from different groups [47, 51, 52] focused on cationic and anionic Au NPs with a core in the sub-10 nm range, showing that they can interact passively with mammalian cell membranes and model lipid bilayers (Figure 6). Nevertheless, although still debated it is thought that nanomaterials with cationic surfaces exert stronger effects than their anionic counterparts, with a possible enhanced toxic effect [47, 53–55]. Even hydrophobicity have to be considered in the nano–membrane interactions. For example, using MD

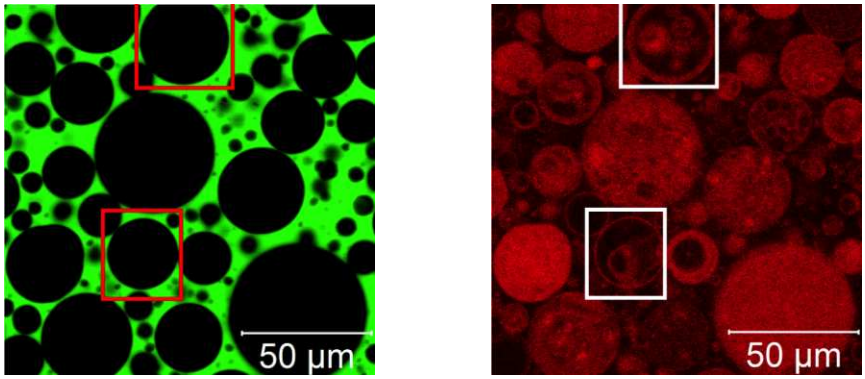

(a) calcein **(b)** BODIPY

Figure 6: Confocal microscopy images of BODIPY-labelled anionic AuNPs interacting with multilamellar model vesicles. Left: calcein fluorescente probe (green fluorescence) outside the liposomes cannot penetrate the vesicles once NPs are added to the solution. Right: BODIPY-labelled NPs (red fluorescence) interact preferentially with the lipid membrane and can non-disruptively penetrate in the liposome interior co-localising within lipid membranes. Taken from [47].

simulations, pristine fullerene NPs have been shown to spontaneously interact and penetrate the model lipid bilayer by the hydrophobic effect: fullerenes aggregate in the water phase and penetrate the lipid membrane as an aggregate which then dissolves in the lipid membrane core [56, 57].

Even the cell membrane characteristics can influence the nano–membrane interface. For example, the electrostatic attraction between oppositely charged NPs and membranes certainly favors the formation of stable nano–membrane complexes [48, 58, 59], as also shown by the group of Bothun and collaborators [60]. They found that Ag NPs functionalized with a mixture of neutral and positively or negatively charged groups, have strong binding with oppositely charged model vesicles. Also, negatively charged single strained DNA-modified Au NPs can stably interact with positively charged cell membranes [59]. Another possible factor affecting the nano–membrane interface is the membrane composition: cell membranes, in fact, present structures with different rigidity, called lipid rafts, which contain a large amount of cholesterol along with negatively charged lipids. Lipid rafts can move in the fluid lipid matrix of cell membranes and eventually come in contact with the NPs [61]. Experiments with ZnO NPs and multicomponent liposomes, for example, showed that ZnO NPs seem interact and eventually penetrate across lipid disordered phases and in proximity of phase boundaries [62]. Conversely, lipid-functionalized and cationic superparamagnetic Fe oxide NPs were found to only adhere to the lipid membrane containing a mixture of cholesterol, neutral and negatively charged lipids [63]. Both kinds of NPs were found to prefer cholesterol rich membranes, with lipid-functionalized NPs irreversibly binding to the bilayer surface.

The increasing interest in the field has produced a vast literature on the nano–membrane interaction. Nevertheless, to be able to efficiently engineer nanomaterials with specific targeting capabilities, it is needed the knowledge, at the molecular level, of the interaction at the nano–membrane interface. However, little is known about molecular mechanisms that occur at nano–membrane interfaces. Computer simulations, in conjunction with experiments, can be useful to provide molecular-level interpretations of the nano–membrane interaction of model systems and efficient design of nanomaterials for biomedical applications.

1.3 GOLD NANOPARTICLES

Among the large variety of nanomaterials which proved useful for biomedical applications, Au has attracted great attention over the years. Gold is indeed chemically stable and non-toxic. In particular, Au NPs are well-known to be stable against oxidation under different physiological conditions (pH, ionic strength and temperature) without any major risk of leak of toxic species. Meanwhile, the surface of Au NPs can be easily functionalized by a wide variety of organic ligands *via* thiol or amine bonds. These two properties make Au NPs an ideal nanoscale platform for a wide range of biomedical applications [64–67], such as drug and

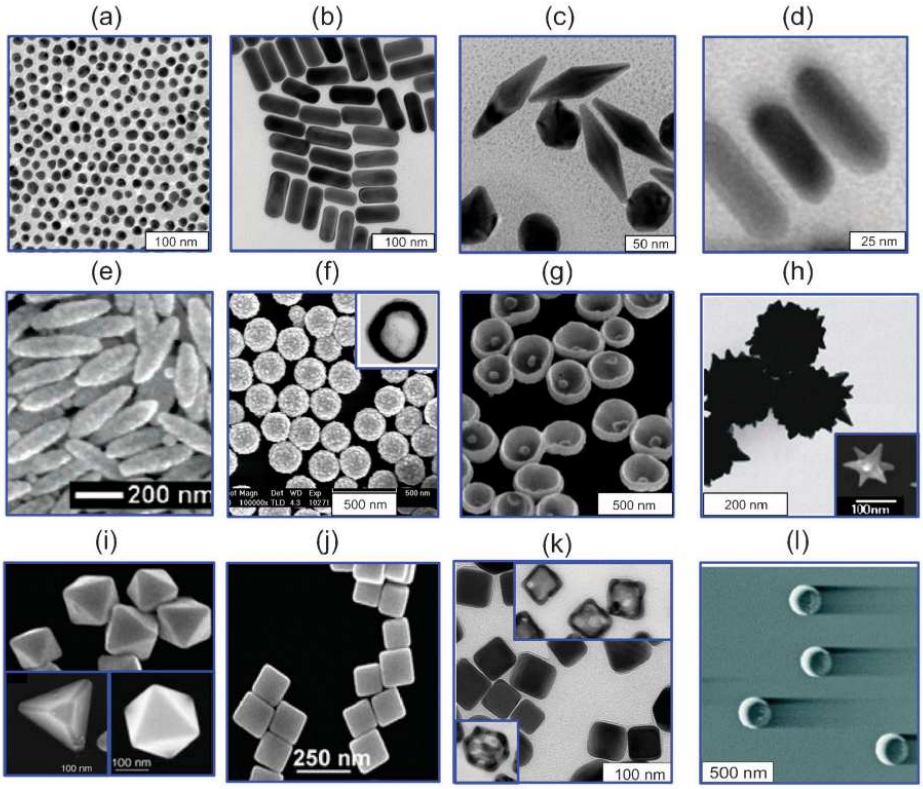

Figure 7: Various types of nanomaterials: 16 nm nanospheres (a); Au nanorods (b); Au bipyramids (c); Au nanorods surrounded by Ag nanoshells (d); "nanorice" (Au-coated Fe_2O_3 nanorods) (e); $Au-SiO_2$ core–shell NPs (the inset shows a hollow nanoshell) (f); nanobowls with bottom cores (g); spiky $Au-SiO_2$ nanoshells (the inset shows a gold nanostar) (h); Au tetrahedra, octahedra, and cubooctahedra (i); Au nanocubes (j); Ag nanocubes and Au–Ag nanocages obtained from them (in the insets) (k); and Au nanocrescents (l). Taken from [68].

gene delivery, biosensing and bioimaging, as well as photothermal treatments and so on.

Many review papers are available on Au NPs and its applications in biomedicine [50, 55, 64, 65, 67–71]. Au NPs can be synthesized in a multitude of shape and size (Figure 7). For biomedical applications nanorods, nanospheres, nanocages and hybrid core–shell NPs (such as $Au-SiO_2$ core–shell NPs) are typically used, with various type of engineered surface coating. Different synthesis methods have been developed and refined to obtain low polydispersity in the size and shape distribution, which can be tuned depending on the specific biomedical application.

In addition to tuning size and shape of Au NPs, its surface can also be functionalized with different kinds of organic molecules. To stably functionalize Au NPs, organic ligands are usually thiolathed on the Au surface. The ligands contain a carbon-bonded sulphydryl ($R-SH$) group. The sulphur atom can be deprotonated and it form a strong bond with Au atoms. Functional molecules introduce other and new physicochemical properties including enhanced biocompatibility, stimuli-responsiveness, antifouling and cell targeting capabilities. Nevertheless, one of

main reasons to protect and functionalize the surface of Au NPs is to stabilize the colloidal solution of Au NPs in water, thus preventing its aggregation and precipitation. For example, citrate molecules physisorbed on the Au surface prevents the precipitation of bare Au NPs in water solution. Au NPs with a net positive or negative charge as well as functionalized with neutral hydrophilic ligands, such us antifouling PEG chains or other polymers, can be produced. Other biological molecules such as DNA, RNA and small peptides can be stably bound to Au NPs.

PLASMONIC IMAGING AND THERAPIES A key characteristic that distinguishes Au NPs from other nanomaterials in the biomedical context, is their unique optical properties and interactions with light, properties that result from a physical phenomenon known as *localized surface plasmon resonance*. The localized surface plasmon resonance involves coherent oscillation and excitation of conduction-band electrons on the surface of Au NPs, upon irradiation of light in the ultraviolet-visible-near infrared region. This strong interaction with light facilitates the use of Au NPs in a wide range of novel types of sensing and therapeutic applications [65]: photothermal therapies [64], optical trapping *in vitro* [72], and nanoscale propulsion *via* thermophoretic effect [73]. Moreover, the surface plasmon resonance frequency depends on the NP size, shape and surface functionalization. Acting on these parameters it is possible to shift the plasmon resonance frequency in the near infrared region. In this region tissues are transparent to radiation which thus penetrates deeper in the body enhancing the treatment efficiency.

In the sensing field, the surface of Au NPs can be conjugated with selective molecules so that complementary molecules will attach to the surface: the resulting shift in the plasmon resonance frequency can be related to the concentration of the bound target molecules. In this way, Au NPs act as a local sensor probe *in situ* or *in vivo* [71]. For instance, antibody-conjugated Au NPs has been used for pregnancy test [74]. On the therapeutic side Au NPs can be used as heating source for localized thermal therapies. Once irradiated with a laser source at the plasmon resonance frequency, Au NPs absorb radiation and efficiently convert it into heat. For example, the resultant plasmonic heat can elevate the surrounding temperature sufficiently to damage and kill cancerous tissues by hyperthermia. Among the possible photothermal therapies, *photoporation* [75–77] is one that has received increasing attention in recent years (Figure 8). Photoporation is a physical approach to permeabilise a cell membrane by means of localized heat source, for example, a laser pulse. In its original formulation, the laser source is directly applied to cell membranes. In this set-up, molecules to be delivered, like short interfering RNA, are dispersed in the liquid phase surrounding the cells, and a high intensity-highly focused laser pulse, of very short duration, is direcetd to the cell membrane to achieve poration and the spontaneous entrance of molecules into the cytosol. The effectiveness of this approach can be highly improved if surface plasmon resonant Au NPs are involved in the process. NPs need to be stably bound to the cell membrane. In this case, the whole cell can be irradiated by a low-intensity laser pulse in the near-infrared range and the resonant NPs are responsible for the efficient light-to-heat conversion. Heat is locally released to the

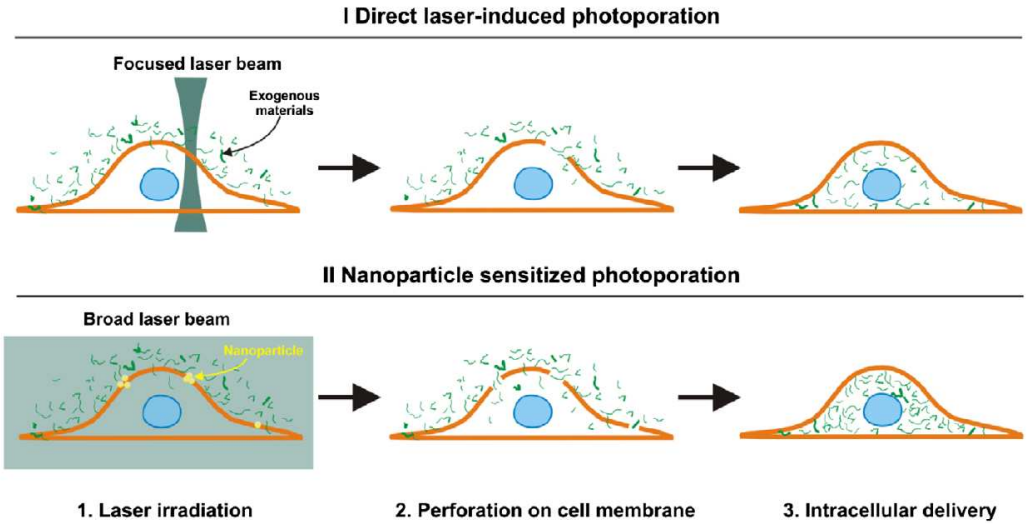

Figure 8: (I) Direct laser-induced photoporation: the high intensity laser beam is focused precisely on the cell membrane to achieve a locally high photon density. (II) NP-mediated photoporation: the NPs are first incubated with the cells to allow them to adhere and stably bound to the cell membrane. In the latter case, a low intensity broad laser beam can be used to photoporate many cells at the same time: the resonant NPs are responsible for the efficient light-to-heat conversion. Following laser irradiation, exogenous compounds in the cell medium can diffuse through the membrane pores into the cell. Taken from [76].

surrounding membrane causing the formation of transient pores with little or no cytotoxic effects. Another possibility is to use Au NPs as therapeutic agents. In this case, they have to be further engineered as smart nanocarriers to deliver and release drugs or genes at the desired site and time triggered by plasmonic heating. For example, Au NPs decorated with thermoresponsive polymers induce the a phase transition of the polymer coating by means of the plasmonic heat released at the NP surface. As a consequence genes, nucleic acids, proteins or drugs can be trapped/expelled by the polymer cage [78–80]. The versatility of Au NPs can also extends to multiple and selective release depending on the wave form of the light [81]. For example, continuous light adsorbed by DNA-functionalized Au NPs induces collective heating effects of Au core, causing DNA dehybridization and release of a single strained DNA, while pulsed light suppresses such a heating effect and transfers hot electrons to break the Au – S bond, thus releasing the double strained DNA. Such selective release of DNA (or potentially RNA) can be efficiently addressed to prohibit transcription or translation of messenger RNA, making the NPs useful for applications in gene therapy as well as drug delivery in cancer therapies.

1.4 AIM OF THIS THESIS

Gold nanoparticles have become a standard in many experimental as well as computational studies and a large bulk of literature exists on this topic. In this

work we use computer simulations to investigate, at molecular level, the interaction between small functionalized Au NPs with different biological interfaces.

NANOPARTICLE – SOLVENT INTERFACE

When Au NPs are used in photothermal applications, and in particular in photoporation setups, resonant NPs are responsible for the efficient conversion of light into heat, which is then released to the surrounding biological tissues. To achieve the maximum efficiency it is of paramount importance to know what is the effect of the surface chemistry on heat transmission at the nano–bio interface. In Chapter 4, we use MD simulations at atomic level resolution to investigate the influence of the protecting ligand shell on the temperature profile around an irradiated Au NP. We show that the large water mobility recorded at hydrophobic ligands interface prevents heat exchange at ligand–water interface, hence increasing the thermal resistance and heating of the ligand shell. Meanwhile, the low water mobility recorded at hydrophilic interfaces promotes heat exchange, reducing the thermal resistance at ligand–water interface.

NANOPARTICLE – MEMBRANE INTERFACE

Once Au NPs reached their target cells, the interaction between NPs and cell membrane is dependent on numerous NP and cell membrane characteristics at interface. Since the interplay of these elements is non-trivial, to study the NP–cell membrane interaction at a fundamental level, the system must be kept as simple as possible. In Chapter 5, we report on the molecular mechanism by which a small monolayer–protected Au NP interact with a model lipid membrane. In particular, we investigate how the NP surface charge and and chemistry can drive the NP–membrane interaction. We show that the spontaneous protonation of anionic carboxylic ligands on the NP surface can occurs when the NP penetrate the membrane. Hence, we show also that the ligand protonation can make the NP–membrane interaction faster and less disruptive.

NANOPARTICLE – PROTEIN INTERFACE

In Chapter 6, we investigate, by means of both atomistic and coarse grained molecular dynamics simulations, the interaction between small Au NPs and ubiquitin, an ubiquitous protein present in most living organism. We provide a molecular level characterization of the experimental results obtained by Ahmet Bekdemir under the supervision of Francesco Stellacci on the NP–ubiquitin interaction. We show coherent results with the experimental ones. In particular, the charge and chemistry of the NP ligand shell influence and drive its binding energetic with ubiquitin, but not its binding geometry.

2 SIMULATION METHODS

The motion of a classical system in time and space is governed by Newton's equations of motion. Classical laws of motion have proved to be a good approximation also at the molecular level as long as atoms are massive enough. In this work, we will treat large biological systems as classical many-body systems of atoms and molecules.

In order to predict the time evolution of a system composed by a large number of atoms and molecules, Newton's equations of motion need to be integrated numerically. The necessity of a numerical integration arises from the complexity of the interactions involved in realistic systems, often nonlinear functions of positions and momenta of the particles, which makes it impossible to obtain an analytical solution for the equations of motion. This is where molecular dynamics (MD) comes into play: given a set of initial conditions and interactions, the time evolution of the system can be obtained from the numerical integration of the equations of motion.

In the first part of this chapter the basic concepts of statistical mechanics underlying molecular dynamics (MD) simulations will be summarized. Then, the advanced sampling technique used in this thesis will be introduced. Finally, will be summarized the interaction models necessary to describe our systems, that is: the classical models for intra-molecule and inter-molecule interactions. We will describe atomistic force fields (FFs), which explicitly represent each atom in the system under study; then, we will present coarse grained (CG) FF, and in particular the MARTINI FF used in this work. For a more detailed description of these concepts the reader is addressed to the books of Tuckerman [82], Leach [83], Frenkel and Smit [84] and Allen and Tildesley [85].

2.1 MOLECULAR DYNAMICS SIMULATION

Molecular dynamics (MD) is a set of techniques that allows us to prepare a "*computer experiment*" in which, by solving numerically the classical equations of motion of a virtual system, we are able to predict its time evolution. Such virtual experiment approach has the advantage that many experiments can be set up with different initial conditions and/or with different control parameters, such as temperature or pressure. Obviously this experiment is carried out using a model that approximates the real system. Th model consists of a the description of the interactions among all system particles, i.e. it corresponds to the potential energy function (PEF) $U = U(\vec{x})$, function of $\vec{x}$, the coordinates of each particle in the system, from which the forces are derived.

In the Hamiltonian description, the equations of motion can be derived from the Hamiltonian function $H = H(\vec{x}, \vec{p}, t)$ of the system, where $\vec{p}$ is the momenta of each particle in the system. If $U = U(\vec{x})$ is time-independent, the Hamiltonian represents the total energy of the system:

$$H = K(\vec{p}) + U(\vec{x}) \tag{2.1.1}$$

where $K(\vec{p})$ is the kinetic energy and $(\vec{x}, \vec{p})$ is called *phase space point*.

According to statistical mechanics, a macroscopic property A of a system with a large number of particles can be computed from their phase space coordinates. It can be shown [82] that it exists a scalar function of the Hamiltonian $f(H(\vec{x}, \vec{p}))$ such that the equilibrium observable A can be expressed as

$$\langle A \rangle = \frac{\int_\Omega A(\vec{x}, t) f(\mathcal{H}(\vec{x}))\, dx}{\int_\Omega f(\mathcal{H}(\vec{x}))\, dx}$$

where Ω is the volume of the phase space. $\langle A \rangle$ is called *ensemble average* of the observable A.

With this definition in mind, we need also a link between statistical mechanics, i.e. the ensemble average, and the experimental values. When we measure a macroscopic observable we prepare an experiment and we study its evolution in time. The value of A is a function of time and phase space coordinates and it fluctuates over time due to particle interactions. The measurement itself requires long time interval compared to microscopic time scales, thus when we measure an observable we take an average over time. If, in principle, the time for average is infinity then we have the "real" mean value of the observable

$$\overline{A} = \lim_{\tau \to +\infty} \frac{1}{\tau} \int_{t_0}^{\tau} A(\vec{x}_t)\, dt$$

In order for a comparison to be made, a link between $\langle A \rangle$ and $\overline{A}$ must be established. Moreover, the sampling of the probability function $f(H(\vec{x}, \vec{p}))$ for each point in the phase space is non–trivial. The workaround is provided by a link between the ensemble and time average that comes from the *ergodic theorem* and the *ergodic hypothesis*. A system is said to be ergodic if, over a long period of time, all the states in the phase space with the same energy are accessible with the same probability. Then the ergodic theorem says that, if the system is ergodic, the ensemble average of A computed from the probability function $f(H(\vec{x}, \vec{p}))$ and the time average of A is equal almost everywhere in the phase space, provided that the latter is performed on an infinitely long trajectory. So we can write the follow identity

$$\overline{A} = \lim_{\tau \to +\infty} \frac{1}{\tau} \int_{t_0}^{\tau} A(\vec{x}(t))\, dt = \frac{\int_\Omega A(\vec{x}, t) f(\mathcal{H}(\vec{x}))\, dx}{\int_\Omega f(\mathcal{H}(\vec{x}))\, dx} = \langle A \rangle \tag{2.1.2}$$

Solving the equations of motion, described by H, with a numerical integrator, an MD simulation generates a set of coordinates, called *trajectory*, at discrete times that are multiples of the fundamental time discretization parameter, called *time step*,

δt. Starting from an initial phase space vector $\vec{x}(0)$, that is the initial configuration, the forces are computed at each step from the PEF. Then the equations of motion are integrated and a new configuration $\vec{x}(\delta t)$ is generated, thus a new set of forces is computed and so on. δt is called *MD time step*. A basic MD simulation can be described by the flowchart shown in Figure 9. In order to compute time averages we need to discretize Equation (2.1.2) so the time integration is substituted with a summation over the collected data at fixed time steps $\Delta\tau \geqslant \delta t$. The formula becomes

$$\langle A \rangle = \frac{1}{M} \sum_{n=1}^{M} A(\vec{x}(n\Delta\tau)) \tag{2.1.3}$$

where $M\Delta\tau$ is the total averaged time.

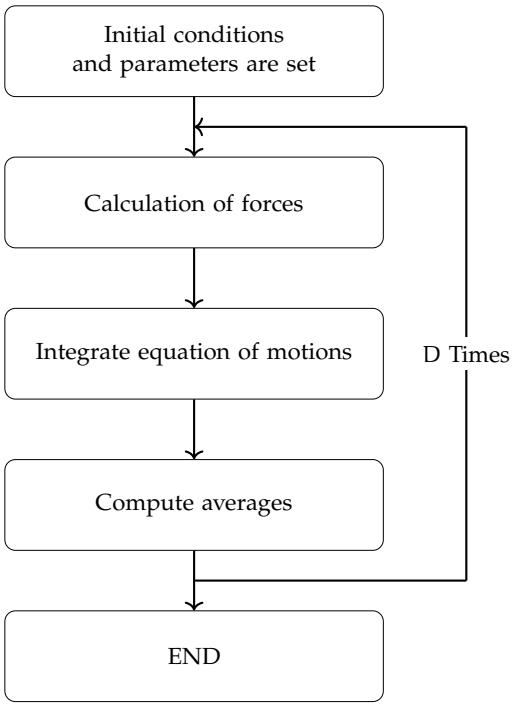

Figure 9: Schematic representation of an MD simulation.

WORKING PRINCIPLES To perform an MD simulation, and to solve Newton's equations of motion, a numerical integrator is required. Time is discretized in time intervals and positions and velocities are obtained from previous values with a finite-difference method. Once the integration algorithm is chosen, an initial configuration is necessary to start the computation of the trajectory. Its choice can be nontrivial and it depends on the complexity of the system. Then, care must be taken in setting up the initial configuration. The initial set of positions $\vec{x}(0)$ and velocities $\vec{v}(0)$ is assigned to the atoms in the system. While positions are usually taken from experimental structures or assigned by design, the velocities are typically determined extracting random values from the Maxwellian distribution of velocities at the temperature of the simulation. The time step for integration is

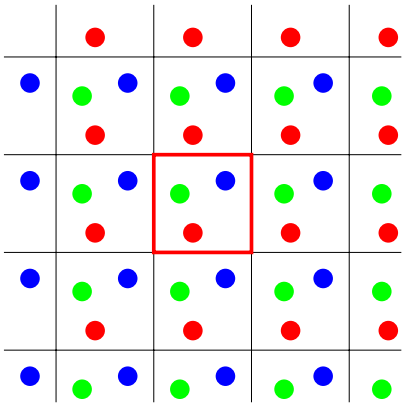

Figure 10: Schematic view of a two–dimensional box with PBC imposed. The central, red contoured, box is the simulation box and it is replicated along each side.

chosen based on the characteristic motions of the atoms in the system. If τ is the period of the faster vibration in the system, a good rule of thumb for the choice of δt is $\tau/\Delta t \sim 20$. For example, if hydrogen atoms are explicitly considered, the typical period of vibration in a hydrogen involved bond is about $\tau \sim 10$ fs, then, an appropriate time step would be about 0.5 fs. The integration stops when the number of integration steps previously set has been reached.

PERIODIC BOUNDARY CONDITIONS When an MD simulation is performed, the system is inserted into a so called *simulation box* whose shape can be differently chosen to better reproduce the symmetry of the simulated system. In order to avoid surface effects and to consider only an infinite bulk system, periodic boundary conditions (PBC) are imposed to the simulation box. This gives us also the possibility to simulate system's bulk proprieties without considering a too large number of particles. In Figure 10 an example of a two–dimensional box with PBC is shown. The central red contoured box is the simulation box. The idea is to replicate that box in space along each side so that there are no surface particles nor walls in the central box. Only box geometries compatible with translational symmetry can be used. For example, nether a spherical nor a icosahedral box could do the job. However when it is possible one has to use the most appropriate shape to better describe the symmetry of the system, otherwise a close approximation, compatible with PBC, must be used.

Even if PBC are used in a wide range of applications, it must be taken into account that imposing periodicity to a system may affect its properties. A clear limitation of the periodic cell is that it is not possible to achieve fluctuations that have a wavelength greater then the cell length. This causes, obviously, the impossibility to sample those vibrating modes. Another problem arises with the range of the inter–particle interactions: one has to choose carefully the size of the simulation box, or the number of particles, to ensure that the smallest simulation box length is at least twice as long as the interaction range.

CONSTANT TEMPERATURE AND PRESSURE The relevant ensemble for biological systems in physiological conditions is the isobaric-isothermal NPT ensemble. To

maintain the system at constant temperature and pressure it is necessary to couple it with an external temperature bath and a pressure bath. The simplest way to impose constant temperature in MD simulations is to rescale velocities, using the so called velocity rescale algorithm [86]. An other approach is to couple the Hamiltonian of the system with an external temperature bath, as done in the Noose–Hoover algorithm [87]. Both the algorithms are able to drive the system at target temperature as well as to correctly sample the instantaneous temperature fluctuations. Simulations at constant pressure can be performed applying a scaling to the coordinates of the system, along with a volume scaling, as proposed by Berendsen [88]. The scaling factor depends on the isothermal compressibility of the system, on the difference between the instantaneous pressure and the target pressure and on the barostat relaxation time. Even if the Berendsen barostat succeeds in driving the system to the target pressure, it fails in reproducing the fluctuations of the instantaneous pressure. To retrieve the correct behavior of pressure fluctuations the Parrinello–Rahman approach [89, 90] can be adopted: both the shape and size of the box are allowed to change during the simulation and a coupling term between the system and a pressure bath is introduced into the Hamiltonian of the system through a coupling constant related to the relaxation time of the system.

MOLECULAR DYNAMICS SOFTWARE All MD simulations for this thesis are performed with the Gromacs package [91] which provides different integrators, barostats and thermostats, to run simulations at constant temperature and pressure, different methods to compute electrostatic interactions and different set of tools to analyze the generated trajectories.

2.2 ADVANCED SAMPLING METHODS

The time evolution of a biomolecular system and its equilibrium properties are determined by the system's free energy surface (FES). Free energy differences tell us, for example, if a chemical reaction occurs spontaneously, whether a given solute is hydrophobic or hydrophilic, whether a protein conformational change can take place at physiological conditions, whether some molecules in water solution are able to self–assemble into a more complex system and so forth.

COLLECTIVE VARIABLES Often, we are interested in the FES as a function of some generalized coordinates, called collective variables (CVs) of the system. CVs are variables that describe, in a simple and useful way, some chemical, thermodynamic or mechanical processes that take place in the system. For example, the free energy in function of the distance between the center of mass (COM) of two molecules gives us information about their attraction or repulsion and if they can form a bound state. In this example, the FES restricted to the CV space provides a map of the stable dimer conformations, of the relative stability of these conformations

and of the height of the barriers that must be crossed to make a transition from one FES minimum to another one.

FREE ENERGY SURFACE The calculation of the free energy difference between two thermodynamic metastable states (which requires an *a priori* knowledge of the two stable states) and the calculation of the FES conecting them are one of the main challenges in MD simulations for biomolecular applications. Let us suppose that we are interested in the FES in function of the CV $s(\vec{x})$. The free energy along the CV is obtained as

$$G(s) = -k_B T \ln Q(s) \tag{2.2.1}$$

where $Q(s)$ is the partition function that integrates out all the degrees of freedom (DOF) of the system except for $s(\vec{x})$. Since $s(\vec{x})$ does not depend on particle momenta and using the ergodic theorem (2.1.2), it can be shown that

$$Q(s) = \frac{\int_\Omega e^{-\beta U(\vec{x})} \delta(s(\vec{x}) - s)\ dx}{\int_\Omega e^{-\beta U(\vec{x})}\ dx} = \lim_{t\to+\infty} \frac{1}{\tau} \int_0^\tau \delta(s(\vec{x}(t)) - s)\ dt \tag{2.2.2}$$

where $U(\vec{x})$ is the PEF. $Q(s)ds$ can be interpreted as the probability to find the system with $s(\vec{x})$ between s and $s + ds$.

The time sampling of Equation (2.2.2) can be derived, in principle, via MD. Unfortunately, since the time can not be infinite, the main problem related to MD simulations is whether we are able to correctly sample *all* the phase space point. The answer depends on the system size, and often it takes too much time and/or we are not able to collect sufficient data. This sampling problem can be summarized as follows: regions in phase space around a local minimum of the FES are typically sampled well, whereas regions of higher energy are sampled rarely. These high energy regions must be overcome in order to overcome energy barriers and sample other minima. These transitions are called *rare events*. When the system is moving in the energy landscape the only way to escape from a local minimum is to exploit thermal fluctuations and so energy barriers that are higher then $\sim k_B T$ have a small probability of being overcome.

BIAS BASED ADVANCED SAMPLING Several methods have been developed and are still in development in order to solve the just described sampling problem. These methods are called advanced sampling techniques and allow us to

- escape from a local energy minimum, in order to explore other regions of the phase space;
- calculate the free energy difference between two thermodynamic states;
- compute the FES along one or a small set of CVs.

The common basic idea is to introduce an additional *bias potential* able to confine the sampling to a limited region of the CV space and/or drive the transition between two metastable configurations. In the following we describe only the method used in this thesis work, called *metadynamics* [92, 93], but other methods could be used

such as *umbrella sampling* [94], *replica exchange* [95], *steered molecular dunamics* [96, 97] and so on.

2.2.1 Metadynamics

Metadynamics was originally developed by Laio and Parrinello [92] with the the aim to accelerate the escaping from a free energy minimum in MD simulations and computing free energies in function of a small set of CVs. The basic idea is to enhance the dynamics of a system along some CVs simply by filling the corresponding energy minimum with an history–dependent bias potential, in order to sample larger and larger portions of the phase space. Supposing a two state process from A to B, in the CV space, if the deposited energy is sufficient to fill the energy well of state A, the system can overcome the barrier and go to B. In Figure 11 a simple cartoon is shown.

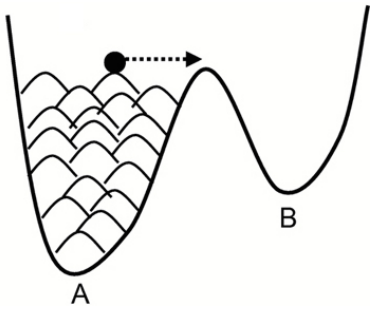

Figure 11: Schematic cartoon of the energy well filling by the history–dependent bias potential and the consequently transition from state A to state B.

This novel idea is supported by the assumption of Laio and Parrinello, based on experimental and heuristic results, that iteratively summing the deposited potential during the biased MD simulation leads to an estimator of the FES along the chosen CVs in the region explored. If $\vec{s}(\vec{x}) = (s_1(\vec{x}), \cdots, s_n(\vec{x}))$ is the CVs vector, where n is a small number, and $w(\vec{s}, t)$ is the bias potential deposited every τ MD time steps the "metadynamics" history–dependent potential acting on the system at a time t is given by

$$w_M(\vec{s}, t) = \sum_{\substack{i=0 \\ i\tau<t}} w(\vec{s}, i\tau)$$

where t is the time in unit of MD time step. The time dependence in the bias potential $w(\vec{s}, t)$ is needed since it has to depend on the values assumed by the CVs at some previous MD steps. The Laio and Parrinello assumption yields the following expression

$$\lim_{t\to+\infty} w_M(\vec{s}, t) \simeq -G(\vec{s}) + C \tag{2.2.3}$$

where C is an additive constant. Since the history–dependent potential iteratively compensates the underlying FES, the system evolved with metadynamics *tends to escape from any energy minima via the lowest saddle point*. Thus, contrary of other methods, metadynamics is suitable not only to compute efficiently FES, but also to explore the lowest-energy reaction paths and accelerate the observation of rare events. If the CVs are chosen sensibly, the system will quickly find its way over

to the lowest free energy saddle point and evolve over the next minimum as it would do in a *very long* MD simulation. The function used for the bias potential is a Gaussian centered around the values assumed by the CV at a time t:

$$w(\vec{s}, t) = w \ \exp\left(-\sum_{i=0}^{n} \frac{(s_i - s_i(\vec{r}(t)))^2}{2\delta {s_i}^2}\right)$$

where w is the height and δs_i is the width of the deposited Gaussians, two input parameters needed to setting up a metadynamics simulation.

BIAS PARAMETERS For setting up a metadynamics simulation, there are three parameters to choose carefully: the height w and the width δs_i of the Gaussians and the stride of deposition τ. These parameters affect the accuracy and the efficiency of the free energy profile reconstruction. It does not exist a universal and general recipe to choose the parameters. Empirical criteria can be used to choose δs and τ; the former by monitoring the standard deviation of the CVs in an unbiased MD simulation, keeping in mind that the history–dependent potential can only reproduce features of the FES on a scale larger then $\sim \delta s$. The latter by considering the relaxation time of the system after a Gaussian is deposited, so as to avoid the deposition of two Gaussians on the same spot at consecutive deposition times.

In Figure 12 an example of the time evolution of a metadynamics simulation is shown. We can see that as the number of deposited Gaussians increases the system is able to visit more regions of the phase space. Moreover, as the simulation time increases, when the energy landscape (lower panel) becomes flat the system becomes diffusive (upper panel) in the CVs space. Thus we can stop the metadynamics simulation obtaining the unbiased FES as in Equation (2.2.3).

Keeping in mind Figure 12 the validity of Equation (2.2.3) can be qualitatively understood in the limit of slow deposition. This means that $w_M(\vec{s}, t)$ varies slowly and the probability to observe $\vec{s}$ is approximately proportional to the Boltzmann factor $e^{-\beta(G(\vec{s}) - w_M(\vec{s}, t))}$. If the function in the exponential has some local minimum due to $G(\vec{s})$, $\vec{s}$ will preferentially be localized in the neighborhood of this minimum and an increasing number of Gaussians have to be added until it is completely filled. When the minimum is filled the system reaches the condition $G(\vec{s}) \sim w_M(\vec{s}, t)$, the probability distribution would be approximately flat and the system becomes diffusive in the region explored by the simulation. Then, in this region, the placement of new Gaussians is no more affected by the difference between $G(\vec{s})$ and $w_M(\vec{s}, t)$ and they are deposited randomly over the flat free energy profile. The FESs reconstructed after that point, as visible in Figure 12, are affected by some corrugations, due to newly deposited Gaussians, of the order of w. From that point on the metadynamics has reached the *convergence* in the sampled region.

CONVERGENCE As explained before, the convergence of the metadynamics in a specific region of the CVs space is reached when the system becomes diffusive in this region, i.e. when the CVs can assume all possible values in the sampled

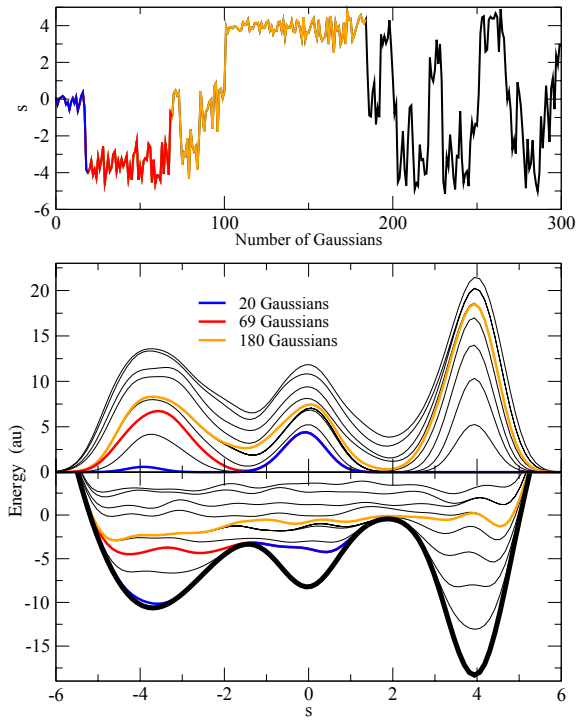

Figure 12: Example of a time evolution of a metadynamics simulation. Top: time evolution of the CV of a system evolved on the 3–minima FES represented by the black thick line in the lower panel. Middle: time evolution of w_M, the history–dependent bias potential. Blue line: w_M when the first minimum is filled and the system escapes to the second minimum; red line: w_M when also the second minimum is filled; yellow line: when the entire profile is filled and the dynamics becomes diffusive on the whole energy landscape. Lower panel: time evolution of the sum of w_M (same color scheme). Taken from [93].

region. Unfortunately in most systems it is not trivial to identify precisely when the diffusive regime has been reached. In most cases a practical method to assess the convergence of metadynamics simulations is based on monitoring the free energy difference between two reference points: when the difference is approximately flat then the convergence has been reached.

METADYNAMICS SOFTWARE To run metadynamics simulations we use a plugin compatible with Gromacs named Plumed [98]. An input file containing metadynamics parameters, that is Gaussian width, height and deposition pace together with the set of collective variables, has to be provided to the software. Analysis tools for metadynamics simulations, such as that to reconstruct the FES of the system, are included in the plugin.

2.3 EMPIRICAL FORCE FIELDS

Biomolecular simulations, especially when requiring the explicit treatment of solvent molecules, often deal with a very large number of particles ($10^4 < N < 10^6$). As for the time scales, they can span a broad range depending on the process under study: hydrogen bond formation in organic molecules, for example, happens on the picosecond time scale; slow processes such as the diffusion of massive colloidal particles take place on time scales of milliseconds if not seconds.

The possibility to achieve the description of such a variety of systems by the same tool, MD, relies on the existence of appropriate models of the interactions between

atoms and molecules. In soft or condensed matter systems these interaction models always rely on the *Born–Oppenheimer approximation*. It consists in integrate out the high frequency electrons' motions considering only the interactions between atomic nuclei. The set of functional forms of the interaction potentials between atoms and molecules and they parameterization are collected into the so called *force field (FF)*. For biomolecular applications different levels of description can be achieved: in *atomistic* FFs basic particles are atoms, *coarse grained* FFs basic particles represent atom groups or small chemical moieties.

PARAMETERIZATION In general the functional forms for potential interactions are common to all particles in the system. The FF is completed by a set of empirical parameters that characterize the interaction between different types of particles, whether they are atoms or whole chemical groups. Interaction parameters are empirical in the sense that they are assigned to reproduce a small set of target properties on a group of reference systems. These target properties can be derived from experimental measurements or from finer–level calculations or simulations. Nowadays, atomistic and CG biomolecular FFs come as "packages" of parameters and functional forms appropriate for the description of a large variety of chemical compounds in the liquid and solid phases.

TRANSFERABILITY As described above the parameterization of a FF involves a small set of test systems for which some set of target properties are reproduced. An important characteristic of a FF is its *transferability* that means the ability of the model to describe situations that differ from those used at the parameterization stage. For example, a FF parameterized to reproduce the physical properties of liquid water in standard ambient conditions should also reproduce other properties such as water melting point, liquid–vapor surface tension, and so on. This is the most challenging aspect of model development, and it relies on a very accurate choice of the target properties used during the parameterization stage.

In the first part of this section we will describe the most common functional forms for modeling the inter–particle interactions and how to treat them in an MD simulation. Then, we will provide a summary of atomistic and CG FFs with a focus on the main CG FF used in this thesis work: the MARTINI FF developed by Marrink *et al.* [99].

2.3.1 Interactions

In MD simulations of molecular systems the inter–particle interaction potentials are usually divided into two main classes: the *bonded interactions* involving particles within the same molecule and the *non–bonded interactions* engaging all particles in the system and which usually represent Van der Waals and electrostatic interactions:

$$U(\vec{x}) = U_b(\vec{x}) + U_{nb}(\vec{x})$$

BONDED INTERACTIONS The most common and general functional form for bonded interaction is given by the following terms

$$\begin{aligned} U_b = &\frac{1}{2}\sum_{\text{bonds}} \frac{1}{2}k_i^b(l_i - l_{i0})^2 + \frac{1}{2}\sum_{\text{angles}} k_i^a(\theta_i - \theta_{i0})^2 + \\ &+ \frac{1}{2}\sum_{\text{torsions}} V_n(1 + \cos(n\omega - \gamma)) \end{aligned} \tag{2.3.1}$$

the first two terms are harmonic potentials that model respectively the energy contribution due to the deviation from a reference bond length l_{i0} and angle θ_{i0}. k_{bi} and k_{ia} are the bond and angle elastic constants. The bond contribution involves a set of two adjacent particles while the angle contribution a set of three consecutive particles in the same molecule. The last term in Equation (2.3.1) concerns the energy contribution due to torsional angles. It involves four consecutive particles in the same molecule.

NON–BONDED INTERACTIONS The non–bonded interactions are related to the Van der Waals and electrostatic contributions to the PEF described by the following terms

$$U_{nb} = \sum_{i=1}^{N}\sum_{j>i}\left(4\epsilon_{ij}\left(\left(\frac{\sigma_{ij}}{r_{ij}}\right)^{12} - \left(\frac{\sigma_{ij}}{r_{ij}}\right)^{6}\right) + \frac{q_i q_j}{4\pi\varepsilon_0 r_{ij}}\right) \tag{2.3.2}$$

where r_{ij} is the distance between particle i and j. The first term is the energy contribution due to the Van der Waals interaction modeled as a Lennard–Jones $12-6$ potential, fully characterized by the constants σ_{ij} and ϵ_{ij} assigned to each pair of particles. The r^{-6} dependence is related to the attractive contribution which takes into account dipole–dipole interactions (Keesom forces), dipole–induced dipole interactions (Debye forces), induced dipole–induced dipole interactions, London dispersion forces. The r^{-12} part is related to the repulsive contribution which takes into account the Pauli exclusion principle between electron clouds. The last term in Equation (2.3.2) is the electrostatic energy contribution described by the particle charge q_i. The non–bonded interactions involve obviously all particles in the system, but for particles belonging to same molecule they are usually computed only if they are separated by a certain number of bonds, usually three, but it depends on the specific FF.

The non–bonded interactions depend on the inter–particles distance r_{ij} and decay to zero as a power of r_{ij}^{-d}. Depending on the power order d compared to the dimensionality s of the system they are split into *short range* if $d > s$ and *long range* interactions if $1 \leqslant d < s$. The Lennard–Jones $12-6$ potential decays to zero as r^{-6} then it is a short range interaction, while the electrostatic term is a long range interaction since it decays to zero as r.

The calculation of non–bonded interactions is one of the most time consuming part of an MD simulation. Even if we use a simple pairwise additive potential their calculation scale as $\sim N^2$. Thus, especially for short range interactions, various methods have been developed in order to speed–up the simulation. The *cut–off*

method is the most used to treat the short range interactions and, in some cases, even the long range ones. Taking one particle into account, the general idea is to evaluate the non–bonded interaction with all other particles that are located within a distance r_c, called *cut–off* radius, otherwise the interaction is set to 0.

LONG RANGE ELECTROSTATICS Since electrostatic is a long range interaction, in the calculation of the electrostatic potential we need to include also the electrostatic contribution from the infinite number of periodic images of the simulation box. This makes the summation non–convergent. Some FFs for biomolecular applications solve this problem by treating the electrostatic interaction as a short ranged one by a cut–off method. Usually this is sufficient to produce physically meaningful results, nevertheless is an approximation and can lead to several issues and nonphysical artifacts in those properties or systems that strongly depend on the electrostatic interaction.

The increasing computer power has led to develop more rigorous methods in order to include the long range contribution of the electrostatic interaction, even for very large biological systems. One of the most used method developed to solve this problem is based on the Ewald summation method (ESM) [100] and it is called particle mesh Ewald (PME) method [101, 102]. Briefly, the ESM relies on the possibility to split the electrostatic summation of a periodic lattice into a short and a long range part. In the PME method the short range contribution is directly computed with a cut–off method while the long range part is calculated in the Fourier space using a 3D fast Fourier transform algorithm (3DFFT). This is possible because all charges in the system are assigned to a discrete grid points in space. The grid space binning, together with the cut-off, is a specific parameter which is included in the FF. For a more complete discussion about the advanced methods developed to treat the electrostatic interaction the reader is addressed to the review by Cisneros *et al.* [103].

CHARGE REPRESENTATION Even if some methods, such as the PME one, have been developed to speed up the computation of electrostatic contribution, one of the main problems of FFs for biomolecular applications remains the *charge representation*: the way in which charges of atoms or molecules are assigned to the system particles. The problem arises from the necessity to represent the electron cloud and the interaction that generates. Nevertheless, this is crucial for a better description of most electrostatic phenomena. The most common solution is the *atom–centered "partial charge" approximation* in which the full charge density of the molecule is replaced by fractional point–like charges assigned to each atom of the molecule (the q_i in Equation 2.3.2). Traditionally most non-polarizable FFs (like those we will use in this thesis work) assign to each atom of a molecule a fixed partial-charge. The most used procedure for extracting partial-charges from molecular wave functions is based on fitting atomic charges with the molecular electrostatic potential, computed with *ab-initio* calculation such as *density functional theory*. Such representation is believed to be an important source of error in the electrostatic treatment. Moreover, with a fixed charge assignment it is impossible to take into

account those phenomena, like polarization effects, which involve a transfer of charge inside the molecule. The use of off-centered charges and/or higher-order atomic multipoles can significantly improve the treatment of electrostatics even if, it is necessary a good balance between accuracy and performances since the electrostatic problem can rapidly drive to a loss of computational efficiency.

2.3.2 Atomistic force fields

In an atomistic FF each atom of the system is essentially treated as a single interacting unit. The only exception consists of the hydrogen atoms: FFs that treat all hydrogens explicitly are called *all atom*, while those that treat a carbon atom and the relative bound hydrogens as a single interacting site are said *united-atom (UA)*. In atomistic UA FFs we can find the first step to the reduction of the number of DOF, but still keeping the atomistic resolution. Indeed, biological simulations involve a large number of organic molecules, such as lipids or organic solvents, which contain a great number of CH_n moieties, thus an UA model can contribute significantly to reduce the number of DOF of the system and speed-up the simulation. As an example, we can consider a model bio membrane composed of 114 1-palmitoyl-2-oleoyl-*sn*-glycero-3-phosphocholine (POPC) lipids: with an all atom FF we have 15276 atoms, while we have only 5928 atoms with a UA model.

Unfortunately, biological simulations involve a great number of water molecules: generally more than half of the total atoms in the system belong to water molecules. Keeping in mind the great number of atoms and DOF involved in an atomistic simulation, and that the typical time step is 2 fs, the accessible length and time scales, for both all atom and UA models, are still in the order of tens of nanometers and microseconds. For an all atom model, in particular, these could be even less if bonds involving hydrogen vibrate, in which case the time step should be set to 1 fs.

In the literature, one can find different atomistic FFs that have been developed to better reproduce different properties of different classes of systems. Indeed, bonded interactions are usually fitted against experimental crystal structures, vibrational spectra or *ab-initio* simulations, thus there is not a great difference in their parameters. Non–bonded interactions, instead, are fitted on different experimental data, depending on the properties that the FF is developed to reproduce, such as: densities, heat of vaporisations, surface tensions, self–diffusion coefficients, dielectric constants and so on. Usually, the parameterization of the non–bonded interactions involve only the self–interaction terms, thus *combination rules* are needed to compute interactions between different types of atoms. Different FFs use different combination rules. Proper of each FF is also the treatment of the so-called $1-4$ pair interactions: non-bonded interactions between atoms separated by 3 bonds and which participate in a dihedral interaction are reduced by a factor which depends on the FF.

The atomistic FF we will use in this thesis is the OPLS UA model [104, 105] together with the Berger parameters for lipids [106, 107]. Moreover, as we shall see, the missing bonded parameters in OPLS will be taken from the AMBER FF [108, 109]. Both OPLS and AMBER use the geometrical combination rule, that is

the Van der Waals interaction between atom i and j is computed with the following parameters: $\epsilon_{ij} = \sqrt{\epsilon_i \epsilon_j}$ and $\sigma_{ij} = \sqrt{\sigma_i \sigma_j}$. For the $1-4$ interactions, the OPLS UA use a scaling factor of $1/8$ for the Van der Waals interactions and $1/2$ for the electrostatic one. All atomistic simulations presented in this thesis work are performed with the PME method for the long-range electrostatics, with a grid spacing of 0.12 nm. For what concerns the water model we use the extended simple point charge (SPC/E) [110], one of the simplest, powerful and computationally efficient water model. Moreover, all bonds inolving hydrogen atoms were constrained with the LINCS algorithm [111].

2.3.3 Coarse grained force field

Since the atomistic model, introduced before, takes into account all the atoms in a molecule it is obviously the most realistic and accurate FF. Nevertheless, the large number of DOF leads to a loss of computational performance and the atomistic FFs are efficient until the physical properties can be properly sampled on a time scale of microseconds over a length scale of a tens of nanometers. As the time and length scales increase, more and more time is needed to carry out a complete simulation. Unfortunately, many biological processes involving lipid membranes and other organic molecules, including synthetic compounds, take place on much longer time (of the order of microseconds nor milliseconds) and length scales (of the order of tens nanometers).

One possible solution is to *integrate out* some DOF, preserving those that are relevant for the problem in exam: this procedure is called *coarse-graining*. The basic units of coarse grained FFs are called *beads*, each representing a group of atoms or a well defined chemical moiety. The size of the group of atoms that is represented by a single bead determines the degree of coarsening of the FF. Even in this case, all the general features described above apply: functional forms need to be chosen and their parameterization need to be adjusted so as to reproduce the desired target properties. In Figure 13 different levels of coarse-graining are showed.

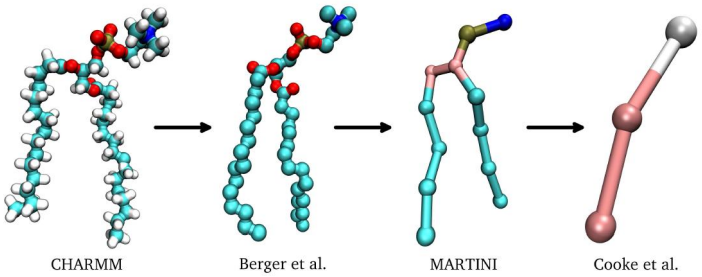

Figure 13: Different levels of coarse-graining of a phospholipid. From left to right increasing levels of coarse-graining. Taken from [112].

The first step in the development of a CG model is the *mapping* procedure. This establishes a link between the atomistic model and the CG one. There is not a unique or correct procedure to perform the mapping because it depends on the

desired coarse-graining level, on the time and length scales that one wants to correctly sample and on the properties one wants to reproduce. For biological applications CG FFs are often designed to reproduce specific thermodynamic properties such as surface tension, free energy of partitioning, free energy of hydration and so on. CG FFs employed in the material sciences (e.g. polymer science) often use as a target the material structural properties.

In general a CG FF is more computationally efficient than an atomistic one for the following reasons

- the DOF of the system are reduced due to the CG procedure with the consequence that a smaller number of interactions and forces has to be computed;
- bead–bead interactions, which result from the removal of finer structural details, are softer than atom–atom interactions. Thus, vibrational modes are slower, and their sampling can be achieved using larger MD time steps than in atomistic simulations;
- softer interactions imply a smoother PEF which leads to faster diffusion.

2.3.4 MARTINI force field

MARTINI is a CG FF developed by Marrink *et al.* [99] for organic solvents and lipids and then extended to proteins [113–115], carbohydrates [116] and a broad class of polymers [117]. MARTINI is based on a chemical building block approach. Such MARTINI blocks or beads represent small chemical moieties and they are extensively calibrated in order to construct a large variety of organic molecules. The FF is based on accurately reproducing the interaction between polar and non–polar chemical compounds. The main target property is the *partitioning free energy* between water and a large number of organic solvents, such us octanol, hexadecane, chloroform and ether.

MAPPING MARTINI uses a four–to–one mapping scheme: it groups four heavy atoms like C, S, O and so on, plus their associated hydrogen atoms, into a single interaction site. Consistently four water molecules are modeled with one MARTINI bead. An example of the mapping procedure including both atomistic and CG descriptions is shown in Figure 14.

There are four main bead types: polar (P), non–polar (N), apolar (C) and charged (Q). Each bead type has a number of subtypes to take into account a more accurate representation of the chemical nature of the moieties due to the underlying specific atomistic structure. These subtypes are distinguished by the hydrogen bonding capabilities: donor (d), acceptor (a), both donor and acceptor (da) and none (0) and/or by their degree of polarity: lowest polarity (1), ..., highest polarity (5).

VAN DER WAALS INTERACTIONS The functional form describing pairwise Van der Waals interaction is a Lennard–Jones $12-6$ potential. For most beads the σ parameter is set equal to 0.47 nm except for the Q–C_1 and Q–C_2 interactions

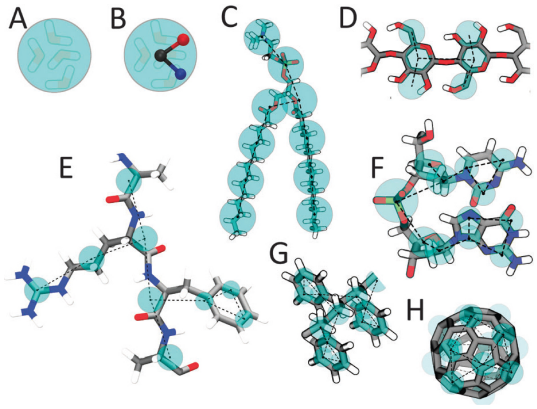

Figure 14: MARTINI mapping on top of atomistic structures of some molecules: MARTINI CG beads are shown as cyan transparent beads overlaying the atomistic structure. (A) Standard water bead, (B) polarizable water bead, (C) DMPC lipid, (D) Polysaccharide fragment, (E) Peptide, (F) DNA fragment, (G) Polystyrene fragment and (H) Fullerene molecule. Taken from [118].

for which $\sigma = 0.62$ nm. This is consistent with reproducing the hydration shell when a charged bead (Q) is dragged into an apolar medium. The strength of the interactions is instead dived into ten levels from $\epsilon = 5.6$ kJ/mol (level O) to $\epsilon = 2.0$ kJ/mol (level IX). The association matrix of the interaction strength with each MARTINI beads is shown in Figure 15.

		Q				P					N				C				
	sub	da	d	a	0	5	4	3	2	1	da	d	a	0	5	4	3	2	1
Q	da	O	O	O	II	O	O	O	I	I	I	I	I	IV	V	VI	VII	IX	IX
	d	O	I	O	II	O	O	O	I	I	I	III	I	IV	V	VI	VII	IX	IX
	a	O	O	I	II	O	O	O	I	I	I	I	III	IV	V	VI	VII	IX	IX
	0	II	II	II	IV	I	O	I	II	III	III	III	III	IV	V	VI	VII	IX	IX
P	5	O	O	O	I	O	O	O	O	O	I	I	I	IV	V	VI	VI	VII	VIII
	4	O	O	O	O	O	I	I	II	II	III	III	III	IV	V	VI	VI	VII	VIII
	3	O	O	O	I	O	I	I	II	II	II	II	II	IV	IV	V	V	VI	VII
	2	I	I	I	II	O	II	II	II	II	II	II	II	III	IV	IV	V	VI	VII
	1	I	I	I	III	O	II	II	II	II	II	II	II	III	IV	IV	IV	V	VI
N	da	I	I	I	III	I	III	II	II	II	II	II	II	IV	IV	V	VI	VI	VI
	d	I	III	I	III	I	III	II	II	II	II	III	II	IV	IV	V	VI	VI	VI
	a	I	I	III	III	I	III	II	II	II	II	II	III	IV	IV	V	VI	VI	VI
	0	IV	IV	IV	IV	IV	IV	IV	III	III	IV	IV	IV	IV	IV	IV	IV	V	VI
C	5	V	V	V	V	V	V	IV	IV	IV	IV	IV	IV	IV	IV	IV	IV	V	V
	4	VI	VI	VI	VI	VI	VI	V	IV	IV	V	V	V	IV	IV	IV	IV	V	V
	3	VII	VII	VII	VII	VI	VI	V	V	IV	VI	VI	VI	IV	IV	IV	IV	IV	IV
	2	IX	IX	IX	IX	VII	VII	VI	VI	V	VI	VI	VI	V	V	V	IV	IV	IV
	1	IX	IX	IX	IX	VIII	VIII	VII	VII	VI	VI	VI	VI	VI	V	V	IV	IV	IV

Figure 15: Interaction strength association matrix for the MARTINI bead types and subtypes. Taken from [99].

ELECTROSTATIC INTERACTIONS Electrostatic charges are assigned using the atom–centered approximation, as described in Section 2.3.1. The charges of the MARTINI beads are empirically assigned at the center of the beads and correspond to the net charge of the chemical moiety they represent. Water, for example, is described by a neutral P_4 bead. Van der Waals interactions take into account, effectively, the effects of polarizability together with the use of an implicit medium with a dielectric constant $\varepsilon_r = 15$. However, as we shall see shortly, to avoid problems

with electrostatic screening, especially for lipid membranes for which the dielectric constant in the hydrophobic region is much smaller, Yesylevskyy *et al.* [119] have developed a more sophisticated CG water model, called polarizable water (PW), to take into account a better water behavior.

BONDED INTERACTIONS They depend on the molecule to be represented, usually include bond lengths and angles as harmonic contributions. The former is modeled with a harmonic potential as the first term in Equation (2.3.1). The latter is modeled as a cosine–type harmonic potential. Moreover, especially for ring systems, an improper dihedral angle harmonic potential can be used to prevent out of plane distortion.

SIMULATION PARAMETERS The MARTINI FF was originally developed using a shifted cut–off scheme for both Lennard–Jones and electrostatic potentials with a cut–off radius $r_c = 1.2$ nm. The Lennard–Jones potential was shifted from $r_s = 0.9$ nm to r_c while from $r_s = 0.0$ nm to r_c for the electrostatic potential. Recently the more efficient Verlet cut–off scheme was tested by Marrink *et al.* [118] and used with the MARTINI FF with a cut–off radius of $r_c = 1.1$ nm. Moreover, the treatment of the electrostatic interaction can be safely integrated by the use of the PME method. This new set–up was largely tested by Yesylevskyy *et al.* [119]. In this case the cut–off radius was set to $r_c = 1.2$ nm and the PME grid spacing was set to have a lower bound of 0.12 nm. In all cases a time step $20 \leqslant \delta t \leqslant 40$ is suitable for a great number of applications. It should be clear that changing these simulation parameters must be followed by a new validation of the main properties of the MARTINI FF.

POLARIZABLE WATER Water plays a crucial role in any biomolecular system. It is important to correctly describe its behavior. Since the MARTINI water model does not directly take into account the electrostatic interaction between water and water and between water and the other polar or charged molecules, because it interacts only via Van der Waals interaction, a simple implicit medium is used to take into account the main electrostatic effects of water, screening and polarizability. In reality, however, most biomolecular processes involve charged species moving between regions with different dielectric constants. Due to the change in electrostatic screening in those environments, the strength of the charge-charge interaction also changes. This effect can not be taken into account by implicit medium models. In order to capture the inhomogeneous nature of the dielectric response an explicitly polarizable medium has to be used.

Yesylevskyy *et al.* [119] have developed a polarizable water (PW) model that better describes the real behavior of water. The new water bead consists of three particles instead of one as in the standard MARTINI model. In Figure 16 the topology of the PW and a comparison with the old model is shown. The central particle *W* is neutral and interacts with the other particles in the system only with Lennard–Jones potential. The two additional particles, namely *WP* and *WM*, which are bound to the central one, carry a positive and negative charge

(standard model) (PW model)

Figure 16: Schematic representation of the PW bead. Shaded orange spheres correspond to the Van der Walls radii of the central neutral particle *W*. The blue particle is the positively charged while the red is the negatively charged.

$|q| = 0.46e$ respectively, where $e = 1.60217653(14) \cdot 10^{-19}$ C is the unit electron charge. They interact with other particles in the system by the Coulomb interaction only. The bonds $W - WP$ and $W - WM$ are constrained to have a fixed distance $l = 0.14$ nm. The electrostatic interaction between *WP* and *WM* inside the same bead are excluded, thus they are invisible to each other and they can rotate around the *W* particle. As a consequence the dipole momentum of the water bead depends on the relative angular position θ of *WP* and *WM*: it can vary from zero ($\theta = 0$) to $2ql$ ($\theta = \pi$). A harmonic angle potential with equilibrium angle fixed to $\theta_0 = 0$ and a force constant $k_\theta = 4.2$ kJ/(mol rad^2) is added to control the rotation of *WP* and *WM* particles around the *W* particle, so to adjust the distribution of the dipole momentum. The value of the equilibrium angle is consistent with the fact that in an apolar medium the total dipole momentum of a water molecule is zero.

Since in this model the screening and polarization effects are treated explicitly the global dielectric constant is then reduced from $\varepsilon_r = 15$ to $\varepsilon_r = 2.5$. Moreover, since the PW beads attract each other stronger then the standard water beads (P_4 type), because of the additional electrostatic interactions, the strength ϵ_{WW} of the Lennard–Jones interaction between *W* particles must be reduced. The same apply to the cross interaction terms between *W* particle and the other MARTINI beads. For these terms, the Lennard–Jones strength is 95% of the I level. Instead, σ remains unchanged to 0.47 nm. With these new interaction terms Water properties, especially the hydration free energy are reproduced satisfactory. Moreover, in order to recover the correct partitioning behavior, the self terms between Q type beads are generally decreased; while the cross terms are generally increased. In Figure 17 a summary of the new interaction terms between Q type beads and the other beads is shown.

The parametrization of q, k_θ and ϵ_{WW} are obtained, in addition to the basic target properties of the MARTINI FF, also trying to reproduce the dielectric constant ε_W, density ρ and dipole momentum of a pure water phase. A comparison of the results obtained with the PW, the standard MARTINI water and the experimental data are summarized in Table 1. For more details about the parameterizations and testing methods the reader is addressed to the article by Yesylevskyy *et al.* [119].

Moreover, the authors found that, in addition to the PW model, the use of PME method contributes to a more realistic description of the processes involved in

	POL	Q_{da}	Q_d	Q_a	Q_0	P_5	P_4	P_3	P_2	P_1	N_{da}	N_d	N_a	N_0	C_5	C_4	C_3	C_2	C_1
Q_{da}	**O**	**O**	**I**	**I**	**IV**	**O**	**O**	**O**	**O**	**O**	**O**	**O**	**O**	**III**	**IV**	**V**	**VI**	**VII**	**VII**
	O	O	O	O	II	O	O	O	I	I	I	I	I	IV	V	VI	VII	IX	IX
Q_d	**I**	**I**	**IV**	**III**	**VII**	**O**	**O**	**O**	**O**	**O**	**O**	**II**	**O**	**III**	**IV**	**V**	**VI**	**VII**	**VII**
	O	O	I	O	II	O	O	O	I	I	I	III	I	IV	V	VI	VII	IX	IX
Q_a	**I**	**I**	**III**	**IV**	**VII**	**O**	**O**	**O**	**O**	**O**	**O**	**O**	**II**	**III**	**IV**	**V**	**VI**	**VII**	**VII**
	O	O	O	I	II	O	O	O	I	I	I	I	III	IV	V	VI	VII	IX	IX
Q_0	**II**	**IV**	**VII**	**VII**	**IV**	**O**	**O**	**O**	**I**	**II**	**II**	**II**	**II**	**III**	**IV**	**V**	**VI**	**VII**	**VII**
	O	II	II	II	IV	I	O	I	II	III	III	III	III	IV	V	VI	VII	IX	IX

Figure 17: New interaction strength between Q type beads and the other beads. New values in bold font, old values in normal font. POL is the name of the MARTINI bead type associated to particle *W* inside a *PW* bead. Taken from [119].

biomolecular environments. In particular, some interesting results of utility for this thesis work concern a better description of the properties of lipid membranes, as we shall see in Chapter 3.

	PW	MARTINI water	Experimental
ρ [kg/m^3]	1043	1013	997
$\overline{p}$ [D]	4.9	–	4.4[a]
ε_W	75.6	–	78.4
T_{melt} [K]	282	290	273
ΔG^{hyd} [kJ/mol]	−18.7	−18	−27
D_{WW} [10^{-5} cm^2/s]	2.5	2.0	2.3

Table 1: Summary of the results obtained with the PW, standard MARTINI water and the experimental data at $T = 300$ K. $\overline{p}$ is the average dipole momentum of a pure water box and D_{WW} is the self–diffusion coefficient. [a] In order for a comparison to be made, this data is obtained from an atomistic simulation of 1600 SPC/E water molecules and the average dipole momentum $\overline{p}$ is obtained averaging over a groups of four molecules, randomly chosen; see [119] for more details.

2.3.5 Limitations of the MARTINI force field

As we have seen in Section 2.3.3 the CG FFs are computationally advantageous, still a price has to be paid. Although the MARTINI FF is still a fine CG FF, some limitations are shared with other CG models at a fundamental level, such as the chemical and spatial resolution, which are both limited compared to atomistic models. An important issue is the underestimation of the entropy with respect to the atomistic case, that is a consequence of the DOF reduction process. Since in the MARTINI FF the partitioning free energy $\Delta G = \Delta H - T\Delta S$ must be consistent which the experimental data, the intrinsic loss of entropy imply a reduction of the enthalpy contribution. This means that, in most cases, the ratio between the enthalpic and the entropic part of the free energy will not be correct in the MARTINI description. If a NVT ensemble is used the correct potential is the Helmholtz free

energy $\Delta A = \Delta U - T\Delta S$, thus the imbalance is between the internal energy and the entropy.

Another consequence of the use of a CG FF is related to the FES that becomes smoother with respect to the atomistic case. This effectively results in more sampling of the energy landscape in a given time interval, speeding up the dynamics of the system and allowing the use of higher time steps with longer simulation times. However, the speedup is not easily predictable and is not likely to be the same for different systems. Nevertheless, for the MARTINI FF an average scaling factor of four, based on the self-diffusion coefficient of water, is commonly used, of course with some care. Another source of error is due to the choice of masses: since ensemble properties are not affected by particle masses, to increase the efficiency, all the MARTINI beads have the same mass of 72 amu. This affects the dynamics of different molecules, making the time scaling for different systems non-trivial.

A problem involving the Lennard–Jones potential as a model of Van der Waals interactions in MARTINI, is that the steep repulsion leads to an over-structuring of fluids compared to atomistic models. As we can see from Table 1 the direct and most evident implication is the melting point of the standard water that is 290 ± 5 K. A practical partial solution is the use of the so-called "anti-freeze" particles named BP_4 type. The Lennard–Jones interaction between these particles and water is modified with a slightly larger Van der Waals radius parameter, $\sigma = 0.57$ nm and a stronger interaction, which is set to level O. Marrink *et al.* suggest that a mole fraction of $n_{af} = 0.1$ is sufficient to prevent freezing without affecting the other properties of water. Using the PW model these properties improve slightly, see Table 1. For a more comprehensive discussion about the limitations of the MARTINI FF the reader is addressed to refs [118, 120–122].

3 COMPUTATIONAL MODELS

In the first part of this chapter we will present and describe the model of the charged monolayer–protected Au NP developed by Federica Simonelli and co-workers in [123–126]. In the second part we will describe the most important physical and chemical features of cell membranes, along with the characteristic of the CG model used to treat it. In the last part we decribe proteins and the CG model of ubiquitin used to studi the Au NP–ubiquitin interaction. For more details about the Au core used, its properties, equilibrium structure and so forth, the reader is addressed to the work of Lopez-Acevedo *et al.* [127] while for a general discussion about thiolated Au NPs to the work of Häkkinen and collaborators [128–130]. For what concerns cell membranes and biological lipids the reader is addressed to the book by Yeagle [131].

Changing the composition of the organic ligands bound to the Au core, different properties of Au NP can be achieved, such as different net charge, different level of hydrophobicity, different size and so on. Here, we use different ligands depending on the interface and interaction we want to study. Moreover, as we shall see, the Au NP can be functionalized by a monolayer of ligands of the same type, or by a monolayer of two different ligands at a specific composition and surface arrangements. The ligands we consider in this thesis are: the para-mercaptobenzoic acid (pMBA), the 7-methyl-mercaptoundecanoic acid (MMUA), the mercaptoundecanoic acid (MUA), the MUS, two –OH terminated PEG chains with 3 or 7 monomers, the 6-methyl-undecane thiol (MC11) and the OT.

3.1 NANOPARTICLE MODEL

Thiolated Au NPs in the $2-4$ nm range have a well defined molecular structure. Several stable thiolated Au NPs differing in size of the Au core and number of ligands have been synthetized and identified [132] and extensively studied both teoretically and experimentally [128, 133–135]. Monolayer–protected Au NPs have a definite mass and molecular composition, and their metal core structure is stabilized by the covalently bound ligand shell. Ligands are often thiols, as they covalently bind to the Au atoms by $Au-S$ surface bonds, that is a robust crucial in passivating and stabilizing the NP [128–130]. Subtle changes of size, structure, ligand composition and arrangement can affect NP properties such as their chemical or optical properties, important for biomedical sensing and therapeutics. In this thesis work we will consider the $Au_{144}(SR)_{60}$ thiolated Au NP, where R are functionalizing thiol compounds. The equilibrium structure of

the Au core was predicated by *ab–initio* calculations in [127] and also resolved with x-ray spectroscopy [29].

3.1.1 Gold core

The Au core is composed of 144 atoms, it has icosahedral symmetry and it is made of three bulk shells with 12, 42 and 60 atoms, respectively. A surface shell of 30 atoms completes the gold cluster structure. The diameter of the Au core is about 2 nm. 60 S atoms are bound to the Au atoms on the surface through the typical bond structure RS – Au – SR. The shell construction is shown in Figure 18. When

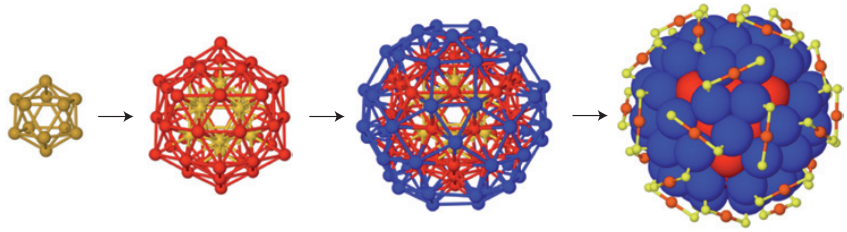

Figure 18: First three frames: the concentric 12–(yellow), 42–(red) and 60–(blue) atom gold internal shell, surrounded (last frame) by 30 gold (red small) and 60 sulfur (yellow small) surface atoms. The R chains, bound to S atoms, are not shown. Taken from [128].

passivated by thiols, the overall size of the NP depends on the length of the chains bound to the S atoms. The monolayer–protected Au NPs we will consider have a total diameter of about 4 nm.

NON–BONDED PARAMETERS Despite the computational cost associated to atomistically describe the NP core, all Au and S atoms are taken into account, even in simulations at CG level. At atomistic level the Van der Waals parameters for Au atoms are taken from Heinz *et al.* [136] ($\epsilon = 22.14487$ kJ/mol, $\sigma = 0.2629$ nm), while for S atoms, the standard OPLS parameters are used ($\epsilon = 1.046$ kJ/mol, $\sigma = 0.355$ nm). Moreover, to prevent the overlap between Au and S atoms a purely repulsive Lennard–Jones potential is added between S and Au ($\epsilon = 0.2324 \cdot 10^{-6}$ kJ/mol). For what concerns electrostatic interactions, Au and S atoms have partial charges, which we obtained from *ab initio* calculations, courtesy of J. Akola. The *ab-initio* simulations reveal that bulk Au atoms have a partial charge of $q = +0.0286e$ while surface Au atoms $q = +0.10273e$, with e the absolute value of the electron charge. S atoms are instead negatively charged with a partial charge per atom of $q = -0.12123e$. The cluster thus has a negative total charge of $-0.9315e$ which is compensated by an opposite charge equally distributed among the first atomic group of each ligand used to functionalise the Au cluster. At CG resolution both Au and S atoms have a purely repulsive interaction, of the form C/r^{-12}, between them and all other particles, including Au and S. In the CG simulations, no charges are attributed to any Au or S atoms in the cluster. This because at CG level charged beads carry unit charge while in this case both Au and S atoms carry a small charge and it vanishes within the CG bead dimension.

BONDED PARAMETERS The classical Lennard-Jones pair potential describing the Au – Au and Au – S interactions within the OPLS model suffers from intrinsic limitations at describing the many-body character of the metal bonding, and thus it may fail at reproducing the transfer of heat from the hot Au core to the ligands via atomic vibrations. We solved this issue by modeling Au – Au and Au – S interactions with an elastic network [125] parameterized using as a target the harmonic vibrational spectrum of the AuNP given by a more reliable many-body model [137, 138]. The optimized elastic network uses two different elastic constants:

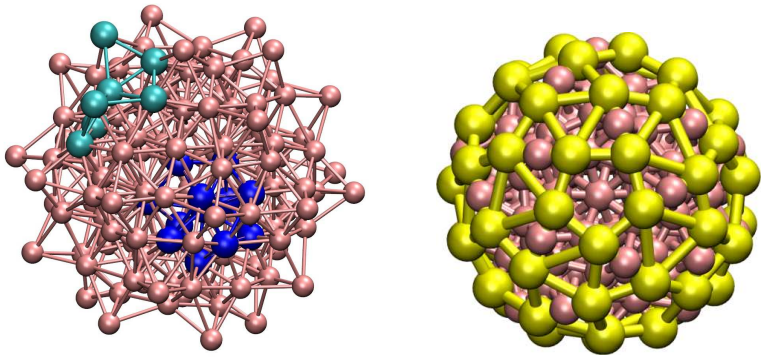

(a) Au elastic network **(b)** Au NP cluster

Figure 19: Left: gold elastic network. In cyan a surface atom and its neighbors; in blue bulk atom and its neighbors. Right: Au NP cluster. The elastic network for both gold and sulfur atoms are represented by sticks. Taken from [123].

$k = 32500$ kJ mol nm^{-2} for Au – Au surface atoms and Au – S bonds and $k = 11000$ kJ mol nm^{-2} for Au – Au bulk atoms. To maintain the structure of S atoms stable, an elastic network is added also between S – S atoms with $k = 25000$ kJ mol nm^{-2} for atomistic simulations and $k = 1250$ kJ mol nm^{-2} for CG simulations. All the elastic constant are summarized in Table 2. The equilibrium distances are derived from *ab–initio* data in [127]. A gold atom is considered as a bulk atom if it has at least nine gold neighbors, otherwise it is considered as a surface atom. Two gold atoms i and j are neighbors if their distance is $r_{ij} \leqslant 0.35$ nm. Instead, two sulfur atoms are considered neighbors if their distance is $r_{ij} \leqslant 0.55$ nm, i.e. each S atom has at least five neighbors.

Bond	k [kJ/(mol nm^2)]
Au – Au (bulk)	11000
Au – Au (surface)	32500
Au – S	32500
S – S	25000 (1250)

Table 2: Summary of the bond constants for the elastic network of the NP core. In parentheses the value used in CG simulations; if not indicated, the value is the same. Data from [123, 125].

3.1.2 Atomistic ligands

The ligands used and modeled at atomistic resolution are: the hydrophilic para-mercaptobenzoic acid (pMBA), 7-methyl-mercaptoundecanoic acid (MMUA), mercaptoundecanoic acid (MUA), mercaptoundecane sulfonate (MUS) and two –OH terminated polyethylene glycol (PEG) chains with 3 or 7 monomers, namely PEG3 and PEG7, and the completely hydrophobic 6-methyl-undecane thiol (MC11) and octanethiol (OT) ligands. Their chemical structure is shown in Figure 20 while in Figure 21 it is shown their atomistic UA representation. Figure 22 shows the configuration assumed by the PEG7–Au NP in the water phase; the other Au NP configurations are shown in Figure 31 of the Chapter 4. The parameterization of the ligands is done following the standard OPLS–UA rules [104, 105, 139, 140] with missing parameters taken from the AMBER FF [108, 109]. The non-bonded parameters (including partial charges) and dihedral angles for the sulfonate group in MUS are taken from the parameterization of Lopes and collaborators [141]. For what concerns the PEG chains, three OPLS–compatible parameters were tested, from Fuchs *et al.* [142], Fischer *et al.* [143] and Weiner *et al.* [108]. For each parameter set, a MD simulation was performed with one PEG molecule composed by 28 monomers, solvated with about 30000 SPC/E water molecules. We calculated the chain radius of gyration and compared it, via extrapolation at low molecular weight, with the experimental data by Kawaguchi *et al.* [144]. The model based on Weiner was selected as it was the one matching well the experimental data.

The addition of the side methyl group in the MMUA and MC11 ligands assure that the final configuration assumed by the functionalized NP in the water phase

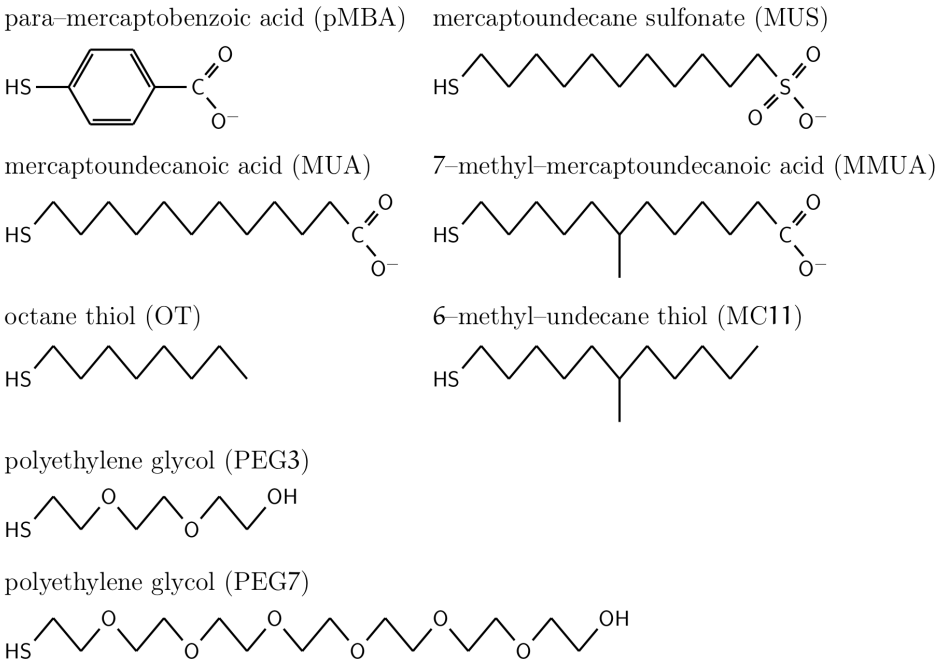

Figure 20: Chemical structure of used ligands.

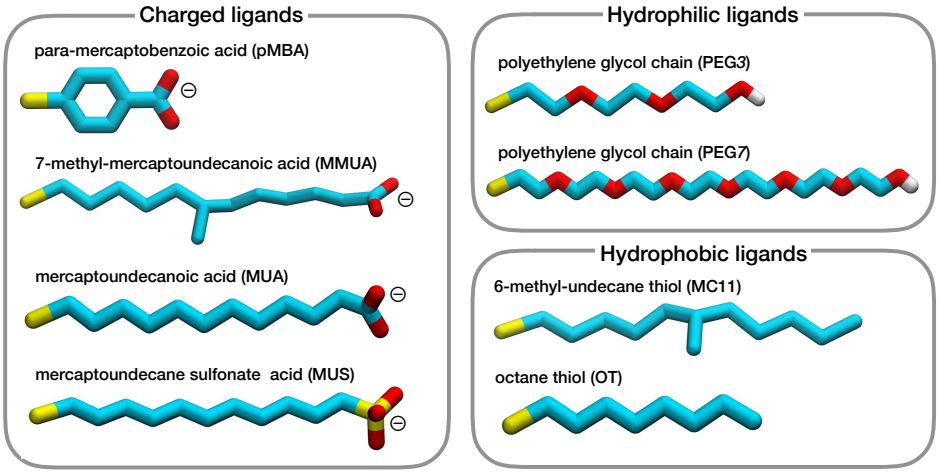

Figure 21: Snapshot of the atomistic UA ligands. S in yellow, C in cyan, O in red and H in white.

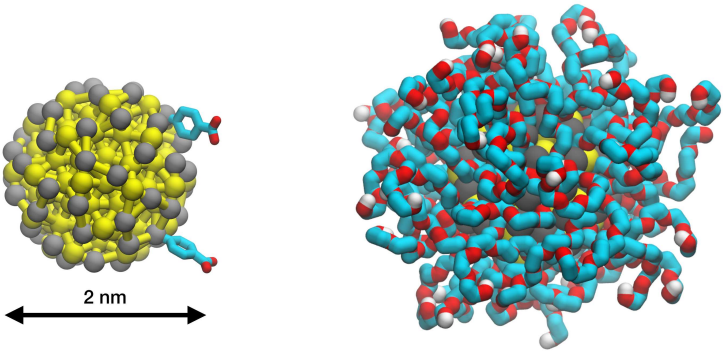

Figure 22: Left: The Au–S core of the NP, Au in yellow and S in gray; the sticks represent the elastic network between Au–Au, S–S and Au–S atoms. Only two functionalizing ligands are shown. Right: Snapshot of a hydrated Au NP functionalized by PEG7 (water is not shown for clarity). For a view of the other NPs in water phase, the reader is addressed to Figure 31 in Chapter 4.

is, as much as possible, isotropic and spherical, i.e. the methyl group is needed to prevent the ordered packing of the alkane chains on the NP surface, as shown in Figure 23 for the MC11 case.

3.1.3 Coarse grained models

The ligands used at CG resolution are the MUA, MUS and the OT, as shown in Figure 24.

OT MODEL Two MARTINI beads of type C_1 model the eight carbon atoms of the OT backbone and their hydrogen atoms. The chemical structure and the resulting CG MARTINI model is shown in Figure 24a. The first bead of each OT ligand is bound to a sulfur atom via a harmonic potential with a bond constant

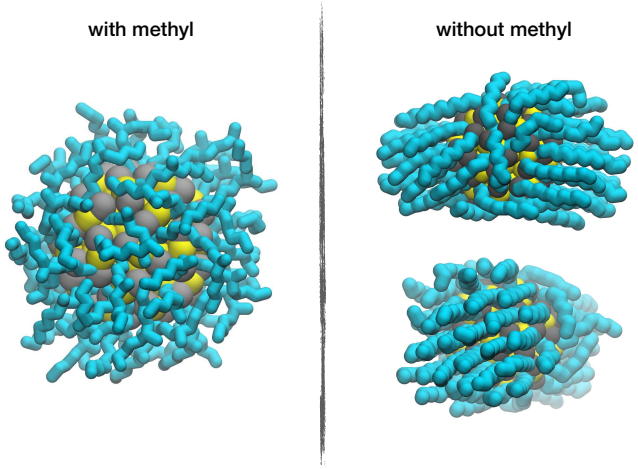

Figure 23: Comparison between the final configuration of a hydrophobic NP in water: in the left functionalized with the 6-methyl-undecane thiol (MC11) and in the right with the undecane thiol (C11). The addition of the methyl group in the alkyl chains is needed to prevent the ordered packing of the alkane on the NP surface.

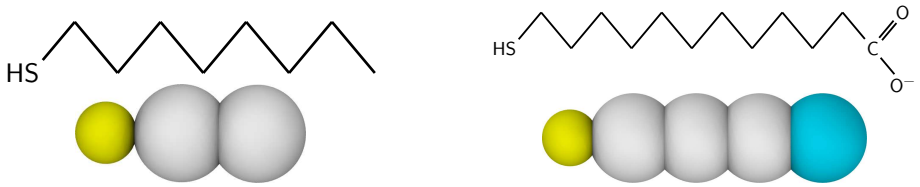

(a) OT ligand **(b)** MUA ligand

Figure 24: Top. Chemical structure of OT (a) and MUA (b). Bottom. CG MARTINI model (white: C_1 bead, cyan: Qda negatively charged bead and yellow: sulfur atom).

of 1250 kJ/(mol nm^2) and equilibrium length of 0.47 nm. The second bead is connected to the first by the same bond potential. An angle potential as in Equation (2.3.1) is used among the three particles. Parameters are fixed in accordance with the MARTINI parameters for alkanes.

MUA AND MUS MODEL Three MARTINI beads of type C_1 model the hydrophobic chain of the MUA ligand. The charged group is modeled as a Qda bead with a charge of $-e$. The chemical structure and the resulting CG MARTINI model is shown in Figure 24b. Even in this case the first bead of a MUA ligand is bound to the sulfur atom through a harmonic potential with the same parameter: bond constant of 1250 kJ/(mol nm^2) and equilibrium length of 0.47 nm. The same potential is used to bind all other beads to the previous one. An angle potential as in Equation (2.3.1) is used among the sulfur atom, the first C_1 and second C_1, among the first, the second and the third C_1 beads and so on for all four beads. Parameters are fixed in accordance with the MARTINI parameters for alkanes. Since the MUS ligand has a negatively charged terminal group similar to the carboxylate one, the CG model for MUS does not differ from the MUA model.

LEVEL OF HYDROPHOBICITY The NP core can be functionalized with both ligands varying the ratio between the OT and MUA or MUS ligands, thus reaching different levels of hydrophobicity. Two surface compositions will be considered in this thesis

work: (MUA:OT 1:1) and (MUA:OT 2:1). This choice is due to the possibility to compare to previous experimental and simulation data [47, 145–147].

SURFACE ARRANGEMENTS The ligands on the Au NP surface can be arranged in two possible ways: randomly or with a predetermined scheme. We will consider both NPs with a random ligand arrangement and NPs with a striped ligand arrangement. The striped scheme is obtained dividing the NP surface into three stripes: the external two stripes are covered with MUA ligands while the central with OT ligands, thus the NP show large hydrophobic patches. The random case, instead, shows small patches. For this thesis work, we consider NPs with both small or large patches, as shown in Figure 25.

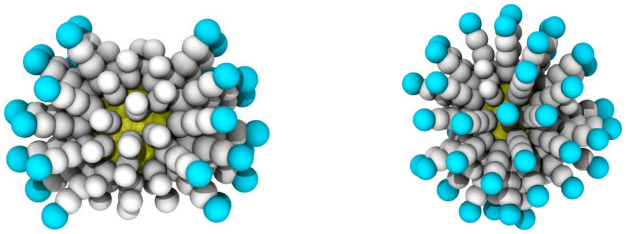

(a) large patches **(b)** small patches

Figure 25: AuNP with different ligand surface arrangements. From left to right: (MUA:OT 1:1) with large patches and (MUA:OT 1:1) with small patches. Hydrophobic beads are shown in white while the negatively charged beads are cyan.

3.2 CELL MEMBRANES

The cell membrane or cytoplasmic membrane is a biological membrane whose main function is to compartmentalize the biological environment into two well defined, though not independent, subsections: the interior of the cell and its external environment. The membrane controls the in–out flow of ions and other chemical compounds which are necessary to carry out all "life reactions" taking place inside the cell. For these reasons, from an evolutionary point of view, it is believed that the appearance of the cell membrane was one of the necessary ingredients to the development of life. In this section we describe the main characteristic of a cell membrane along with the model that we will use to simulate a lipid membrane at CG level.

3.2.1 Real cell membranes

As we can see from a cartoon of a real cell membrane in Figure 26, the biological membrane is a crowded environment consisting of phospholipids, glycolipids, carbohydrates, proteins and other organic molecules.

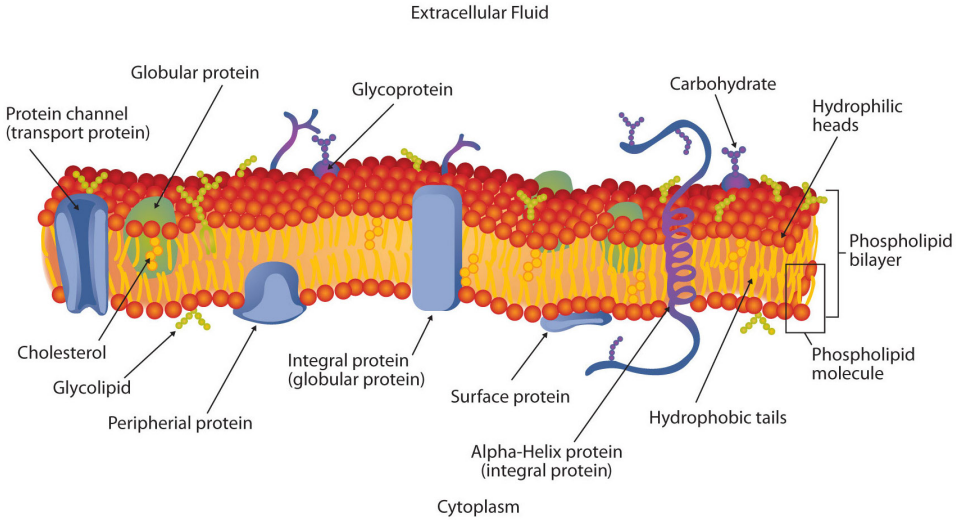

Figure 26: Schematic picture of a cell membrane. In the bilayer, mainly composed of phospholipids, different kinds of proteins ad biomolecules are embedded. Cholesterol and carbohydrates are also present in the membrane.

The plasma membrane by mass is essentially composed by half lipids and half proteins. Most of the lipids that constitute animal membranes are a particular type of lipids, called *phospholipids*. They are made of a neutral (polar) or charged head, which is hydrophilic and one or two fatty acid hydrocarbon chains, often called lipid tails, which are instead hydrophobic. Phospholipids are *amphiphilic* molecules. This amphiphilic nature, through the *hydrophobic effect*, plays a key role in the membrane formation. In fact when we put a relevant concentration of phospholipids in a water solution they tend to *spontaneously* self–organize in a *ordered* state that minimizes the Gibbs free energy. Thus the lipid tails tend to cluster in order to minimize the hydrophobic surface in contact with water. Instead, the polar heads tend to make favorable bonds with water molecules. The final assumed configurations depend on the lipid concentration, on the temperature of the solution and the salt concentration. The one that constitutes a cell membrane is called *phospholipid bilayer*: a thin polar membrane made of two layers of lipid with a hydrophobic core (composed by the hydrophobic lipid tails) and two hydrophilic surfaces (composed by the hydrophilic lipid heads facing toward the water). A schematic representation of a bilayer is shown in Figure 26 with different proteins and biomolecules embedded. The two lipid layers that made a bilayer of a cell membrane are called *leaflets*.

A real lipid bilayer often contains hundreds of different lipid species. They differ in the length of the hydrocarbon chains, in the degree of unsaturation, *i.e.* in the number of double bonds in the hydrocarbon chains, and in different chemical composition of the head that can be neutral (polar) or charged. There are two main classes of phospholipids that make a cell membrane of animals: glycerophospholipid (phosphatidyl–choline, phophatidyl–ethanolamine, phophatidyl–serine, phosphatidyl–serine) and phosphosphingolipids (sphingomyelin). In the former group the lipid tails are bound to a glycerol group while the latter do not have

glycerol and the lipid tails have a backbone of sphingoid bases, absent in the former. These five types take into account for more then half of the lipids in most membranes.

The cell membrane has quasi–liquid properties at physiological temperature. This is in part due to some disorder in the alignment of the lipid tails produced by the presence of unsaturated chains. Another contribution arise from the area occupied by the lipid heads which determines the distance between the hydrocarbon chains. This fluid character makes the lipid bilayer like a solvent in which the other molecules (lipids and proteins) are dissolved and are free to diffuse. Moreover, lipids themselves can move in different ways. The main movements and the associated time scales are summarized as follows

- lipids conformational changes (few nanoseconds);
- lipids protrusions out–of–plane (tens of picoseconds);
- diffusion within a leaflet (order of tens of nanoseconds);
- bilayer undulation and thickness involving collective motion of many lipids (more than tens of microseconds).

There are also many rare events that take place on the order of hours or even days, such as lipid flip–flop, in which a lipid flips from one leaflet to the opposite one; ion translocation; electroporation by water, for example due to a cross membrane ion imbalance, in which water translocates across the bilayer; water assisted ion permeation via formation of a *water–finger* and so forth.

For what concerns the length scales, the bilayer thickness is determined by the length of the lipid tails and their degree of unsaturation. Typically the hydrophobic region is ~ 3 nm thick while each hydrophilic region is ~ 1 nm thick. Hence the typical bilayer thickness is around $\sim 4 \div 5$ nm.

3.2.2 Model cell membrane

The cell membrane is an extremely complex environment due to a large number of different biological molecules (lipids, proteins and so on) that compose and reside in the membrane. The model membranes we will consider in this thesis will be composed of lipids only. This choice is dictated by three main reasons. First, current models and computational power can not aim at reproducing the complexity of a real plasma membrane [148]. Second, the use of a model system allows to tackle fundamental questions concerning the physical and molecular mechanisms of interaction between NPs and membranes. Last but not least, the model membrane we will consider resembles closely the model membranes used in a number of experimental and simulation results.

In the bilayer model we will use, we consider a model biological membrane consisting of 1-palmitoyl-2-oleoyl-*sn*-glycero-3-phosphocholine lipids, whose chemical structure is shown in the top of Figure 27. It is a zwitterionic glycerophospholipid of type phosphatidyl–choline whose head is made of a phosphate (PO_4^-) and a

choline ($C_5H_{14}NO^+$) groups. It has two hydrocarbon chains: one is a saturated chain (palmitoyl) and the other is an unsaturated chain (oleoyl). The head groups and tails are both bounded to the glycerol group ($C_3H_8O_3$).

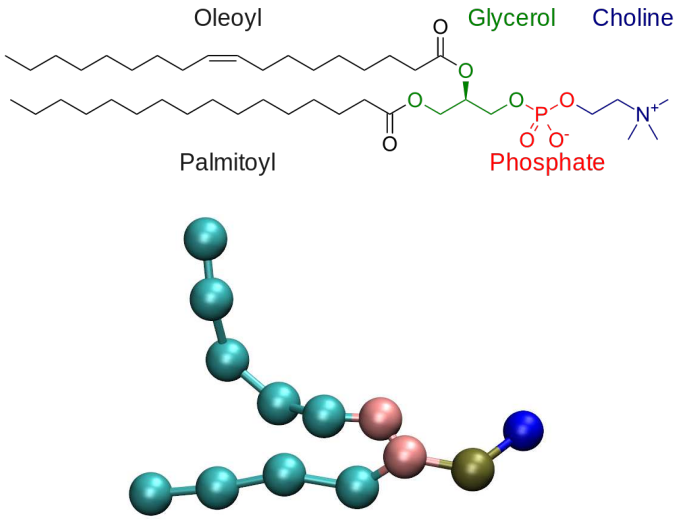

Figure 27: Top: chemical structure of a POPC lipid. Bottom: MARTINI CG model. The tan bead is the phosphate group, choline is in blue, the two pink beads represent the glycerol group and the hydrophobic chains in cyan.

CG MODEL The lenght scale associated to a real cell is of the order of one to tens of micrometers. Thus, it is clear that the number of lipids that constitute a real cell membrane is enormous and it is impossible to take into account an entire cell membrane in a MD simulation. A first approximation is to consider only a small patch of a model bilayer. In our investigations of NP–membrane interactions, given the dimension of a protected Au NP of about 4 nm, we need a bilayer patch on the lenght scale of tens nanometers, says 160 nm^2. Since, the medium area per lipid of a pure POPC bilayer is about 0.65 nm^2, we need a total of about 500 lipids. The total number of particles to be included in a atomistic simulation (excluding hydrogen atoms) are about $3 \cdot 10^4$. Even more, looking at NP–membrane interactions we need also a time scale of tens of microsecond if not more. This has a very expensive computational cost at atomistic level and the range of phenomena which can be studied on the time scale accesible with an atomistic simulation are very limited, calling for the adoption of a CG approach.

MARTINI MODEL As described in Section 2.3.4, we will use the CG MARTINI FF for lipids [99]. The MARTINI model for the POPC lipid maps the choline and the phosphate groups into two beads of type Q_0 and Qa negatively and positively charged, respectively. The saturated tail is modeled with four beads of type C_1 while the unsaturated tail is built up of four C_1 beads and one C_3 bead that corresponds to the unsaturated group of atoms. The glycerol group is modeled

	STD[a]	PME[b]	PME + PW[b]	atomistic[b]
D [10^{-8} cm^2/s]	~ 62	43.3 ± 0.7	31 ± 1	8.0 ± 0.4
$\overline{A}$ [nm^2]	0.65	0.630	0.635	0.688
$\bar{t}$ [nm]	4.16	4.29	4.26	3.66

Table 3: Summary of main properties of a pure POPC bilayer in comparison with different models. D is the lateral diffusion coefficient of a lipid. $\overline{A}$ is the average area per lipid. $\bar{t}$ is the bilayer thickness as the average distance of the phosphate groups. [a] Data from [149]. [b] Data from [124].

with two beads of type N_a. A comparison between the chemical structure and CG model is shown in Figure 27.

MODEL ACCURACY The standard MARTINI FF is able to capture the main physical properties of a lipid bilayer. These properties include the area per lipid, the distribution of groups across the membrane, the trend of the bending and the area compression moduli in function of the lipid composition and the unsaturation degree of the lipids, the stress profile across the membrane, and many other as better described in [99, 118]. Some of the main properties of a pure POPC bilayer are shown in Table 3 in a comparison among different models.

As any model, the MARTINI model has its weaknesses. Most of the properties strongly depending on electrostatic interactions are not well described. These are ion translocation, electroporation of the membrane by water, due to a cross membrane ion imbalance, water-helped ion permeation and many other water defects inside the membrane as better described in the works of Marrink [118] and Yesylevskyy [119]. As we have seen in Section 2.3, this is because the standard MARTINI FF does not take into account long range electrostatic interactions. To overcome this problem the use of the PME method and the PW model, as outlined in Sections 2.3.1 and 2.3.4, are crucial to better describe the processes that involve the interaction between ions, water and lipid bilayer.

3.3 PROTEINS

Proteins are a wide class of biological polymers that are fundamental to every aspect of cell life. The base units of proteins are called amino acids. In nature many different amino acids exist but only 21 are necessary to the eukaryote translational machinery to assemble proteins. Of these, 20 are genetically-encoded: they are shown in Figure 28. The amino acids are characterized by the same topology: a backbone, which is the same among the different amino acids and a side chain, which is proper of each amino acid. The backbone is composed by a central carbon, called C_α, to which an aminic $-NH_2$ (N-terminus) and a carboxylic –COOH (C-terminus) groups are bound. Typically, the N- and the C-termini of a protein in a water solution are positively and negatively charged, respectively.

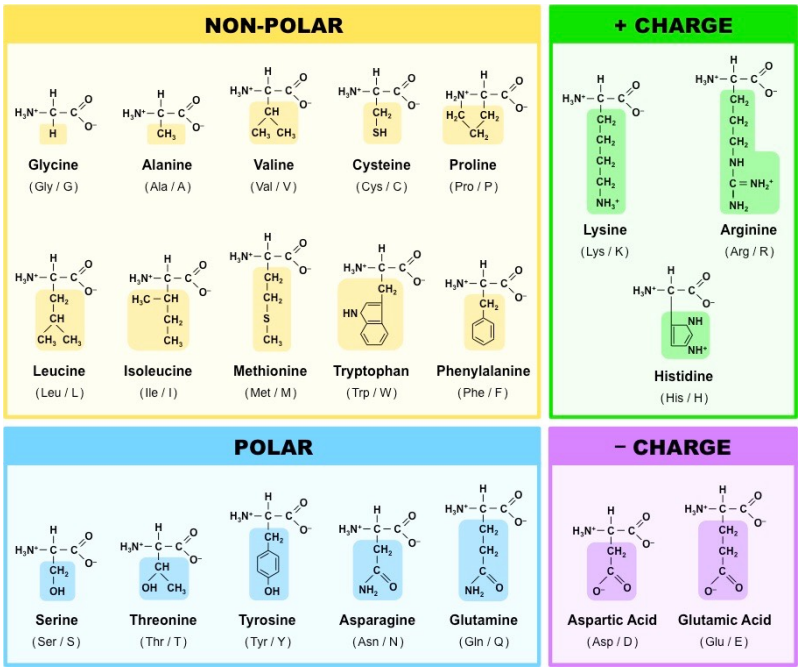

Figure 28: Chemical structure of the 20 genetically–encoded amino acids.

The sequence of amino acids that identify the protein is called *primary structure*. Once the synthesis of a protein ends, the sequence of amino acids starts to fold into the 3D functional structure of the protein, which is called *tertiary structure* or folded state. The tertiary structure controls the basic function of proteins and the transition from the primary structure to the folded state is called *protein folding*. This process is essentially guided by the external environment (other proteins and/or enzymes) that stabilize the folded state through salt bridges, hydrogen bonds, disulfide bonds, and even posttranslational modifications. The tertiary structure is made of regular sub-structures, namely α-helces and β-sheets. These, are called *secondary structures*, which are defined by patterns of hydrogen bonds between the backbone peptide groups. Some proteins are made of two or more sub-units which constitute the monomers of the *quaternary structure* of these proteins.

UBIQUITIN It is a small protein that exists in all eukaryotic cells and occurs ubiquitously. The protein consists of 76 amino acids, it has a molecular mass of about 8.6 kDa and it displays a α-helix and one-β sheet, as shown in Figure 29a. The atomistic structure of human ubiquitin is available in the protein data bank (PDB) which is determined via x-ray diffraction crystallography [150] at a resolution of 0.18 nm. The protein is neutral, but it has the C and N termini, respectively, negatively and positively charged.

MARTINI MODEL OF UBIQUITIN We built the MARTINI CG model of the ubiquitin protein with the use of the *martinize* script, freely available on the MARTINI website. The model is based on the polarasible version of the ELNEDIN MARTINI CG FF for proteins [113–115]. Briefly, according to the philosophy of the original version

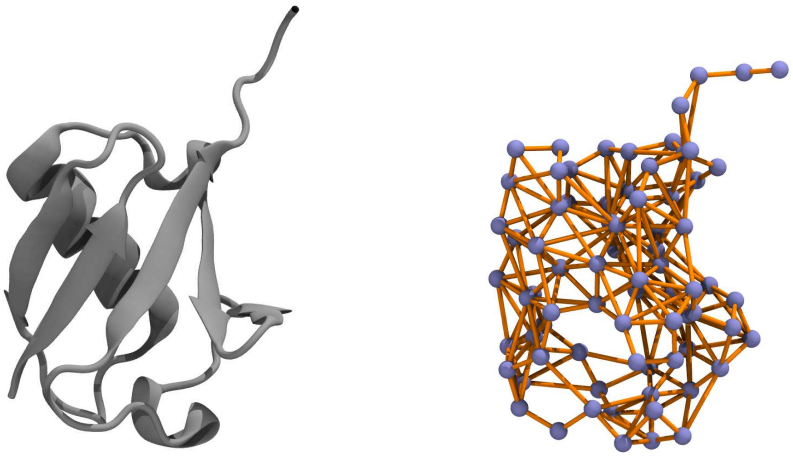

(a) atomistic staurcture **(b)** MARTINI structure

Figure 29: (a) Atomistic structure of the ubiquitin protein with the α-helix behind the β-sheet. (b) MARTINI CG mapping with the ELNEDYN elastic network (orange sticks) superimposed to the backbone beads (light blue). Side chain beads not shown.

of MARTINI [99], one bead is used to model the backbone of each residue and zero to four beads are used to model their side chain, depending on the residue type [113], as shown in Figure 30. Proteins, in its CG representation, cannot change

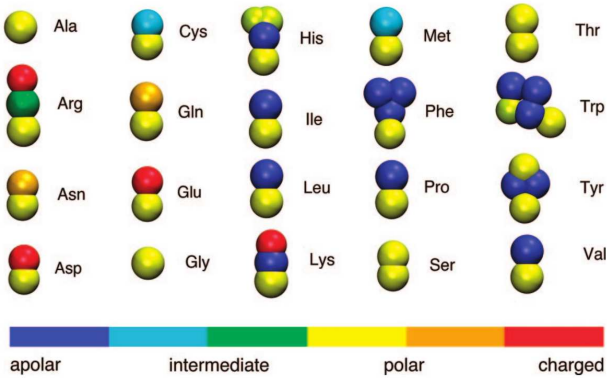

Figure 30: Mapping of all amino acids. Taken from [113].

their secondary structure which is fixed by bonded interactions. To improve the structural and dynamical properties of CG proteins, including their collective motions, the CG MARTINI model has been combined with an elastic network [114]: the representation that emerges is based on both structural and thermodynamic properties and is termed ELNEDIN. In the ELNEDIN model the position of the backbone beads coincides with the C_α position. As shown in Figure 29b, the elastic network is superimposed to the backbone beads and involves only backbone beads within a cut-off distance r_c which could be tuned together with the elastic constant K to reproduce the atomistic vibrational properties of the protein of interest. In that case, we choose to use the default parameters [114]: $r_c = 0.9$ nm and $K = 500$ kJ/(mol nm^2).

Moreover, we use the polarazable version of the ELNEDIN FF for proteins [115, 119]. This choice is guided to two principal reasons: *i.* we want to study the

interaction between a charged Au NP and ubiquitin, a hydrophilic protein, thus it is crucial to correctly treat the electrostatic interaction; and *ii.* it is well known that the standard MARTINI FF tend to overestimate the hydrophobic interaction [120, 122] with the tendency to over stabilize cluster of organic molecules, especially if proteins are involved [151]. Thus, the necessity to use the polarizable version and overcome these limitations. In the polarizable version for proteins [115], follow the philosophy of the PW model, each polar or charged bead is associated, respectively, to two or one charged dummy particle. Dummy particles can interact with all other beads only via Coulomb interaction. They have a fixed bond with the Van der Waals interacting centre: rotating around it they can adjust the bead polarization depending on the surrounding environment. The partial charge associated with the dummy particle is $\pm 1e$ if the bead is charged and it represents a charged group or $\pm 0.36e$ if the bead is neutral and represents a neutral but polar group. Furthermore, the mass of dummy particles is set to 36 u.m.a. The mass of the Van der Waals interacting centre is set to 36 u.m.a. if the polarizable bead is charged or 0 if it is neutral.

4 EFFECT OF LIGAND HYDROPHOBICITY ON THE THERMAL CONDUCTANCE OF IRRADIATED NANOPARTICLES

As we have discussed in the introduction, inorganic NPs are multivalent agents for different biomedical applications [66]. NPs can effectively and stably accumulate in tumor tissues. They can permeate cell membranes. Their facile surface chemistry allows for many different functionalizations. Their optical properties can be used in photothermal therapies or bio-imaging applications. Photothermal applications, in particular, are currently the object of intense research efforts, aimed at the optimization of the NP optical response, as well as at the minimization of their toxic effect [152, 153].

The localized surface plasmon resonance of Au NPs functionalized with biocompatible ligands can be efficiently used to adsorb light in the near-infrared window and convert it into heat, which is transferred to the surrounding tissue [66, 71]. This light-to-heat conversion has been largely exploited to improve the performances of bio-sensing applications [65] and photothermal therapies [64]. For example, Au plasmonic NPs, which show good biocompatibility, have already entered clinical trials for the treatment of lung or prostate cancer [67]. The capability of Au NPs to convert light into heat can be exploited also for drug delivery applications: polymer capsules or liposomes loaded with NPs have been shown to release their cargo upon irradiation [78]. Moreover, as near-infrared radiation can penetrate biological tissues for several centimeters, the ability to deliver Au NPs to a target unhealthy tissue allows for the localized release of heat in the region to be treated, this is the physical conpect in which many photothermal cancer therapies rely in. Among the many photothermal therapies, the most promosing one if the photoporation: in a typical setup, plasmonic Au NPs coated by organic ligands are stably inserted in the cell membrane and are heated up by a short high intensity laser pulse, inducing nanoscale transient pores in cell membrane, allowing for drug or short inerfering RNA penetration into cells *in vitro* [75, 77].

Regardless of the specific application, the ability to control the temperature profile developed around ligand protected plasmonic Au NPs would guarantee their optimal design [154]. As a matter of fact, the presence of ligands influences the thermal conductance of the nano-bio interface, altering the temperature profile developed around the NP. Therefore, tuning the NP ligand composition to achieve the desired temperature increase at the NP surface, and to limit the damage on the healthy tissue [125], is the ultimate objective for final designing and exploiting plasmonic coated NPs in biomedicine.

The direct experimental measurement of the temperature profile at NP surface is challenging, and it has been attempted by means of the *ad hoc* covalent binding of polymers or quantum dots to the NPs [155]. A less direct approach consists in

the measurement of the interface thermal conductance via optical pump and probe techniques, such as time-domain thermo-reflectance, often applied to extended surfaces. It has been shown that the presence of a ligand layer enhances the thermal conductivity with respect to the bare solid surface in contact with the solvent [37, 156, 157]. The seminal works by Braun and Cahill [158] suggested a dependence of the interfacial conductance on the hydrophobic or hydrophilic nature of the coating ligand layer. The nature of the solvent, the density of covalent bonds at the metal surface and the work of adhesion needed to separate the liquid from the solid are all factors that have been shown to affect thermal conductance [158–160]. There is a general consensus that in the presence of a three-component interface, namely metal–ligand–solvent, the ligand–solvent interface offers the largest thermal resistance [161], thereby playing a major role in the study of heat transfer mechanisms. However, this interface cannot be classified as an ideal solid–liquid nor as liquid–liquid interface, instead it strictly preserves a soft matter nature whose thermal properties are likely to be explained only considering its chemical and physical features at the molecular scale. For this reason, molecular modelling techniques have been adopted to clarify and unveil the most critical phenomena ruling the heat transfer at the ligand–water nanoscale interface. MD simulations have demonstrated a considerable potential to distinguish the specific molecular mechanisms which influence heat conduction and the formation of thermal gradients around NPs. MD studies have proved that stronger Van der Waals interactions favor heat conduction, both at metal–solvent [36, 162] and ligand–solvent interfaces [161, 163]. The collaborative effects of Van der Waals and electrostatic forces, which contribute to the formation of hydrogen bonds between the ligands and the solvent, has also shown to increase thermal conductance at ligand–solvent interfaces [164]. Heat conduction can be enhanced also by the reciprocal alignment of ligands and intercalating solvent molecules [165].

In this chapter, we use MD simulations to investigate the thermal gradient developed around a hot thiolated Au NP in cold bulk water. As we shall see, the shape of the thermal gradient depends on the hydrophobicity of the coating ligands. We show that the temperature profile developing around the hot NP can be explained in terms of interfacial water structure and dynamics. Moreover, in the final part of this chapter, we propose a MD-based approach to predict the thermal gradients based on the knowledge of ligand composition. This could allow for a fast and preliminary screening for the best ligands to coat NPs in tailored biomedical applications.

4.1 NON–EQUILIBRIUM MOLECULAR DYNAMICS SIMULATIONS

We are interested in calculating the temperature profiles generated by an irradiated hot Au NP by means of atomistic non–equilibrium MD simulations. We consider a single Au NP, covalently functionalized by organic thiols. We use 5 different organic thiols as functionalizing agents. These ligands are: two negatively charged ligands: the para-mercaptobenzoic acid (pMBA) and the

7-methyl-mercaptoundecanoic acid (MMUA); two neutral but hydrophilic polyethylene glycol (PEG) chains terminated with a −OH group, made with 3 and 7 PEG monomers, respectively; a completely hydrophobic carbon chain, the 6-methyl-undecane thiol (MC11). In Figure 21 of Section 3.1 it is shown the atomistic representation of the different ligands. In Figure 31 it is shown a snapshot of the functionalized NP in water phase with all ligand types.

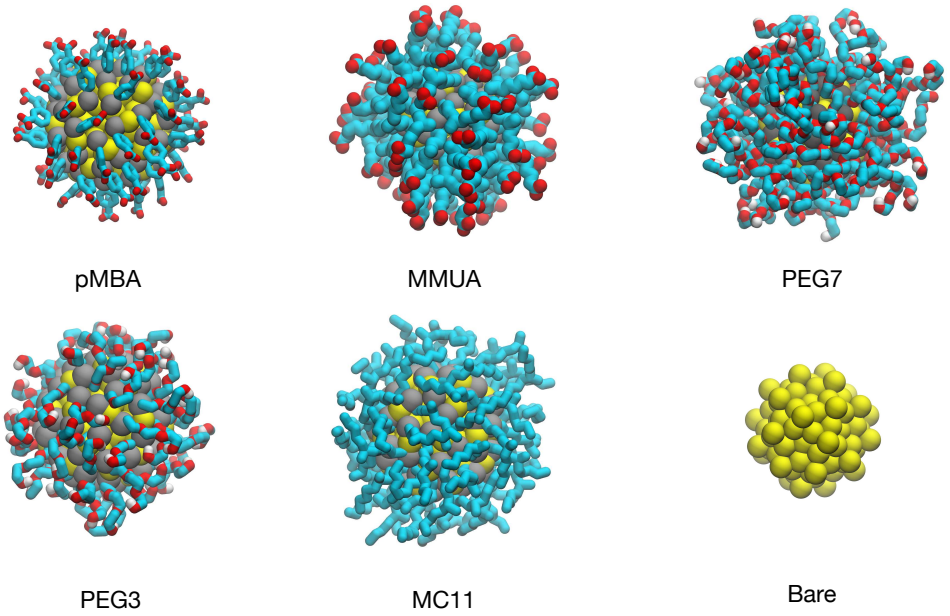

Figure 31: Snapshot assumed by the functionalised Au NPs in the water phase. Water not showed for clarity. Color code as in Figure 21.

As in Tascini *et al.* [36], temperature is controlled in only two spatial regions, hot and cold, by two independent thermostats, while the rest of the system is left un-thermostated. The heat source is represented by the Au atoms of the NP, thermostated at an average temperature of $T_{hot} = 380$ K. The T_{hot} temperature we chose is lower than the typical melting temperature of Au NPs of this size [166]. The heat sink corresponds to a shell of bulk water molecules, thermostated at $T_{cold} = 300$ K. In Figure 32 it is shown the simulation box used for all non–equilibrium simulations: it has a volume of about 2000 nm^3 and it is composed of a Au NP placed at the center and solvated with SPC/E water. To obtain a smooth temperature profile each profile is obtained by averaging, along a 80 ns trajectory, the temperature profiles collected every 2 ns, as better detailed in Section 4.4.

TEMPERATURE PROFILES In the top right panel of Figure 32, we show the temperature profiles as a function of the distance from the NP COM. The bare NP case, as expected, shows a single large temperature drop at the Au–water interface, $\Delta T_{AuW} = 48.7 \pm 0.7$ K. When the NP is functionalized by ligands, we can distinguish two main behaviors depending on the hydrophobicity of the ligand: in presence of a hydrophilic ligand, the largest temperature drop is recorded at the Au–ligand interface, ΔT_{AuL} (light-red shaded area in Figure 32). The tem-

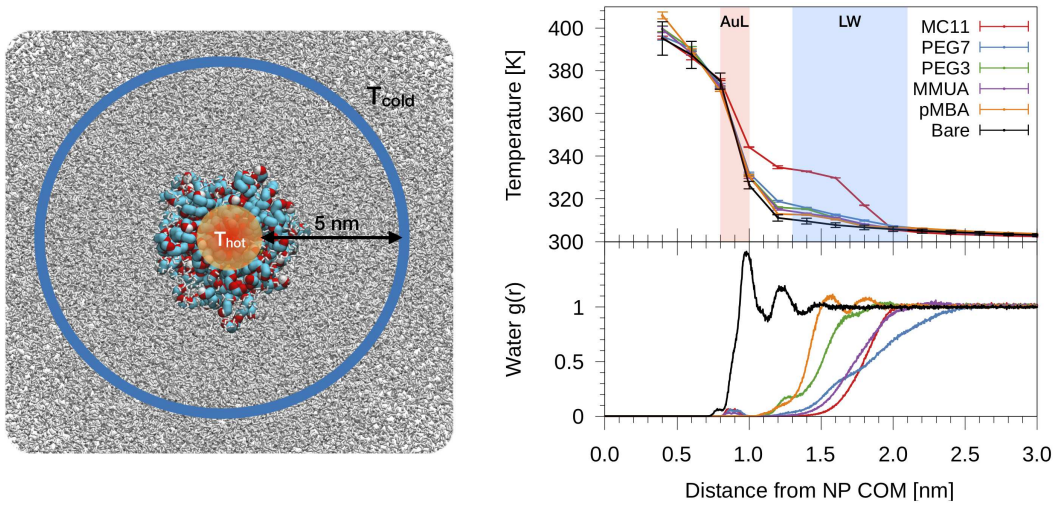

Figure 32: Left: Simulation box used for the non-equilibrium MD simulations. A thiol protected Au NP is placed at the center of the box and solvated with water. Color code as in Figure 21, water is shown as gray-stick representation. Top-right: plot of the temperature profile for the different ligand types as a function of the distance from the NP COM, r. The light-red shaded area corresponds to the Au–ligand interface (AuL); the light blue one corresponds to the ligand–water interfaces (LW) after accounting all the study cases reported in the legend. The precise protocol to compute the interface is detailed in Section 4.4. Right-bottom: plot of the radial distribution function (RDF) of the water molecules as a function of r.

perature drop at the ligand–water interface (ΔT_{LW}, light-blue shaded area), in contrast, is smaller by an order of magnitude. For example, for the pMBA ligand (orange line) $\Delta T_{AuL} = 39.8 \pm 0.7$K $> \Delta T_{LW} = 2.1 \pm 0.4$ K. The hydrophobic MC11 ligand, instead, shows two almost equal temperature drops at the Au-ligand and ligand-water interfaces ($\Delta T_{AuL} = 31.6 \pm 0.4$ K and $\Delta T_{LW} = 24.3 \pm 0.3$ K), separated by a temperature plateau. The temperature drops for all ligands are also reported in Table 4. A similar behavior is also shown in the work of Hung *et al.* [167] for the temperature drops at the interface between a Au(111)-supported self assembled monolayer (SAM) and water: using a hydrophilic SAM they observe $\Delta T_{AuL} > \Delta T_{LW}$ and vice-versa for the hydrophobic case. To quantitatively rank the temperature profiles, we have defined the following dimensionless quantity:

$$R = \frac{\Delta T_{AuL}}{\Delta T_{AuL} + \Delta T_{LW}} \tag{4.1.1}$$

For the bare case, $R = 1$ since $\Delta T_{LW} = 0$. The lower the R value, the more the ligand acts as a thermal insulator, increasing ΔT_{LW} and lowering ΔT_{AuL}.

ALTERNATIVE SETUP We aim at verifying if the constrained cold-water molecules of our main setup could lead to perturbations such to produce unrealistic temperature profile, i.e. to verify that the resulting temperature profile around the Au NP does not depend on the choice of the non-equilibrium MD scheme. Thus, We have built an alternative setup to derive the temperature gradient from non-equilibrium

Ligand name	R	ΔT_{AuL} [K]	ΔT_{LW} [K]
MC11	0.565 ± 0.009	31.6 ± 0.4	24.3 ± 0.3
PEG7	0.89 ± 0.02	41.1 ± 0.8	5.3 ± 0.3
MMUA	0.89 ± 0.02	42.4 ± 0.8	5.0 ± 0.3
PEG3	0.91 ± 0.02	41.5 ± 0.7	4.1 ± 0.3
pMBA	0.95 ± 0.02	39.8 ± 0.7	2.1 ± 0.4
bare	1.00 ± 0.02	48.7 ± 0.7	–

Table 4: Values of the dimensionless parameter R (see Equation (4.1.1)) and the temperature drops at Au–ligand and ligand–water interfaces. The error on R was computed with the statistical error propagation theory.

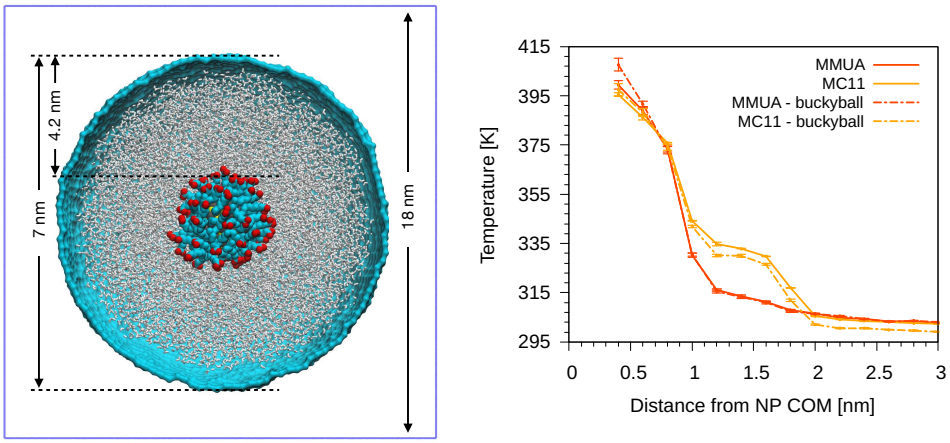

Figure 33: Left: System configuration of the alternative setup. Color code as in Figure 21. Right: Temperature profiles of MMUA and MC11 ligand types for both setups as a function of the distance from the NP COM.

MD simulations. The alternative system, shown in the left panel Figure 33, is made by a rigid spherical buckyball of 4894 atoms and diameter of ~ 7 nm. The atoms of the buckyball are parametrized like carbon atoms and its density is tuned in such a way that water molecules cannot pass through it. Then, a ligand protected Au NP is placed at the center of the buckyball and the system is solvated with about 39000 SPC/E water molecules. The number of water molecules has been chosen so as to achieve a water density of about 1000 kg/m^3. In Figure 34 it is show the number density of each system part as a function of the distance from the NP COM. For the non-equilibrium MD simulations the heat source is represented by the Au atoms thermostated at $T_{hot} = 380$ K and heat sink by the buckyball itself, whose atoms are thermostated at $T_{cold} = 280$ K. We performed the non-equilibrium MD simulations with the alternative system only for the MMUA and MC11 ligand types: these two ligands show two different temperature profiles while they only differ in the functional terminal group (a charged $-COO^-$ for the first ligand and a $-CH_3$ in the second one). A comparison of the temperature profile obtained with the two setups is shown in the right panel of Figure 33. As we can see, the temperature profiles obtained with the two setups are very similar.

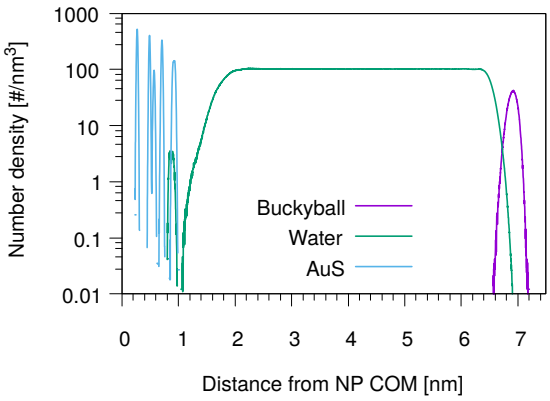

Figure 34: Number density of each system part (excluded the functionalizing ligands) of the alternative setup as a function of the distance from the NP COM.

4.2 DYNAMICS AND STRUCTURE OF INTERFACIAL WATER

Since hydrophobicity seems to be an important driving force shaping the temperature profile around the NP, we have investigated water penetration into the shell of the different ligand types. The bottom-right panel of Figure 32 shows the RDFs of the water molecules as a function of the distance from the NP COM. Despite the different chemico-physical nature of the ligands, there is no clear correlation between the water RDFs and the temperature profiles. For instance, the RDFs of water for MMUA and MC11 are quite similar while the temperature profiles differ significantly. This suggests that, if water molecules play a role in the heat transfer, this may not be related to the number of water molecules inside the ligand shell or at the ligand-water interface but rather to water dynamics or to the specific interaction between water molecules and the functionalizing ligands.

INTERFACIAL WATER We thus investigated if and how the thermal gradients are correlated to the mobility of interfacial water. We classify as interfacial water all water molecules having non-bonded interactions with the ligand atoms (Lennard-Jones and Coulomb energy terms) larger than the thermal energy of the fluid at interface: $\propto k_B T$ [168]. Figure 35 provides a graphical representation of the interfacial water molecules. If one imagines that a single-well effective potential describes the interaction between water and the NP surface, all water molecules that *i.* are located in the shell corresponding to the potential well and *ii.* have a kinetic energy can does not allow to escape the effective potential barrier, can be classified as interfacial water molecules.

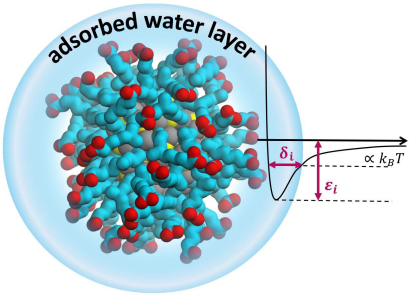

Figure 35: Schematic representation of interfacial water molecules. Color code as Figure 21

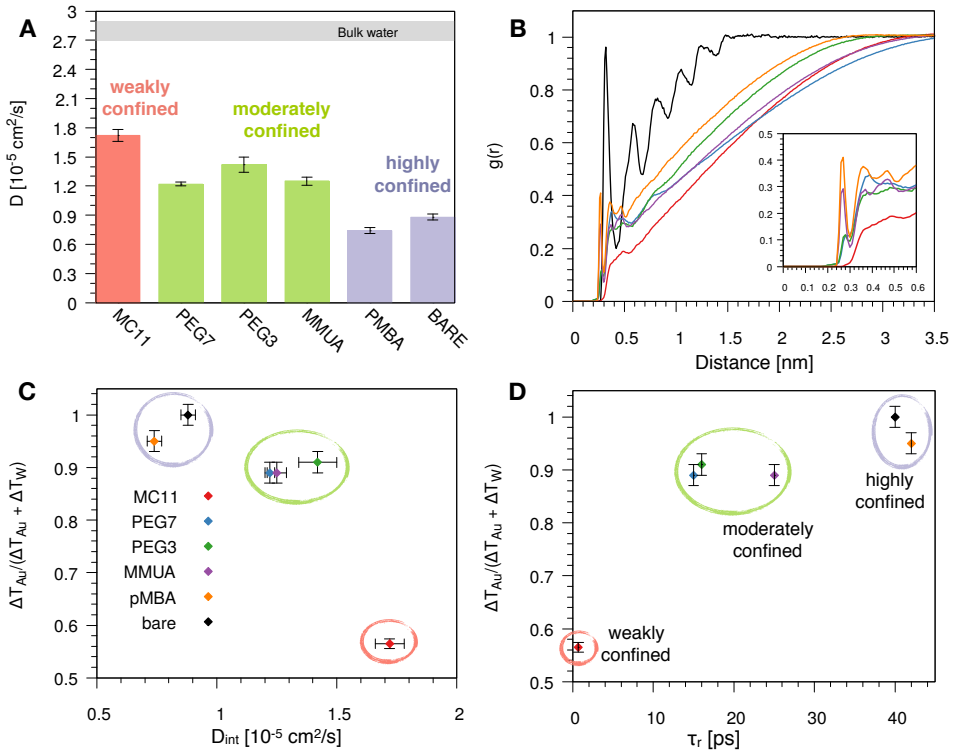

Figure 36: **A**: self-diffusion coefficient of the water molecules confined at the ligand–water interface, D_{int}, for the different ligand types. The grey area corresponds to the range of the self-diffusion coefficient of bulk water, far from the NP (D_{bulk}), obtained for the different ligands, compatible with the SPC/E self-diffusion coefficient [110]. **B**: radial distribution function, $g(r)$, of the water oxygens as a function of the distance between the oxygen and any atom of the Au NP and ligands. **C** and **D**: plot of the R parameter, see Equation (4.1.1), as a function of D_{int} (**C**) or as a function of the water characteristic residence time τ_r (**D**), at ligand–water interface. Colored bars and circles indicate the degree of water confinement: red for weakly confined water at the interface of hydrophobic MC11, green for moderately confined water in proximity of hydrophilic PEG7, PEG3 and MMUA and purple for highly confined water close to charged pMBA and bare Au NP.

WATER DYNAMICS From equilibrium MD simulations, we computed the self-diffusion coefficient of bulk water (that is, water far from the NP), D_{bulk}, and that of the interfacial water molecules, D_{int}. The results are shown in Figure 36 and also reported in Table 5. The diffusion coefficient for bulk water is compatible with the one obtained for the SPC/E water model [110]. The diffusion coefficient of water at the ligand–water interface is substantially reduced with respect to the bulk molecules, as also shown in [168] for water confined around a wide class of NPs. Most interestingly, the reduction of the diffusion coefficient depends on the functionalization of the Au NP: we recorded the lowest value of the diffusion coefficient for the pMBA ligand, $D_{int} = 0.74 \pm 0.03 \cdot 10^{-5}$ cm^2/s, and the highest $D_{int} = 1.72 \pm 0.06 \cdot 10^{-5}$ cm^2/s is found in presence of the hydrophobic MC11 ligand type. D_{int} visibly clusters into three groups identified as weakly, moderately and highly confined water corresponding to the transition from hydrophobic to

Ligand name	R	$D_{int}[10^{-5}\ cm^2/s]$	$D_{bulk}[10^{-5}\ cm^2/s]$	τ_r [ps]
MC11	0.565 ± 0.009	1.72 ± 0.06	2.9 ± 0.2	0.7
PEG7	0.89 ± 0.02	1.22 ± 0.02	2.72 ± 0.05	15
MMUA	0.89 ± 0.02	1.25 ± 0.04	2.70 ± 0.03	25
PEG3	0.91 ± 0.02	1.42 ± 0.08	2.81 ± 0.03	16
pMBA	0.95 ± 0.02	0.74 ± 0.03	2.93 ± 0.06	42
bare	1.00 ± 0.02	0.88 ± 0.03	2.92 ± 0.06	40

Table 5: Value of the R parameter (see Equation (4.1.1)), the water self-diffusion coefficient at ligand–water interface (D_{int}) and in the bulk (D_{bulk}) and of the water characteristic residence time (τ_r) for each type of ligand. The error on D was computed as the standard deviation of the self-diffusion coefficient obtained from independent simulations.

hydrophilic ligands and eventually to the bare Au surface (panel A and C of Figure 36). We also quantified the characteristic residence time, τ_r, of interfacial water around the different types of ligands, τ_r (panel D of Figure 36). The residence time depends on the functionalization of the Au NP: the lowest value is recorded for the MC11 ($\tau_r = 0.7$ ps) and the largest for the pMBA ($\tau_r = 42$ ps). To further characterize the water structuring and density at interface we calculated the RDF of the water oxygens as a function of the distance between the oxygen and any atom of the Au NP and ligands. As confirmed by Figure 36D, the MC11 coated Au NP shows, at ligand–water interface, the lowest density and oxygen structuring that is not present when the ligand is hydrophilic.

Figure 36 distinctly emphasizes that a large water mobility at hydrophobic ligand interface prevents the heat release at the ligand–water interface. Hydrophobic ligands are thus acting as a thermal insulator. On the other hand, the more confined water state registered around the hydrophilic ligands is the promoter of a more efficient thermal transport across the interface (highest R).

VIBRATIONAL DENSITY OF STATES Based on the acoustic and diffusive mismatch models of the thermal conductance at solid–solid interfaces, several studies have related interfacial temperature drops to the overlap of the vibrational spectra [169], even for solid–liquid and liquid–liquid interfaces. For example, the overlap of the vibrational density of states (vDOS) between Au NPs and rigid or flexible water models has been invoked to explain a little difference in the thermal conductance at the Au–water interface [170]. Similar considerations hold for three-component interfaces. Gezelter and collaborators have found positive correlation between the overlap of the vibrational power spectra of the interface components and the thermal conductance, in different systems including Au surface/butanethiol/organic solvent [171], CdSe surface/hexylamine/hexane,[42] Au NP/alkane(or alkene)thiols/hexane [165]. Organic ligands with long saturated carbon tails are expected to have a good vibrational overlap with organic alkane

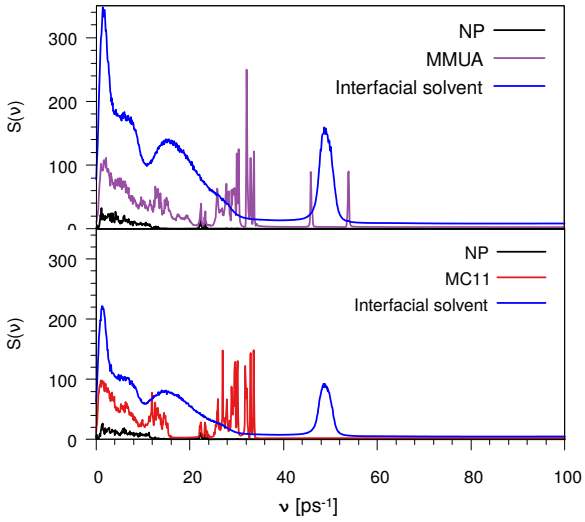

Figure 37: Plot of the vDOS for the core atoms (black lines), ligand atoms (red and purple lines) and the water molecules at interface (blue lines) for the MC11 (top panel) and MMUA (bottom panel) NPs. The two spectra for the interfacial solvent have the same shape but different normalization because of the different number of water molecules at interfaces: less for the MC11 than that for the MMUA.

solvents [161]. However, relating the temperature drops at solid-liquid and liquid-liquid interfaces with the spectra overlapping between the involved materials is not always straightforward, and often only qualitative trends can be derived from this kind of analysis [161]. No correlation between spectral overlap and thermal conductance was found by Alexeev *et al.* for graphene-water interfaces [162]. For thiolated Au surfaces in water, Hung *et al.* found lower thermal conductance for hydrophobic SAMs than for hydrophilic, OH-terminated SAMs, but no correlation with the overlap between their vibrational spectra and that of water [167]. Here, we calculated the vDOS of the different materials composing the interface (Au and S atoms, ligand atoms and water molecules at ligand–water interface), for the MC11 and MMUA cases, as better detailed in Section 4.3. We found, as shown in Figure 37, that there is no appreciable difference between the overlap of solvent and ligand vDOS in the MC11 and MMUA cases, despite the temperature profiles are quite different.

Here, we have unveiled the role of water dynamics on the thermal conductance at the three-component Au NP–ligand–water interface. In particular, we have investigated via MD simulations the interfacial water physics driving the thermal transport from a ligand coated Au NP with an average temperature of 380 K to a water bath at 300 K. For bare and hydrophilic ligand-coated NPs, the temperature profile exhibits a single steep descent at the Au–ligand interface. Instead, a different temperature profile is found in the case of fully hydrophobic ligands coating the hot Au NP. We observe a first temperature drop at the Au–ligand interface, a temperature plateau, and a second large drop of $\sim$ 40 K at the ligand–water interface. We thus interpret the data based on the dynamics of water at the ligand–water interface. The large water mobility registered only in the case of completely hydrophobic ligands prevents interfacial water from exchanging heat with the hot NP, thereby increasing the thermal resistance at the ligand–water interface and causing a significant heating of the ligand shell. On the contrary, water is more effectively confined (low water mobility) at the interface with hydrophilic ligands,

promoting NP-to-solvent heat transfer and reducing the thermal resistance at the ligand–water interface. This mechanism, which we have described for the case of thiolated Au NPs, can also explain the dependence of thermal conductance on the hydrophobicity of the SAMs adsorbed at different planar interfaces [158].

4.3 PREDICTIVE METHODOLOGY

The temperature profiles shown so far rely on the direct calculation of the time-averaged temperature, which in turn requires MD simulations with extensive sampling of both positions and velocities. Indeed, performing the MD simulations for the derivation of the temperature profiles it is the most time-consuming part of this work and it can request up to a week for each profile. Thus, beyond the physical insight of the conductance at the three-component Au NP–ligand–water interface, it is of interest to propose a more efficient and less time-consuming predictive methology that, based on short inexpensive equilibrium MD simulations, is able to predict which functionalization would be more efficient at creating a spatially confined hot region around the NP.

For this purpose, as proposed by Chiavazzo *et al.* [168], we tested whether the different behavior of interfacial water could be related to the strength and spatial extent of the ligand–water interaction. Indeed, these energy and structural data are accessible via equilibrium MD simulations without recurring to non-equilibrium setups and to the extensive sampling required so far. We characterized the water confinement around a NP by means of a spatial and an energetic parameter, δ and ϵ. Figure 35 provides a graphical explanation of the physical meaning of δ and ϵ. Their definition relies on the identification of a single-well effective potential interaction between water and the NP surface. In detail, the characteristic length of the water nanolayer δ can be explained as a measurement of the thickness of the layer in which the non-bonded interaction energy between water and the ligands is larger than thermal energy ($\propto k_B T$), thus causing the typically reduced solvent mobility at the interface [168, 172]. The water confinement energy ϵ instead represents the binding energy of the effective potential between interfacial water and the NP (core and ligands). We have then computed these two parameters for all the considered Au NPs, as reported in Figure 38 and in Table 6.

The water confinement energy ϵ, which is expressed in kJ/mol, is divided by the thermal energy associated to the temperature at the ligand–water interface, in order to obtain a dimensionless parameter, the normalized-$\epsilon = \epsilon/(k_B T_{LW} N_A)$. In Figure 38 the parameter R (see Equation (4.1.1)) is plotted as a function of normalized-ϵ (left panel); and as a function of the characteristic water confinement length, δ (right panel). The normalized-ϵ and δ parameters are distributed in three main regions. For $R < 0.8$ we only find the MC11 ligand that is characterized by the smallest R and the feeblest interaction with water (normalized-$\epsilon = -1.48 \pm 0.06$ and $\delta = 0.34 \pm 0.01$ nm). All the hydrophilic ligands (PEG7, MMUA, PEG3 and pMBA), instead, show similar values of the normalized-ϵ and δ (see Table 6). Finally, for $R = 1$ we have the bare Au NP with the strongest interaction with

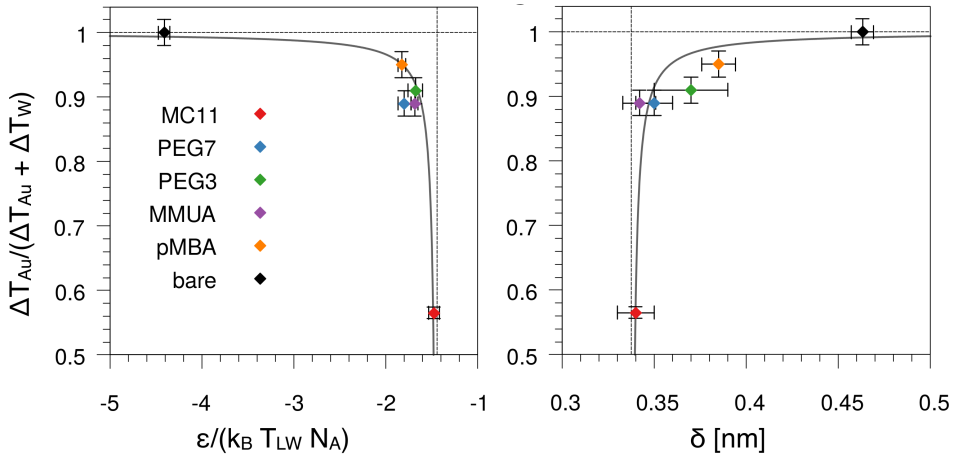

Figure 38: Left: Dimensionless parameter R (see Equation (4.1.1)) as a function of the parameter ϵ normalized with respect to the thermal energy associated to the temperature at ligand–water interface. Right: Plot of the same parameter R as a function of the characteristic water confinement length, δ.

Ligand name	R	δ [nm]	ϵ [kJ/mol]	$\epsilon/(k_B T_{LW} N_A)$
MC11	0.565 ± 0.009	0.34 ± 0.01	-3.7 ± 0.1	-1.48 ± 0.06
PEG7	0.89 ± 0.02	0.35 ± 0.01	-4.6 ± 0.2	-1.80 ± 0.07
MMUA	0.89 ± 0.02	0.342 ± 0.009	-4.3 ± 0.1	-1.69 ± 0.04
PEG3	0.91 ± 0.02	0.37 ± 0.02	-4.3 ± 0.2	-1.68 ± 0.08
pMBA	0.95 ± 0.02	0.385 ± 0.009	-4.7 ± 0.1	-1.83 ± 0.04
bare	1.00 ± 0.02	0.463 ± 0.006	-12.0 ± 0.2	-4.41 ± 0.06

Table 6: Values of the dimensionless parameter R (see Equation (4.1.1)), the characteristic water confinement length (δ), energy (ϵ) and the normalized–ϵ.

water (normalized-$\epsilon = -4.41 \pm 0.06$) and the largest $\delta = 0.463 \pm 0.006$ nm. We thus observe that ligands with a feebler interaction with water lead to the formation of a thick hot layer around the NP, which is further evidence of a poor heat conduction on the solvent side. The R data *vs.* normalized-ϵ and δ are well fitted by a hyperbolic function (solid grey line in the plots of Figure 38, fitting parameters in Table 7), of the form

$$R(x) = \frac{b + x}{x - a}$$

where x is ϵ or δ and the asymptote parallel to the x-axis is fixed to 1. The fitting was done first linearizing the data, then fitting with the least square method the linearized inverse function $h(R) = x(R-1) = aR + b$, where x is $\epsilon(R)$ or $\delta(R)$, to obtain the parameter a and b, reported in Table 7.

Our results suggest that short equilibrium MD simulations could be used to screen a large set of ligands with different degrees of hydrophobicity. The *in silico* estimate of their ϵ and δ parameters could allow for the prediction of the temperature gradients arising at the NP–ligands and ligands–solvent interfaces.

	a	b
normalized$-\epsilon$	-1.44 ± 0.05	1.46 ± 0.04
δ	-0.339 ± 0.004 nm	0.337 ± 0.005 nm

Table 7: Values of the fitting parameters a and b for normalized-ϵ and δ.

Finally, beyond the physical insight, our results can contribute to the engineering of coated NPs with controlled thermal behavior in presence of intense, short laser pulses [154]. The proposed computational approach could indeed be used to predict which functionalization would be more efficient at creating a spatially confined hot region around the NP. As this approach is based on the use of short equilibrium MD runs, it could be easily exported to the case of larger NPs, coated by more massive organic ligands [155]. These results, together with the knowledge of the NP absorbance, could finally allow the estimation of the temperature rise occurring in those biological components in direct contact with theranostic Au NPs, such as the lipids and the plasma membrane proteins in photoporation applications.

4.4 PARAMETERS AND METHODS

System Setup

In all non-equilibrium simulations, the Au NP was restrained at the center of the box by applying a position restraint at one of the most internal Au atom with an elastic constant of 5000 kJ/(mol nm) in the three directions. The heat sink corresponds to a group of 500 water molecules, that are constrained to move outside a sphere of radius 6 nm centered at the center of the box. The applied constraint is a spherical flat-bottom position restraint with an elastic constant of 1000 kJ(mol nm). Each water molecule in this group is subject to a harmonic repulsive potential only if its distance from the NP COM is less than 6 nm, otherwise it moves unperturbed. The constrained water molecules do not affect the dynamics nor the structural properties of water, as we see in the water RDFs shown in Figure 39.

Simulation parameters

All non-equilibrium simulations were performed with a time step of 2 fs. The pressure was kept constant at 1 bar with Parrinello-Rahman barostat ($\tau_P = 0.1$ ps). The temperature of the two thermostated regions were kept constant with two Noose-Hoover thermostats. All non-equilibrium simulations were pre-equilibrated with the same parameters for 5 ns. Then, 80 ns long production runs, for each NP, were performed and used to calculate the temperature profiles.

All equilibrium MD simulations to calculate water properties were performed in the NPT_{NP} ensemble with a time step of 1 fs and a *verlet-buffer-tolerance* of 0.0001 kJ/(mol ps). These simulations were pre-equilibrated in the NPT ensemble

with a time step of 2 fs, Berendsen barostat and v-rescale thermostat to maintain constant, respectively, pressure (1 bar) and temperature of the system (300 K). Then, the barostat was switched to Parrinello–Rahman ($\tau_P = 0.1$ ps) and the v-rescale thermostat ($\tau_T = 0.2$ ps), with a reference temperature of 300 K, was applied only on the NP atoms while the rest of the system was left un-thermostated, in order not to affect the properties of water at the interface. In this case two independent 5 ns runs were performed for each NP.

The alternative non-equilibrium MD simulations are performed in the NVT ensemble with a time step of 2 fs. The system is pre-equilibrated for 15 ns with v-rescale thermostat ($T = 300$ K and $\tau_T = 1$ ps) applied separately at Au NP, solvent and buckyball atoms. Then, 65 ns long MD simulation was performed with Noose-Hoover thermostat ($\tau_T = 1$ ps), applied at Au atoms ($T_{hot} = 380$ K) and at buckyball atoms ($T_{cold} = 280$ K). The temperature profile was obtained discharging the first 15 ns of the trajectory, in order to have the system with the correct temperature gradient.

Temperature profiles

The temperature profiles in function of the distance from the NP center of mass, were calculated with an in house Gromacs tool, freely downloadable from our online repository [173]. To calculate the local temperature, the system was divided in spherical shells of fixed thickness ($\Delta R = 0.2$ nm) and the kinetic energy (K_i) for the i shell was calculated according to the equipartition theorem as $T_i = N_i^{DOF} K_i / 2$. N_i^{DOF} is the total number of DOF in the ith shell, taking appropriately into account the presence of constrained bonds. In order to obtain a smooth temperature profile each profile is obtained by averaging, along the 80 ns trajectory, the temperature profiles collected every 2 ns. This time interval was chosen in such a way as to average independent temperature profiles, coherently with the longest decorrelation time of the temperature of a given shell, as we have calculated with the error estimation option of the *gmx analyze* tool. The error on temperature was computed as the standard error associated to the mean.

The temperature drop at the sharp Au–ligand interface (ΔT_{AuL}) was calculated as $\Delta T_{AuL} = T(R = 1\text{ nm}) - T(R = 0.8\text{ nm})$. The ligand–water interface, instead, is not sharp, and we have thus defined ΔT_{LW} as the temperature drop in a space interval between 75% and 95% of the area of the RDF of the ligand.

Self-diffusion coefficient

The self-diffusion coefficient of water at the ligand–water interface, D_{int}, was calculated with a homemade Gromacs tool, freely downloadable from our online repository [173]. The input trajectory, with 1 frame every 5 ps, was divided into stretches of 150 ps. For each stretch, the mean square displacement (MSD) was calculated only for the water molecules that were in contact (within a cut-off equal to the value of δ)) with at least one atom of the NP+ligands system in the first

frame of that stretch. Then, the MSD was averaged between all stretches and the self-diffusion was calculated with the Einstein relationship:

$$\mathrm{MSD} = \lim_{t \to +\infty} \left\langle \|r_i(t) - r_i(0)\|^2 \right\rangle = 6Dt$$

Characteristic residence time

The water characteristic residence time, τ_r, is calculated with a homemade Gromacs tool, available in our online repository [173]. For each frame of the trajectory, a shell of thickness δ around each atom of the NP is defined. Each water molecule for each frame is tracked to record the time, τ, for which the water molecule is continuously inside the shell, i.e. continuously in contact with an atom of the NP. A frequency histogram $P(\tau)$ is built. The characteristic residence time, τ_r, is defined as [174, 175]:

$$\tau_r = \frac{\int_0^{+\infty} \tau P(\tau)\ d\tau}{\int_0^{+\infty} P(\tau)\ d\tau}$$

Vibrational density of states

The vDOS as a function of the frequency, $S(\nu)$, are calculated through the double precision version of the Gromacs *gmx dos* tool [176], in which the vDOS spectrum is calculated by the Fourier transform of the mass-weighted velocity autocorrelation function [177]. $S(\nu)$ is defined such that its integral over ν is the total DOF [177]. To compute the vDOS a 20 ps long trajectory with a saving frequency of 1 fs is used (for both positions and velocities). This simulation has been performed in double precision and in the microcanonical ensemble (NVE) using the velocity Verlet integrator with a time step of 0.1 fs and a cut-off for the short-range neighbor list of 1.3 nm (to ensure a better energy conservation).

Error estimation on ϵ and δ

The error estimation to ϵ and δ was derived following the statistical error propagation theory. Following the work of Chiavazzo and collaborator [168], ϵ and δ are defined by the following equations:

$$\epsilon = \frac{1}{S}\left(\sum_i \epsilon_i s_i\right) = \frac{\sum_i \epsilon_i s_i}{\sum_i s_i}; \qquad \delta = \frac{\sum_i \delta_i s_i}{\sum_i s_i}$$

Where S is the total solvent accessible surface area (SASA) defined as:

$$S = \sum_i s_i; \qquad \sigma_S^2 = \sum_i \sigma_{s_i}^2$$

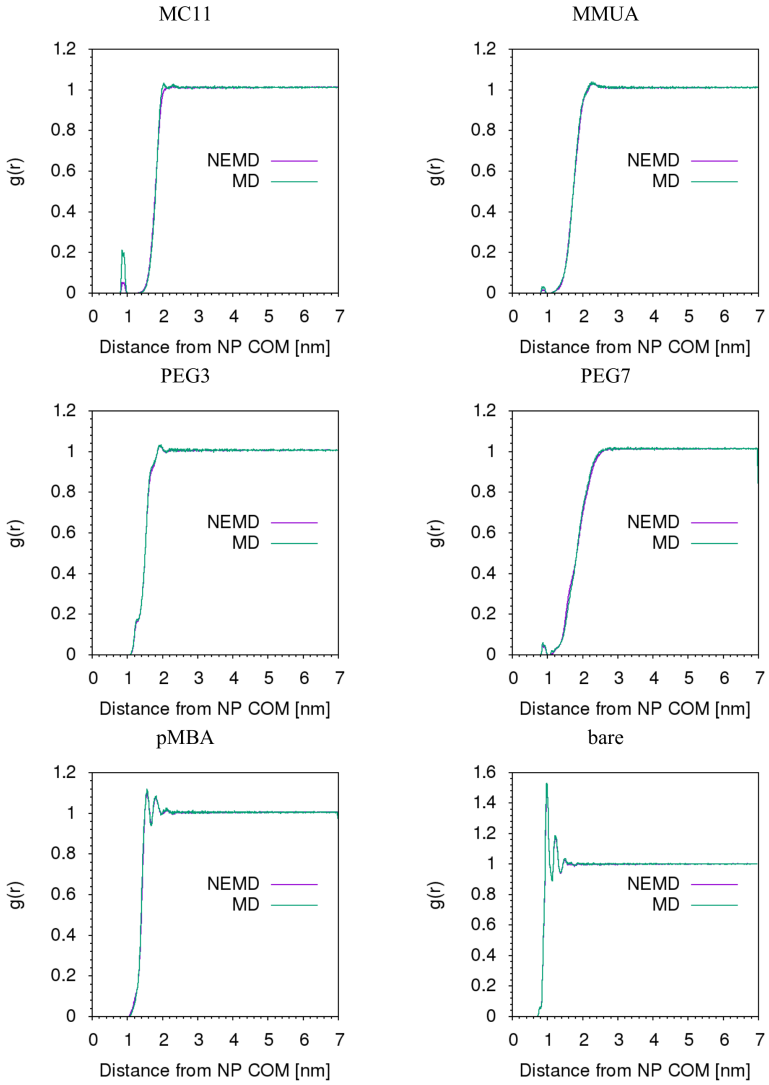

Figure 39: Plot of the water RDF in a comparison between equilibrium and non-equilibrium MD simulations, for each type of NP.

and s_i is the SASA for the ith atom of the NP. Then, the error propagation of ϵ reads as:

$$\sigma_\epsilon^2 = \epsilon^2 \left(\frac{1}{S^2} \sum_i \sigma_{s_i}^2 + \frac{\sum_i \epsilon_i^2 \sigma_{s_i}^2}{(\sum_i \epsilon_i s_i)^2} \right) = \frac{1}{S^2} \left(\epsilon^2 \sum_i \sigma_{s_i}^2 + \sum_i \epsilon_i^2 \sigma_{s_i}^2 \right)$$

In the same way for δ, we have:

$$\sigma_\delta^2 = \frac{1}{S^2} \left(\delta^2 \sum_i \sigma_{s_i}^2 + \sum_i \delta_i^2 \sigma_{s_i}^2 \right)$$

5 EFFECT OF CHARGE AT NP – MEMBRANE INTERFACE

In this chapter we study the interaction of anionic ligand–protected Au NPs with a model cell membrane. Plasma membranes are indeed the target for many applications of Au NPs in the biomedical field, such as controlled drug delivery, diagnostic or therapeutic devices, photothermal therapy and imaging. Cell membranes are the first barrier that NPs encounter when they successfully reach the target cells. To penetrate cell membranes, NPs follow different routes which depend on the nature of the functionalizing ligands, shape or size. From a physicochemical perspective, the NP–membrane interaction results from the complex interplay of electrostatics, hydrophobic interactions, ligand composition, surface ligand organization and, on the membrane side, lipid composition and phase. Small (< 10 nm) ligand–protected Au NPs, such as those treated in this thesis, can passively translocate both model and real cell membranes as shown by experimental data [47, 53, 145]. We thus use computer simulations, at atomistic and CG level, to elucidate by which molecular mechanisms these NPs can spontaneously interact with a model membrane. We found that the MUA:OT Au NP can passively penetrate into a flat POPC model membrane *via* a three–stage mechanism, deforming and perturbing the membrane itself [123, 124]. Moreover, we show that the protonation of the MUA ligand, which we prove to be likely when the NP is in contact with the lipid membrane, can affect the mechanism of NP–membrane interaction, making it faster and less disruptive [126].

5.1 NANOPARTICLE – MEMBRANE INTERACTION

Recently, the literature concerning the computational modeling about the interaction of anionic monolayer–protected Au NP and model lipid membranes has expanded contributing to sketch a possible mechanism of such interaction [146, 147, 178, 179]. The first step of the interaction between the NP, dissolved in the extracellular water environment, and the membrane is the attraction between the charged ligands and the polar head of the zwitterionic phospholipids: electrostatics is recognized to be the driving force for the adhesion of the Au NP to the membrane surface, Figure 40a. To the other end of the pathway, it is predicted, on thermodynamic basis [47], that the most stable state for the Au NP corresponds to the so-called *snorkeling* configuration in which the NP is embedded in the hydrophobic region of the membrane, while the charged ligands stably interact with the lipid heads of both leaflets, Figure 40d. However, the penetration of anionic Au NPs in lipid bilayers is still debated. Recently, Tatur and coworkers [145], by means of a neutron reflectometry experiment on a floating zwitterionic lipid bilayer,

found that anionic Au NPs can only adhere to the surface of the lipid membrane, whitout penetrating it. On the contrary, the experiments with dye-labelled NPs and multilamellar vesicles performed by Van Lehn *et al.* [47] showed that anionic MUS:OT Au NPs can adhere on the lipid membrane and passively diffuse, without membrane disruptions, towards the inner bilayers of the multilamellar vesicles (see Figure 6). The same passive penetration mechanism was found also by Goodman *et al.* [53] and Sabella *et al.* [52] *via* experiments on cells. On the computational side, Heikkilä and collaborators [178], demonstrated, by atomistic MD simulations, that anionic MUA:OT Au NPs can adsorb at the surface of neutral lipid membranes. The limited time scale of the simulations performed in their work did not allow to observe and describe any penetration of the NP into the hydrophobic membrane core. However, later on, Van Lehn *et al.* have considered the interaction between an anionic MUS:OT Au NP with a highly curved lipid bilayer [146] and a with a flat defect–free bilayer [147, 179], observing, *via* biased atomistic MD simulations, the fusion between the NP and the membrane. The internalization pathway was rationalized at CG resolution and with unbiased MD simulations by Simonelli *et al.* [123], with an anionic MUA:OT Au NP interacting with a model POPC bilayer.

Another aspect to be considered in the NP–membrane interaction, is the role played by the ligand arrangements on the NP surface, which is still not completely clear. Verma *et al.* [51] showed that NPs differing in ligand pattern were internalised into cells via different routes and, in particular, NPs with a large patches could spontaneously penetrate the cell membrane. From thermodynamic considerations [47], however, no substantial difference in the free energy of translocation of NPs with small or large patches was found. Anther computational study by Gkeka and collaborators [180], who used an explicit model of water and lipid membrane to compute the free energy of transfer of NPs with different surface arrangements, demonstrated that homogeneous NPs are more easily internalised than NPs with small patches.

5.1.1 Three-stage mechanism of NP – membrane interaction

Simonelli and collaborators [123] derived via unbiased CG MD simulations, the molecular mechanism associated to the interaction between a MUA:OT NP and a flat defect–free model biological membrane. Furthermore they found that the NP–membrane interaction depends on the surface arrangements of the NP ligands. Here I will briefly describe the conclusions achieved in [123], as these results are the basis on which this thesis work was developed.

The internalization mechanism that regulates the insertion of the Au NP into the core of a planar membrane is a three–stage mechanism, see Figure 40. When the NP in the water phase is approaching the surface of the membrane it enters in the stage 1, the adsorbed state, in which the charged ligands interact with the polar lipid heads. The stage 2 is the hydrophobic contact, Figure 40b, in which the hydrophobic beads of the MUA and OT ligands are in contact with the hydrophobic tails of the membrane while the charged bead of the MUA ligands are still in the water

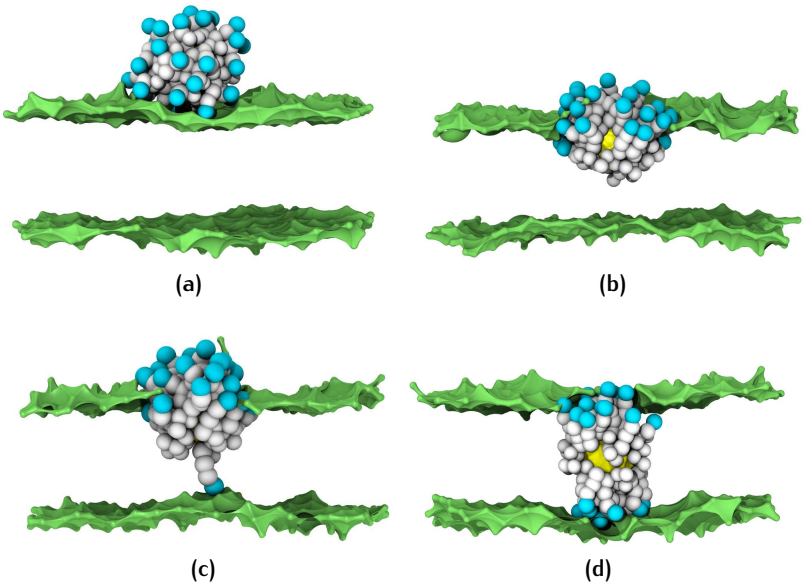

Figure 40: Au NP–membrane interaction. (a) stage 1, adsorption of the NP at membrane surface; (b) stage 2, the protrusion of a lipid tail initiates the hydrophobic contact that leads to partial embedding of the NP in the membrane core; (c) the NP binds to the opposite leaflet throwing a charged ligand; (d), stage 3, snorkeling configuration (five anchors shown). The hydrophobic beads of the ligands are shown in white and the charged beads in cyan. Lipid heads are green; lipid tails and water beads not shown for clarity. Adapted from [123].

phase or in contact with the lipid heads. The stage 3 is the snorkeling configuration, Figure 40d.

A key role for the stage 1 to stage 2 transition is played by a lipid tail protrusion out of the hydrophobic region that stably interacts with the hydrophobic beads of the NP ligands. The protruding lipid pulls the OT ligands into the membrane core and the NP enter the hydrophobic state, Figure 40b. This process, which we see through unbiased simulations, is the same mechanism observed by Van Lehn *et al.* [146, 147, 179] with biased atomistic simulations. The NP is then pulled towards the center of the bilayer and, subsequently, due to thermal fluctuations a charged ligand can cross the membrane core and stably interact with the head region of the opposite leaflet bringing the NP in the anchored state, Figure 40c. According to the standard MARTINI model, the anchored state is thermodynamically favorable with respect to the hydrophobic state. Indeed, in the unbiased MD simulations performed by Simonelli *et al.*, after the first anchor had been dropped, more and more ligands would anchor to the head region of the opposite leaflet, approaching step–by–step the snorkeling configuration, Figure 40d, as also predicted by Van Lehn *et al.* using thermodynamic models [47].

Eventually, and consistently with previous thermodynamics–based models [47], Simonelli *et al.* found that the energy cost associated with the extraction of the NP out of the membrane core is very high, making the anchoring process, and the snorkeling configuration, almost irreversible. We want to stress out that all the aforementioned transitions are triggered by rare events: the lipid tail protrusion

and the membrane translocation of a charged bead. Hence they could be observed to happen spontaneously only thanks to the use of a CG FF. Coherently with the picture emerging from computer simulations, the timescale of the interaction between these NPs and model lipid membranes is of the order of hours [61].

Simonelli *et al.* performed MD simulations for three different NP configurations: the (MUA:OT 1:1) with large patches and the (MUA:OT 1:1) and (2:1) with small patches. They found that the described behavior is common to the three configurations. Nevertheless, after the hydrophobic contact is reached its lifetime depends on the surface ligand arrangement. For NPs with small patches the time lag between the hydrophobic contact and the first anchor is on the order of few nanoseconds. Instead, NPs with large patches can linger in stage 2 for several microseconds. This suggests that the energy barrier to be overcome to move from stage 2 to the anchored state is lower for NPs with small patches.

5.1.2 Atomistic *vs.* coarse grained models

The NP–membrane interaction is driven by two main physical causes: *i.* the hydrophobic effect, that favours the hydrophobic contact between the NP and the membrane, and *ii.* the electrostatic interaction, that favours the contact between the anionic NP ligands and the neutral, but polar, head of lipid molecules. The results summarized in the last section are obtained using the standard MARTINI FF, with a cut-off method for treating the electrostatic interactions. As we have seen in Chapter 2, the cut-off method poorly describes the electrostatic interactions, especially in processes that involve the transfer of charged moieties from a polar to a non-polar environment. For example, it is known that the MARTINI FF can severely underestimate the height of the free energy barrier for membrane translocation of monovalent ions [119, 181]. A key step in the NP–membrane interaction involves the translocation of a charged bead (the terminal bead of the MUA ligand) from the polar water phase to the hydrophobic tail region of the membrane and further down to the distal leaflet headgroups. Thus, we want to test the reliability of the different MARTINI FFs in reproducing the anchoring transition. This section aims to point out, between the different CG MARTINI FFs, which is the one that allows for the best compromise between computational efficiency and reliability.

To this aim, we use both unbiased and metadynamics simulations at the atomistic level[1] to study the translocation process, and then used the atomistic results as a target for the comparison of three versions of the MARTINI FF:

i. the MARTINI FF with cut-offed electrostatics (SM) [99];

ii. the MARTINI FF with long range electrostatics (MPME) [99, 182];

iii. the MARTINI FF with long range electrostatics and water polarizability (MPW) [119];

The translocation process we want to analyze consists in the anchoring and disanchoring transition. The anchoring or forward process is the translocation of

1 All the atomistic simulations discussed in this chapter were performed by Federica Simonelli.

one charged ligand across the membrane (from the hydrophobic contact state to the anchored state); the disanchoring or backward process is, instead, the transition of the same ligand back to the starting configuration.

SIMULATION SETUP All biased and unbiased MD simulations at CG resolutions are performed with a model POPC membrane made of 512 lipids (about 13.2 × 13.2 nm^2). The NP we considered, if not specifically indicated, is the MUA:OT 1:1 NP with large patches placed in the hydrophobic contact state, which is the starting point of the anchoring transition we want to study. The NP with large patches is used, instead, because with the SM unbiased simulations showed the highest stability in the hydrophobic contact state. The resulting simulation box is solvated by about 15300 MARTINI water beads with Na^+ counter ions and 150 mM physiological salt solution. An example of the starting configuration is shown in Figure 41.

For what concerns the atomistic simulations (both biased and unbiased) the lipid membrane is made of 480 POPC lipids (about 13 × 13 nm^2) and the same NP in the hydrophobic contact state is used. The simulation box is solvated by about 32000 water molecules with Na^+ counter ions and 150 mM physiological salt solution.

The CV used for metadynamics simulations, d_z, as shown in Figure 41, is the z component of the distance between the bilayer COM and one of the charged terminal bead, which is the biased bead. We have chosen the ligand to be biased as the one whose charged terminal bead had the lowest z coordinate in the initial configuration. The total simulated time to obtain the potential of mean force (PMF) profiles is about 6, 7 and 31 μs for the SM, MPME and MPW model, respectively.

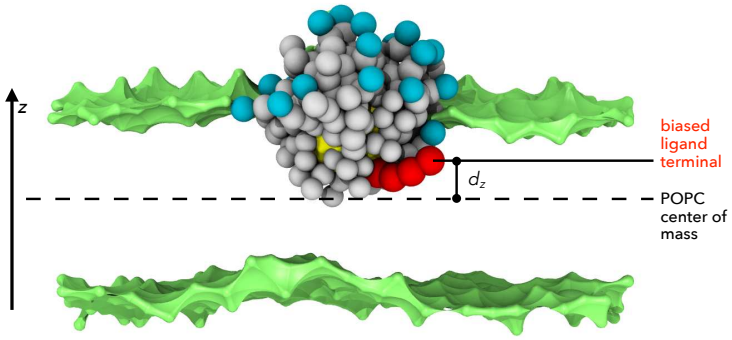

Figure 41: Initial configuration of metadynamics simulations: the NP is in the hydrophobic contact state. The reaction coordinate of metadynamics, d_z, is the distance along the z axis between the COM of the biased ligand (violet) and the COM of the bilayer. The NP core is shown in yellow, hydrophobic ligands in cyan, anionic ligands in magenta. For clarity, only the lipid heads of the membrane are shown as gray beads. Adapted from [124].

THERMODYNAMICS OF LIGAND TRANSLOCATION Contrary to the SM simulations, atomistic, MPME and MPW simulations did not show any spontaneous anchoring process during the unbiased simulations, which covered time scales of tens of microseconds. Thus we needed to use biased metadynamics simulations in order to obtain the anchoring transition. Eventually, we computed the PMF profiles

for the anchoring and disanchoring transitions, as shown in Figure 42. Each PMF profile is computed by averaging the profile of ten metadynamics runs, each biasing a differently charged ligand. Then, errors are estimated considering the standard deviation. The forward barrier, according to our reference atomistic runs,

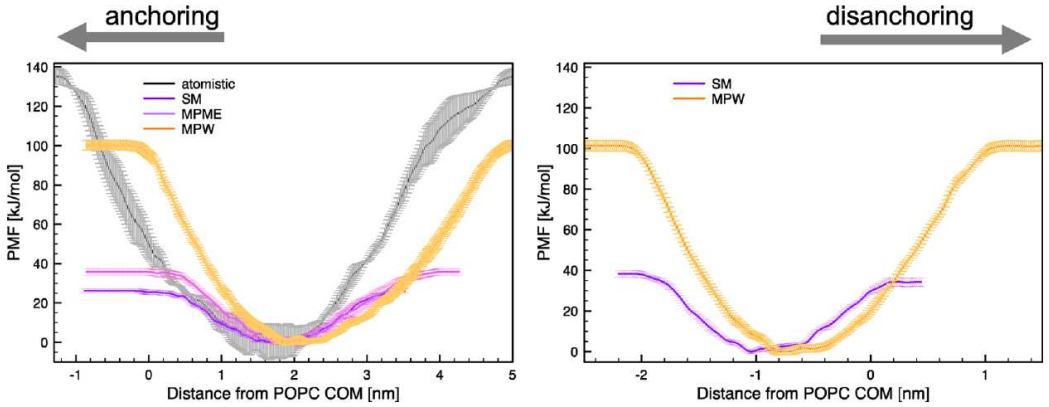

Figure 42: Potential of mean force profiles of the forward anchoring process (left) and of the backward disanchoring process (right). Distances are scaled to take into account the different membrane thickness in different models. Taken from [124].

is extremely large: 135 ± 10 kJ/mol. The SM severely underestimates the free energy barrier for the forward process, 26 ± 3 kJ/mol. The addition of long-range electrostatics does not improve much the comparison with the atomistic model, raising the barriers up to 36 ± 5 kJ/mol. The MPW model, instead, provides a barrier of 96 ± 2 kJ/ mol, much more in line with the atomistic result. We compared the backward barriers, as predicted by the SM and MPW models as well. According to the SM model, the backward process is disfavored with respect to the forward one, with a barrier of 38 ± 5 kJ/mol. The MPW model, instead, predicts a backward barrier of 101 ± 3 kJ/mol, thus attributing no thermodynamic advantages to any of the two states. The free energy barriers are summarized in Table 8.

(kJ/mol)	SM	MPME	MPW	atomistic
forward	26 ± 3	36 ± 5	96 ± 2	135 ± 10
backward	38 ± 5	–	101 ± 3	–

Table 8: Free energy barriers for the anchoring (forward) and disanchoring (backward) transition related to a MUA:OT (1:1) NP with large patches. Data from [124].

LIGAND TRANSLOCATION IS ACCOMPANIED BY DRAGGING OF LIPID HEADS AND WATER TOWARDS THE CENTRE OF THE MEMBRANE In the previous paragraph we have characterized the anchoring and disanchoring process from a thermodynamic point of view. In the following we will instead focus on the molecular processes that occur during the transitions. To this aim, we analyzed both biased and unbiased MD trajectories. We remark that the unbiased MD simulations we have performed with the atomistic, MPE and MPW models concern the NP in the hydrophobic

state only. Indeed, the high energy barriers that need to be overcome to get to the anchored state make the spontaneous anchoring process too slow to be observed on the microsecond time scale. Unbiased MD simulations are nevertheless useful to characterize the hydrophobic state in absence of any biasing potential. In the hydrophobic contact state, the NP partially penetrates the membrane. In Table 9

(nm)	SM	MPME	MPW	atomistic
$d^z_{COM\text{-}COM}$	1.708 ± 0.002	1.554 ± 0.005	1.717 ± 0.002	1.708 ± 0.008

Table 9: Average distance between the COM of the NP and the COM of the bilayer in the hydrophobic contacts state. Distances are scaled to take into account the different membrane thickness in different models. Data from [124].

we report the z component of the distance between the COM of the NP and the COM of the membrane, $d^z_{COM\text{-}COM}$, as calculated with the different models. In this respect, the MPW model is in excellent agreement with the atomistic one, with $d^z_{COM\text{-}COM} \sim 1.7$ nm, while the other CG models favor a configuration in which the NP is more deeply inserted in the membrane. For what concerns the translocation process, obtained with biased simulations, we observed that different behaviors were predicted by the four models. The differences involve, essentially, the dragging of water molecules and lipid headgroups toward the center of the membrane. To better quantify the dragging effects we considered the average number of contacts of the biased charged ligand terminal with water molecules and with the choline groups of the lipid heads of the entrance leaflet, as shown in Figure 43. For $z < 2.5$ nm, corresponding to configurations in which

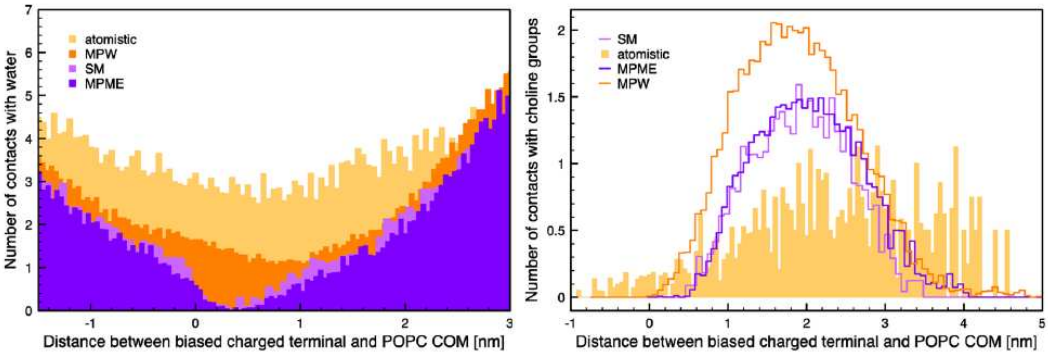

Figure 43: Number of contacts between the biased charged ligand terminal and the water groups (left) and choline (right). To compare atomistic and CG data, the number of contacts with water molecules in the atomistic run has been divided by 4 to account the 4:1 mapping of the MARTINI FF. Taken from [124].

the biased ligand terminal is located above the lipid head region, in the water phase, the atomistic and CG data are in reasonable agreement. As the ligand terminal approaches the center of the membrane, though, the four models predict different scenarios. In the atomistic runs, the number of contacts with water is non-negligible, even at the center of the membrane. In the CG runs, instead, only the MPW model is able to reproduce this feature, still underestimating the number

of water molecules in contact with the translocating ligand. We also monitored the electrostatically favorable contacts between the biased ligand and the choline groups of the entrance leaflet. In the atomistic runs the biased ligand interacts with the choline groups over a broader z range, including when it explores the distal membrane leaflet. All CG models, and especially the MPW model, appear to overestimate the number of ligand–choline contacts. The MPW model shows a slightly wider z range in which ligand–choline contacts are recorded, reaching down to the center of the membrane. These phenomena have to be correlated with the dynamics of transition process. In Figure 44, it is shown the time evolution of

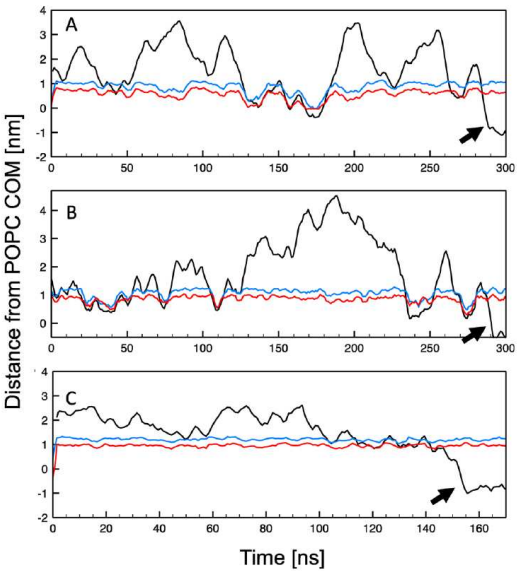

Figure 44: Time evolution of the CV (black line), of the minimum distance between the choline groups of the entrance leaflet and the COM of the membrane (blue), and of the minimum distance between water and the COM of the membrane (red). **A**–**C**. Atomistic, MPW, and SM metadynamics runs, respectively. The arrows indicate the transition to the anchored configuration. Taken from [124].

the CV, before the transition, together with the minimum distance between the choline groups and the COM of the membrane and with the minimum distance between water and the COM of the membrane. We found correlation with the atomistic model and it is correctly reproduced even with the MPW model. In the SM model, instead, the correlation is almost absent. Thus, as visually shown in Figure 45, the biased ligand drags water and lipid headgroups toward the center of membrane while attempting the transition to the anchored state. This is accompanied by important, although local, membrane deformations.

PME AND PW ARE NECESSARY TO FAITHFULLY DESCRIBE THE LIGAND TRANSLOCATION We compared the performances of three versions of the MARTINI FF, namely the standard version with both cut-offed and long range electrostatics (SM and MPME) and the polarisable version (MPW), in reproducing the processes and free energy barriers for the translocation of a charged ligand of a monolayer-protected Au NP across the core of a neutral lipid bilayer. All three CG models are able to reproduce the key features of the hydrophobic contact configuration in which the NP stably resides in the entrance leaflet of the membrane. When looking at the anchoring process, only the MPW model is able to reproduce the molecular mechanisms as observed in the atomistic runs, *i.e.* the formation of ligand-induced

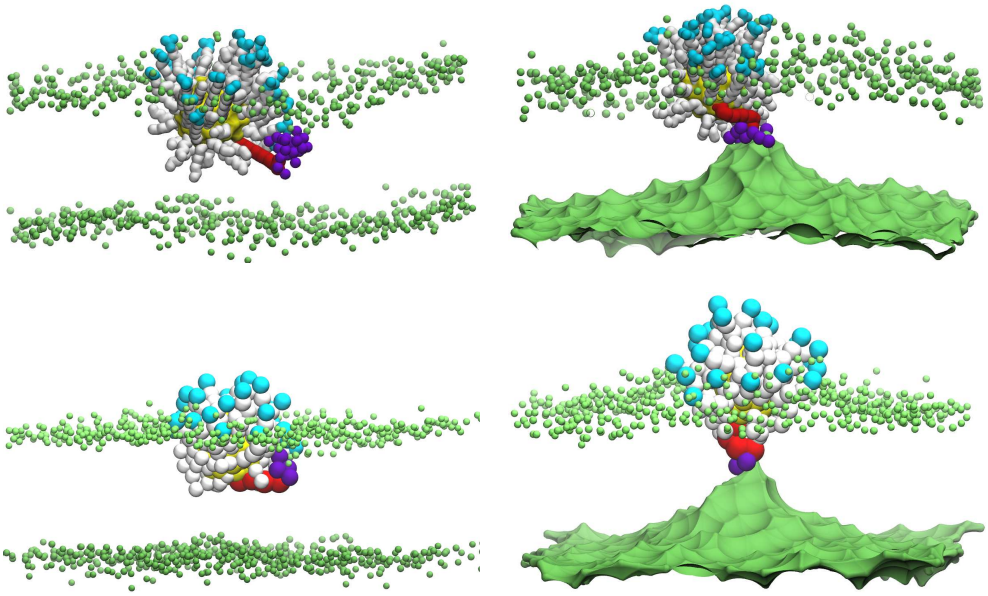

Figure 45: Top row. Snapshots from an atomistic metadynamics run. Biased anionic ligand (red) exploring the central part of the membrane while dragging water molecules (violet) toward the membrane core (left). The biased ligand is anchored to the distal leaflet and deforms it while wandering in the central part of the membrane (right). Bottom row. Similar configurations from a CG metadynamics run performed with the MPW model. Lipid heads of the upper leaflet are in green. Lipid heads of the distal leaflets are represented by a continuous green surface to better visualize the membrane deformation. Lipid tails are not shown. Au and S atoms in yellow, hydrophobic beads in light-gray, negatively charged beads in cyan and water in violet. Adapted from [124].

water defects in the entrance and in the distal leaflet, sometimes involving the translocation of water molecules across the membrane core. Even from a thermodynamic point of view, the translocation barriers calculated with the SM and MPME model are highly underestimated, while the MPW model is in reasonable agreement with the atomistic one. Thus, when looking at the interaction of charged NPs with lipid membranes the SM model remains a valid tool to screen for possible interaction mechanisms in a time-effective way. A more accurate description of electrostatics at CG level, and the use of the MPW model, is nevertheless essential to quantify translocation barriers and describe, as correctly as possible with the CG resolution, the membrane deformations during the interaction process.

LIGAND ARRANGEMENT INFLUENCES THE THERMODYNAMICS OF THE NP–MEMBRANE INTERACTION The ligands on the Au NP surface can be arranged in two possible ways, obtaining a NP with small or large patches, see Figure 25. Looking at the whole Au NP–membrane interaction, as described in Figure 40, we observe that the adsorbed configuration is a meta-stable state for both NP ligand arrangements. Indeed, from unbiased simulations with the SM model, we see that NPs with large patches spend, on average, several microseconds (up to 10 μs) in the adsorbed state before reaching the hydrophobic contact state [123]. Conversely, when NPs with

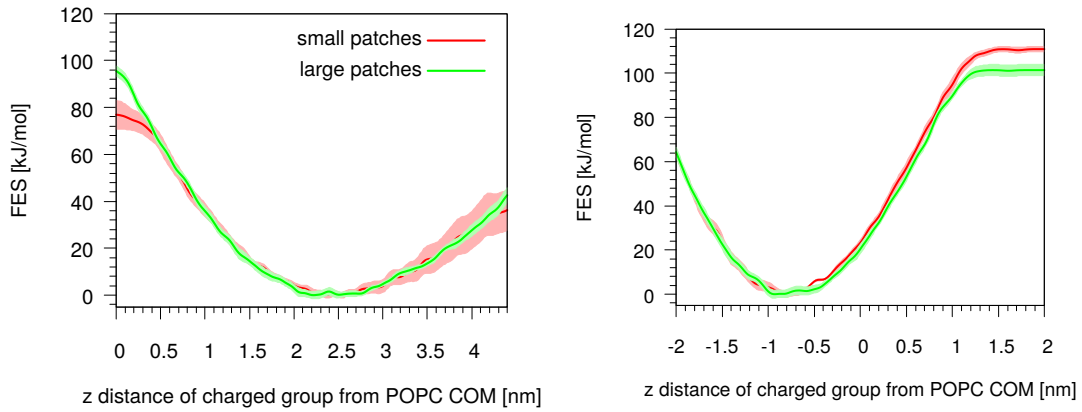

(a) anchoring **(b)** disanchoring

Figure 46: Potential of mean force profiles of the forward anchoring process for the NP with small (red line) or large (green line) patches.

small patches reach the hydrophobic contact state, they take only few nanoseconds before a ligand translocation occures. Thus, different free energy barriers have to be overcome to make the ligand translocation for NPs with different surface ligand arrangements. To be more quantitative, we have analyzed the translocation process with biased metadynamics simulations and the MPW model [124], for both type of NPs. The PMF profiles of the anchoring and disanchoring events for the MUA:OT 1:1 Au NP with small and large patches, are shown in Figure 46. The MPW model confirm the trend observed in [123] with the SM model: the anchoring transition has a free energy barrier of 96 ± 2 kJ/mol for the NP with large patches, and only 77 ± 6 kJ/mol for the NP with small patches. For the backward transition the free energy profiles are similar: for the NP with large patches the free energy barrier to go from the anchored to the hydrophobic contact state is 101 ± 3 kJ/mol and 111 ± 1 kJ/mol for the NP with small patches. This result suggests also that the anchoring and disanchoring transitions for the NP with large patches are more similar and symmetrical to each other than what is observed with the SM model in [123]. The NP with small patches shows, instead, an asymmetry between the anchoring and disanchoring transition: with the first barrier smaller than the second.

Table 10: Free energy barriers for the anchoring (forward) and disanchoring (backward) transition.

(kJ/mol)	large patches	small patches
forward	96 ± 2	101 ± 3
backward	77 ± 6	111 ± 1

5.2 LIGAND PROTONATION MAKES ANCHORING LESS DISRUPTIVE

In the previous section we have characterized the Au NP–membrane interaction and we showed that it is a process that involves the transition between different metastable states. In particular, we have investigated the anchoring transition: one by one, the hydrophilic ligands, initially bound to the headgroup region of the entrance leaflet, translocate the hydrophobic membrane core to bind to the distal leaflet. This transition is crucial since determines the overall time scale of the NP–membrane interaction. We showed, at atomistic and CG level, that the translocation of charged ligands can involve significant membrane deformations, transient membrane poration and overcoming of high free energy barriers.

In this section, we investigate deeper the interaction of a MUA:OT 1:1 Au NP with small patches between a zwtitterionic POPC membrane. In particular, we wonder whether a change of the NP protonation state could be responsible for a less disruptive character of NP–membrane interactions. To answer this question, we will show that:

i. the translocation of protonated (*i.e.* –COOH terminated) ligand makes the NP–membrane interaction a completely non-disruptive process, with little if no perturbatio of membrane integrity during the translocation process.

ii. protonation facilitates the NP–membrane interaction by lowering the free energy barriers along the pathway to the embedding of the NP in the membrane core;

iii. protonation of the carboxylate terminal group of the anionic ligands is more and more favorable as the NP approaches the membrane;

PROTONATED *VS.* CHARGED MUA LIGANDS The MUA ligand, as shown in the top panel of Figure 47, is composed by an acyl chain and a carboxylate terminal group that, depending on the pH of the solution, can be protonated (neutral) or not (negatively charged). It is known that MUA has a $pK_a = 5$ in water solution at physiological pH (pH = 7.4). The protonation reaction is $-COOH \xleftrightarrow{H_2O} -COO^- + H_3O^+$, as shown in Figure 47. According to the Henderson-Hasselbalch relation:

$$pH = pK_a + \log_{10} \frac{[-COO^-]}{[-COOH]} = pK_a + \log_{10} \left(e^{-\beta \Delta G^{dep \to p}} \right) \tag{5.2.1}$$

where $\beta^{-1} = k_B T$. This equation, knowing the pK_a, at constant pH, give us the concentration ratio between the deprotonated and protonated compounds. When adsorbed on the surface of a NP, though, the pK_a of the MUA ligands changes and shifts to larger values. Moglianetti *et al.* [183] have measured an average $pK_a = 6.3$ for MUA ligands adsorbed on the surface of $4-5$ nm Au NPs, suggesting that about one tenth of the MUA ligands are indeed protonated at physiological pH. As the anionic ligands interact with the lipid headgroups and with the membrane

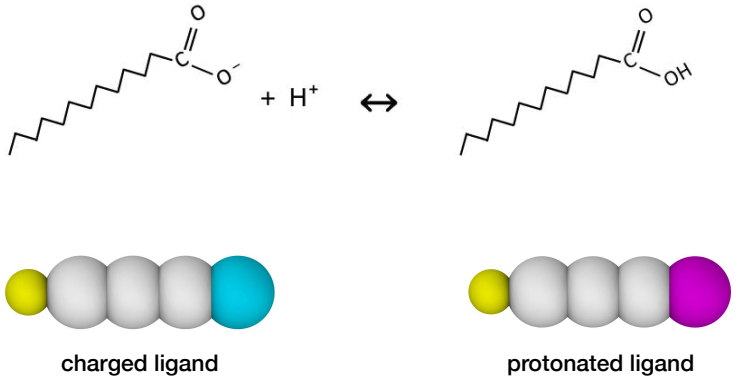

Figure 47: Top panel: MUA ligand protonation reaction. Bottom panel: MARTINImodel of the MUA and MUAH ligand.

interior, they remain hydrated and thus in contact with a proton source, as shown in Figure 49. Could a change of the NP protonation state be responsible for a less disruptive character of NP–membrane interactions?

PROTONATED LIGAND MODEL To simulate a protonated ligand, MUAH, at CG level we have changed the MARTINI type of one charged ligand terminal to represent a protonated carboxyl. According to the MARTINI scheme, the new bead type is P_3, which is neutral but preserves a strong polar character and affinity to the lipid headgroup region. In the bottom panel of Figure 47 it is shown the mapping scheme of the new neutral MUAH ligand in comparison with the negatively charged MUA ligand.

THE TRANSLOCATION OF A PROTONATED LIGAND IS SPONTANEOUS AND LESS DISRUPTIVE We performed unbiased MD simulations starting form a confguration in which: *i.* the NP was in the hydrophobic contact state; and *ii.* the protonated ligand was in contact with the entrance leaflet, as shown in top panel of Figure 48. In this condition we observe many spontaneous anchoring and detachment events of the protonated ligand to and from the distal leaflet. The fast anchoring kinetics, shown in the left panel of Figure 49, indicates the presence of a much smaller anchoring barrier than for the charged ligand. Translocation events did not cause evident membrane deformations, as shown in right panel of Figure 48, and no translocation of water beads was ever observed during the protonated ligand anchoring, as shown in the right panel of Figure 49. The unbiased run thus suggests that, if the interaction of the NP with the membrane could induce protonation of the charged ligands, this would turn into a faster and less disruptive interaction with the membrane.

PROTONATION LOWERS THE FREE ENERGY BARRIER FOR TRANSLOCATION To be more quantitative, we use biased metadynamics simulations to calculate the free energy barriers for the translocation of one protonated ligand (bound to the NP, as in Figure 48) across the membrane, as shown in the central panel of Figure 50, in

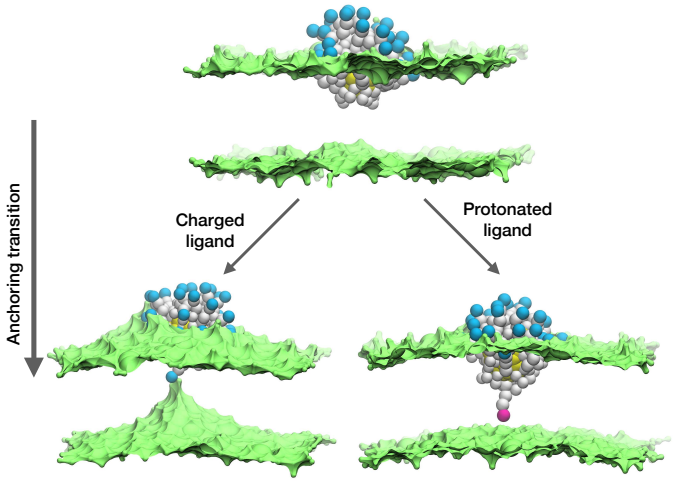

Figure 48: Scheme of the translocation process: starting from the hydrophobic contacts state to the anchored state in a comparison between the charged (left) and the protonated (right) ligand.

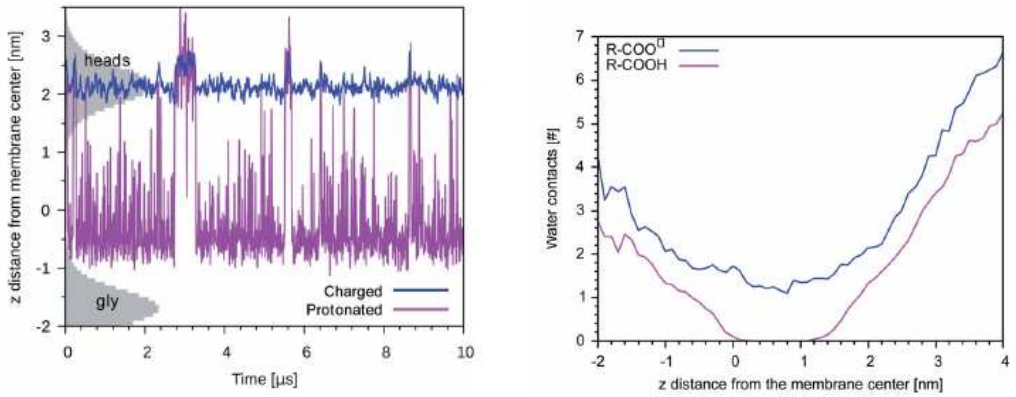

Figure 49: (a) Plot of d_z for a protonated ligand (fuchsia) or of a charged one (blue), during an unbiased simulation with a single protonated ligand. In the starting configuration both the protonated and the charged ligand were bound to the entrance leaflet ($2 < d_z < 2.5$ nm). When bound to the distal leaflet, the protonated ligand has d_z in $-1.0 < z < 0.5$ nm range. The shaded grey areas indicate the distribution of lipid heads (top leaflet) and glycerol groups (bottom leaflet. (b) Average number of contacts between the biased ligand terminal and the CG water groups as a function of its z distance from the bilayer COM. Data from [126].

comparison with the translocation of the charged ligand. As shown in the previous section, the anchoring barrier of the negatively charged ligand for a NP with small patches is 76 ± 6 kJ/mol. The PMF of the protonated ligand instead, shows a first small barrier of about 2 kJ/mol followed by a substantially flat landscape. For the protonated ligand, the free energy difference between the two metastable states (in the entrance and distal leaflets) is about -4 kJ/mol, in favor of the anchored configuration. These small barriers and free energy differences between metastable states are consistent with the fast kinetics observed during the unbiased run.

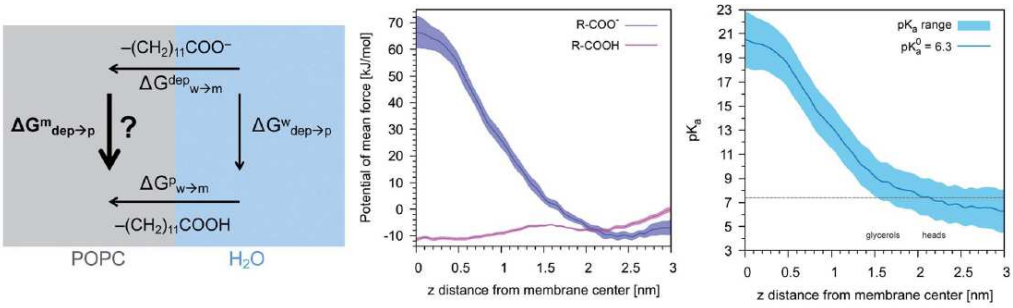

Figure 50: Left: The thermodynamic cycle used to calculate the pK_a of the ligand *vs.* d_z. Center: The PMF profile for the protonated and deprotonated ligand as a function of d_z. Shaded areas show the statistical error on ΔG, which was obtained by averaging over 8 metadynamics runs. Right: The pK_a of the ligand *vs.* d_z. The shaded area shows a conservative estimate of the indeterminacy with which the pK_a of the ligand in water is known: the free ligand has a pK_a of 5 (bottom edge of the shaded area for $d_z = 3$ nm), while cooperative effects on the NP surface have been predicted to shift the pK_a of similar ligands up to 7.6 (upper edge of the shaded area). Using 6.3 as reference pK_a value in water, the light-blue profile is obtained and the error bars deriving from our metadynamics calculations lay within the shaded area. The shaded grey areas indicate the distribution of lipid heads and glycerol groups. Taken from [126].

NP–MEMBRANE INTERACTION MAKES PROTONATION MORE AND MORE FAVOURABLE

We have showed that: *i.* the translocation of protonated (*i.e.* –COOH terminated) ligand makes the NP–membrane interaction a completely non–disruptive process, with little if no perturbation of membrane integrity during the translocation process; and *ii.* the protonation facilitates the NP–membrane interaction by lowering the free energy barriers of the translocation process, along the pathway to the embedding of the NP in the membrane core.

In order to verify if the protonation of the carboxylate terminal group of the anionic ligands is more and more favorable as the NP approaches the membrane, we need to calculate the effective ligand pK_a as a function of the distance z, along the membrane normal, between the ligand terminal and the COM of the membrane. To this aim, we set–up a thermodynamic cycle, as also previously done by MacCallum *et al.* [184] and shown in the first panel of Figure 50. The two horizontal segments of the cycle correspond to the free energy of transfer of the ligand (protonated, $\Delta G^{p}_{w\to m}$ or deprotonated, $\Delta G^{dep}_{w\to m}$) from the water phase to distance z from the COM of the membrane. The PMF profiles of the deprotonated and protonated ligands are shown in the central panel of Figure 50, as obtained with the metadynamics simulations. The offset between the two free energy profiles (right vertical segments) of the cycle is provided by the pK_a of the ligand in the water phase, which we assume to be 6.3 as measured in [183]. The offset has been calculated with Equation (5.2.1). The cycle can thus be used to calculate the unknown free energy change associated to ligand protonation at distance z from the center of the membrane, $\Delta G^{m}_{dep\to p}$, which is then related to the ligand pK_a *via* Equation (5.2.1). The right panel of Figure 50 shows the resulting pK_a as a function of z. The shaded area shows a conservative estimate of the indeterminacy

with which the pK_a of the ligand in water is known: the free ligand has a pK_a of 5 (bottom edge of the shaded area for $z = 3$ nm from the membrane center), while cooperative effects on the NP surface have been predicted to shift the pK_a of similar ligands up to 7.6, as shown in [185] (upper edge of the shaded area). Using 6.3 as reference pK_a value in water [183], the light–blue profile is obtained and the error bars deriving from our metadynamics calculations lay within the shaded area. The shaded grey areas indicate the distribution of lipid heads and glycerol groups. From this results we conclude that the interaction of the membrane makes protonation more and more favourable. Since the pK_a equals the physiological pH of 7.4 in the lipid heads region, all the charged ligands reaching down to the glycerol region should be protonated and be able to translocate to the distal leaflet of the membrane without perturbing membrane structure or induce water transfer.

CONSTANT–PH SIMULATIONS We further exploited the knowledge of the z–dependent pK_a of the titrable sites of the anionic ligands to perform constant–pH simulations of the NP–membrane interaction. One run was initialized as in the top left panel of Figure 48 and, at regular intervals of time, $\Delta t = 10$ ns, the protonation state of each ligand was reassigned based on its pK_a value. The choice of Δt is arbitrary and affects the kinetics of the process, but this setup allows to monitor membrane deformations, during the translocation of many neutral –COOH terminated beads, without the interference of any bias potential. During the run we observe that, as the number of protonated ligands increases, the translocation events increase too, as shown in the top graph of Figure 51. Coherently, the NP penetrates deeper and deeper into the bilayer, as shown in the bottom graph of Figure 51. If the anchored ligand remains protonated, the back transition is favorable as well, causing some fluctuations on the number of anchored ligands. We remark that none of these anchoring and disanchoring events was accompanied by translocation of water beads, and we did not observe any significant membrane deformation during the anchoring process. The first anchoring event of a protonated ligand occur in few ns. Then, after, about 0.2 μs, the NP is stably inserted in the membrane. At this stage, the number of anchored ligands fluctuates around 10 while the number of protonated ligands fluctuates between 10 and 20. From about 1 μs on we observe that some ligands anchored to the distal leaflet start to change their protonation state, coming back to the negatively charged state and making the back- transition unfavorable. In fact, we do not observe any back-transition for the ligands that becomes negatively charged. From 1 to 2 μs the number of anchored ligands increases up to 15 and the NP distance from the membrane COM vanishes and becomes, in some cases, even negative. The NP thus results fully immersed in the membrane with roughly half ligands anchored to the entrance leaflet, and half to the distal one. This configuration is subject to fluctuations – indeed, after ~ 2 μs the number of anchored ligands suddenly decreases and the NP gets back to a distance of ~ 0.5 nm from the membrane COM. We can speculate that, due to fluctuations, the distance between the NP and the center of the bilayer could become more and more negative, leading to a complete transition of the NP from the entrance to the distal leaflet.

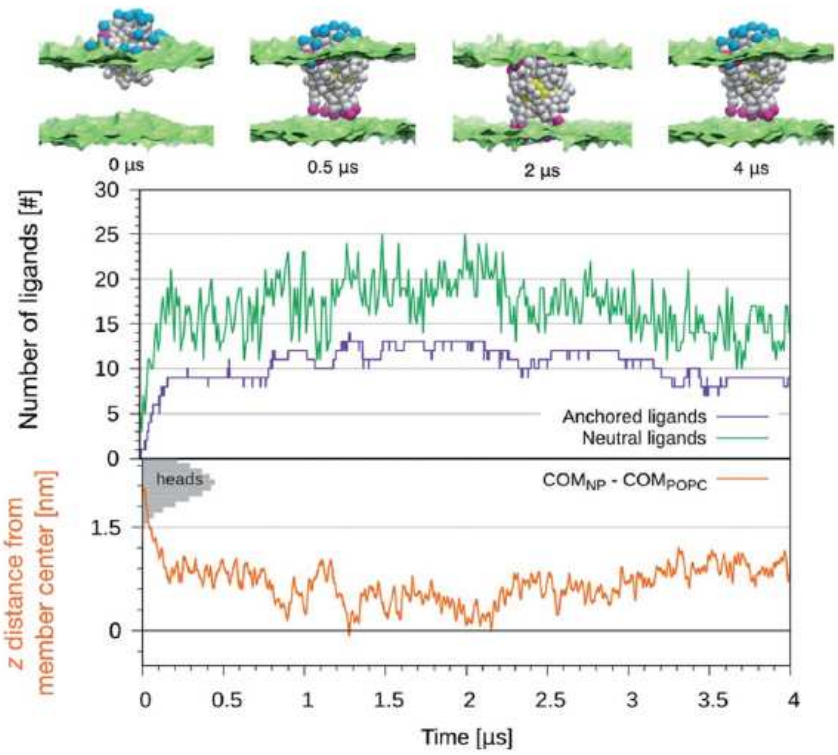

Figure 51: Top: The figures show the configurations of the NP as it is progressively embedded in the membrane. Charged beads in blue, protonated beads in fuchsia and hydrophobic beads in white. Lipid heads are shown in green as surface representation, water and lipid tails are not shown. Bottom: The number of anchored ligands (violet), the protonated ligands (green) and d_z for the NP COM as a function of the simulation time. The shaded grey areas indicate the distribution of lipid heads of the entrance leaflet. Taken from [126].

6 EFFECT OF CHARGE AT NP – PROTEIN INTERFACE

Upon the intravenous administration of Au NPs for biomedical applications, the NPs come in contact with serum proteins. These proteins can non-specifically interact with the NP and adhere on its surface, leading to the creation of a highly complex protein corona [39, 41]. Such non-specific deposition of proteins on the NP surface hinders the targeting capabilities of the NP since the protein corona is now the "new" surface functionalisation that the organism sees. Moreover, the protein corona could increase the NPs uptake rate by the immunological system, which removes them from the bloodstream. This, again, reduces the NP blood circulation time, which affects the targeting and/or delivery efficiency, thus requiring a higher administered dose [39, 41, 186, 187].

Studying and controlling the formation of the protein corona is nowadays one of the main challenges of the engineering of Au NPs for biomedical applications. Important research efforts are being devoted to the understanding of the nature of the proteins that bind to NPs, as well as to the understanding of the static/dynamic nature of the corona. These studies have to be based on fundamental physico-chemical understanding of the binding capability of proteins to NPs, and *vice versa*. Several factors influence the corona characteristics, such us NP size, surface functionality, charge and hydrophobicity. In this perspective computational studies can coordinate with experiment to first track the composition of the corona and then study if a pattern exists explaining the NP–protein interaction. Thus, being able to functionalize NPs with specific molecules which bind only selected proteins or not will allow to achieve a better control of the fate of Au NPs in the body.

In this chapter, we have addressed this problem at both experimental and computational level by concurrently determining protein binding geometry and binding energetics across a series of Au NPs which differ in surface charge. We study the interaction between ligand protected Au NPs and ubiquitin protein. We aim to provide a computational interpretation to the experimental results provided by the group of Francesco Stellacci on the same NP–ubiquitin system. More specifically, the aim is to provide a molecular interpretation of the NP–ubiquitin interaction and of its dependence on the interface characteristic of the NP itself. In the first part of the chapter, we give a brief introduction to proteins, as well as to ubiquitin and its computational model. We briefly summarize the main experimental results and then we analyze the computational results about NP–ubiquitin interaction, showing how the NP surface charge can influence the stability of the NP–ubiquitin aggregate.

UBIQUITIN It is a small protein that exists in all eukaryotic cells and occurs ubiquitously. The protein consists of 76 amino acids, it has a molecular mass of about 8.6 kDa and it displays a α-helix and one-β sheet, as shown in Figure 52a. Ubiquitin is involved in a myriad of functions through conjugation to a large range of target proteins. In particular, ubiquitin is involved in the so called *ubiquitination* process: the addition of ubiquitin to a substrate protein. Ubiquitination affects proteins in many ways: it can mark them for degradation, alter their cellular location, affect their activity, and promote or prevent protein interactions. Moreover, the ubiquitination system functions in a wide variety of cellular processes, including: antigen processing, apoptosis, biogenesis of organelles, cell cycle and division including DNA transcription and repair, immune response and inflammation, neural and muscular degeneration and so on. The structure of human ubiquitin is available in the PDB which is determined via x-ray diffraction crystallography [150] at a resolution of 0.18 nm. The protein is neutral, but it has the C and N termini, respectively, negatively and positively charged. A snapshot of the CG MARTINI representation of ubiquitin is shown in Figure 52b, while its model is detailed in Section 3.3.

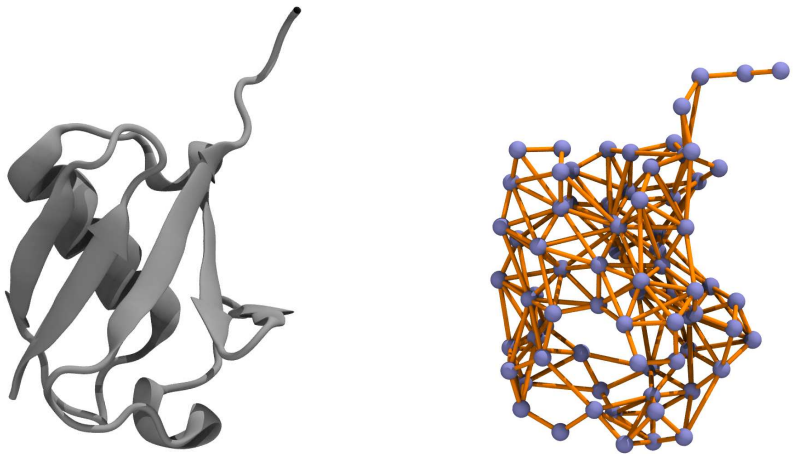

(a) atomistic staurcture **(b)** MARTINI structure

Figure 52: (a) Atomistic structure of the ubiquitin protein with the α-helix behind the β-sheet. (b) MARTINI CG mapping with the ELNEDYN elastic network (orange sticks) superimposed to the backbone beads (light blue). Side chain beads not shown. CG model detailed in Section 3.3.

6.1 NP – UBIQUITIN INTERACTION — EXPERIMENTAL RESULTS

The experiments presented here hae been performed by Ahmet Bekdemir under the supervision of Prof. Francesco Stellaci at the Istitute of Materials, École Polytechnique Fédérale de Lausann [188]. They addressed the interaction between passivated Au NPs and ubiquitin by mens of nuclear magnetic resonance (NMR) spectroscopy. More specifically, as summarized in Figure 53, they synthesized Au

NPs with two different sizes, 4 nm and 6 nm core diameter, fully coated with either MUS or MUA, as well as a stoichiometric mixture with OT with approximately 2:1 hydrophilic to hydrophobic molar ratio. Measurements of the ζ-potential of the Au NPs indicated that sulfonate NP bear significantly more negative charges than carboxylate NP. Moreover, it can be extrapolated that the charge of MUA NP is about $1/5$ of MUS NP, thus $4/5$ of the carboxylate ligands on the surface of MUA NP can be considered protonated.

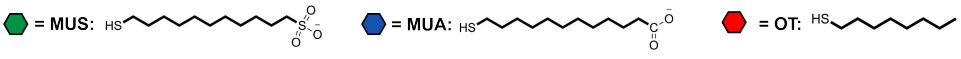

	allMUS(4)	MUSOT(4)	allMUA(4)	MUAOT(4)	allMUS(6)	MUSOT(6)	allMUA(6)	MUAOT(6)
Ligand type								
Core Diameter	4.0±0.6	4.1±0.7	4.2±0.7	4.0±0.7	6.2±0.8	6.3±1.0	6.5±0.9	6.2±1.5
TEM								
OT (%) NMR	0	31±3	0	32±3	0	33±3	0	32±3
ζ-potential 10 mM PB (pH 7.4)	-35±4	-28±6	-10±1	-8±1	-34±5	-30±3	-12±2	-11±2

Figure 53: Summary of synthesized NPs which differ in core diameter, surface chemistry and charge. Courtesy of Ahmet Bekdemir [188].

UBIQUITIN IS STABLE UPON INTERACTION WITH NPS Circular dichroism spectra of a mixture of ubiquitin with carboxylate or sulfonate NPs have shown no change in ubiquitin's conformation upon mixing with NPs. This confirmed that ubiquitin structure is retained upon contact with NPs and no conformational change occurs. This result is robust against variation of the different NP concentration. This analysis justifies our choice to use the CG ELNEDYN elastic network to model ubiquitin protein in our MD simulations, as described in the Section 3.3.

UBIQUITIN STABLY INTERACTS WITH NPS Using ^{15}N NMR spectroscopy analysis, it is possible to determine NP-protein binding geometry. In particular, experiments on ^{15}N-labeled protein samples enable monitoring residue-level effects at high sensitivity, in particular that the degree of signal attenuation in ubiquitin spectra is directly related to the interaction with NPs and provide information about which residues are affected upon NP binding. Indeed, in all NP-ubiquitin mixtures, it is observed a global decrease of signal intensities in the NMR spectrum which is attributed to the NP binding. The analysis of the NMR spectra revealed that ubiquitin binding is well-defined, not stochastic. Moreover, the residues of ubiquitin that interact with the NP are well-defined and not changing with respect to NP concentration. The experimental information of the local binding geometry is

shown in Figure 59(a-d), in which the ubiquitin residues involved in the NP interaction are red-colored.

HYDRODYNAMIC DIAMETER OF NPS The calculation of the hydrodynamic diameter, d_{hydro}, of all NPs relies on sedimentation and diffusion coefficients, separately computed through analytical ultracentrifugation (AUC) based methods [189, 190]. Because it is safe to assume that all NPs in this study are spherical and have roughly the same organic shell extension, the difference between the d_{hydro} and core diameter, obtained from electron microscopy images (Figure 53), gives reliable estimate of the thickness of the hydration layer of each NPs in the same conditions, as shown in Figure 54. According to this estimation, carboxylate NPs do not largely

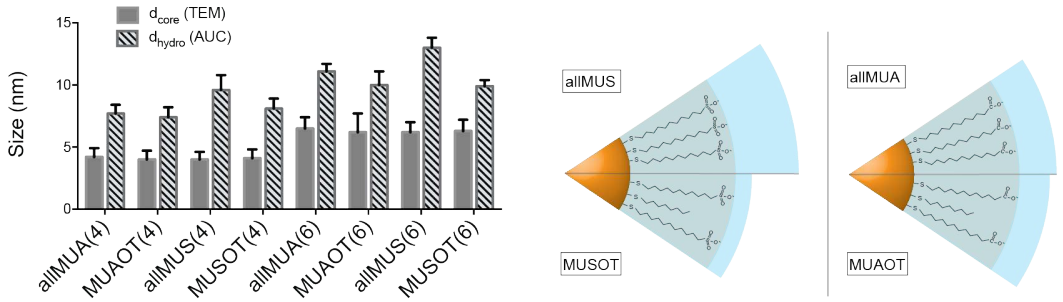

Figure 54: Hydrodynamic diameter (d_{hydro}) computed through analytical ultracentrifugation (AUC) based methods for different NPs. Courtesy of Ahmet Bekdemir [188].

differ from each other in hydration layer irrespective of size and hydrophobicity. On the other hand, sulfonate coated NPs are more sensitive, in terms of hydration layer, to their hydrophobic (OT ligands) content. Between allMUS and MUSOT NPs, there is a decrease of d_{hydro}. Nevertheless, MUS NPs show the higher d_{hydro}, while it is lower for MUA or OT-containing NPs, that show almost the same d_{hydro}, within the error bars.

6.2 NP – UBIQUTUIN INTERACTION — SIMULATION RESULTS

On the computational side, we studied the interaction of Au NPs-ubiquitin interaction with CG MD simulations. The Au NPs considered at simulation level are functionalized with the same ligand used in the experiments (Figures 53 and 55): we considered fully coated NPs with either MUS or MUA, as well as the stoichiometric mixture with OT at 2:1 hydrophilic to hydrophobic molar ratio. Though, they differ in the core diameter: for computational reasons, we considered Au NP with a diameter of 2 nm, as already described in Chapter 3. The CG MARTINI models of the Au NP and ligands are describe in Section 2.3.3.

The NPs we considered with MD simulations are summarized in Figure 55 and Table 11. For what concerns the MUA NP, as pointed out by the ζ-potential, it has $^1/_5$ of MUS NP charge. Thus, $^4/_5$ of the hydrophilic ligands are protonated (the model of the protonated MUA ligand, as well as the protonation process, is

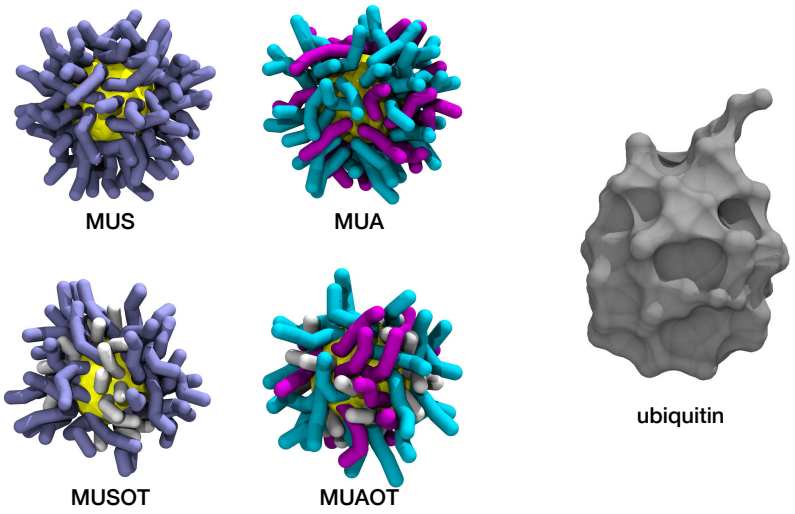

Figure 55: Left: Snapshot of the different NPs used at CG resolution. NP core in yellow, MUS ligands in violet, MUA in cyan, MUAH (the protonated MUA ligand) in magenta and OT in white. Right: CG surface representation of ubiquitin.

described in Section 5.2). We remark, also, that the MARTINI model for MUA and MUS ligands is the same since both ligands have a negatively charged terminal group. The way we have to distinguish, at CG level, NPs functionalised with MUA or MUS rely on the fact that, contrary to MUA ligands, MUS one cannot perform the protonation reaction, thus its charge is fixed independently on the pH of the solution. Thus, the real difference, at the CG level, between the MUS or MUA NPs is the net surface charge, which is summarized in Table 11.

NP name	radius [nm]	composition	ligand concentration	protonation degree[a]	charge [e]
MUS	2	MUS	60	0	60
MUA	2	MUA:MUAH	12:48	4/5	12
MUSOT	2	MUS:OT	40:20	0	40
MUAOT	2	MUA:MUAH:OT	8:32:20	4/5	8

Table 11: Composition of all NPs used in CG MD simulations. [a] We defined the protonation degree as the ratio between the protonated ligands over the total number of hydrophilic ligands.

SIMULATION SETUP To characterize the NP–ubiquitin interaction, we performed unbiased CG MD simulations in which a single NP was allowed to interact with a single ubiquitin. We ran a 10 μs simulation for each NP in Table 11. The simulation box is solvated with about 30000 PW molecules and, where needed, Na^+ counter ions are added. The simulations is performed with a time step of 0.16 fs in the NPT ensemble ($T = 310$ K and $p = 1$ bar).

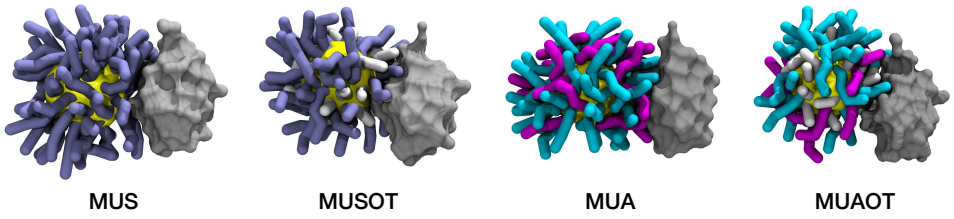

Figure 56: Snapshot of the NP–ubiquitin aggregates. Color code as Figure 55.

BINDING GEOMETRY: SIMULATIONS AGREE WITH EXPERIMENTS In the CG MD simulations, we observed that all NPs stably interact with ubiquitin within the microsecond time scale. In Figure 56 are shown the NP–ubiquitin aggregates among the different NPs. To compare the experimental local binding geometry, we analyzed the time-averaged contacts between NP and ubiquitin as a function of the residues number (distance cut-off of 0.8 nm), normalized to the total number of beads per residue (Figure 57). Figure 59(e-h) shows the simulated local binding geometry, in which the residues with the normalized contacts higher than 0.5 are red-colored. Among the different NPs, we see a good agreement with the experiments for what concerns the side of the protein involved in the NP–ubiquitin interaction. Some differences can be observed in the residues involved in the interaction. These differences may be affected by the chosen cut-off value. Overall, we consider to have a satisfactory agreement between the experiment and the CG model.

ALL NPS SHARE THE SAME BINDING GEOMETRY In Figure 57, it is shown the time-averaged contacts between NP and protein residues as a function of the residue number. From the contact analysis, we see almost negligible differences in the residues involved in the interaction among the different NPs. Thus, at the simulation level, almost the same local binding geometry is shared between carboxylate and sulfonate NPs. However, a slight difference could be observed in the peak intensities of OT-containing NPs that are higher than that of MUA or MUS NPs. Despite the different net charge, almost no difference in the binding geometry and in the number of binding contacts is observed between MUA and MUS NPs.

SURFACE CHARGE INFLUENCE THE NP – UBIQUITIN AGGREGATION Contrary to the local binding geometry, which seems to be shared among the different surface functionalizations, we observe a different behavior in the binding kinetics and in the stability of the aggregates over time. During the simulations, the all-to-all NP–protein contacts are computed as a function of time, with a distance cut-off of 0.8 nm. Then, they are smoothed through a Gaussian filter ($\sigma = 8$) and a contact cut-off of 20 is used to determine if the NP is in contact with the protein or not[1]. In Table 12, it is shown the number of detachment events observed along a 10 μs

1 The average number of contacts in the attached state is about 200.

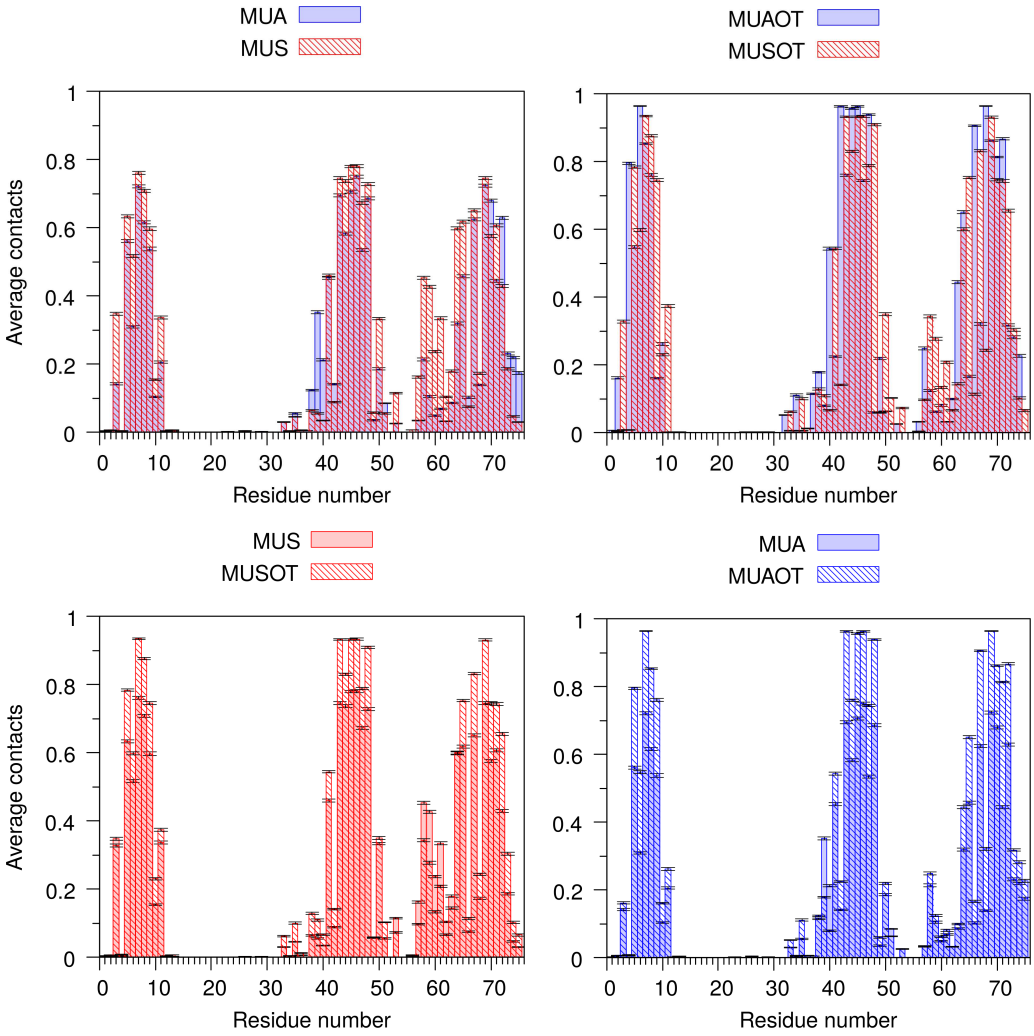

Figure 57: Histograms of the time-averaged normalized contacts between NP and protein residues as a function of the residue number.

long trajectory. We see that reducing the NP surface charge, (by increasing the protonated *vs.* charged ligands ratio or by adding OT), the number of detachment events, as well as the time in which the NP is detached from the protein, decrease.

This behavior is coherent with the differences in the histograms described above (Figure 57) and with the experimental hydrodynamic radius (Figure 54). Indeed, we observe that NP with the largest hydrodynamic radius (MUS or MUA NPs) are those that detach from ubiquitin more easily and spend less time in the dimer state. Could this behaviour be influenced by the strength of the interfacial water interacting with the NP surface?

To characterize the NP–water interface and to provide a quantitative estimation of the effective strength of interfacial water, we computed the characteristic water confinement energy, as described in Section 4.2 and 4.3. To this purpose, we performed atomistic MD simulations of one NP in the water phase, for each NP in Table 11 (for the atomistic model of ligands see Section 3.1.2). The strength of

NP name	Detachment events	Detached time [μs]
MUS	6	2.1
MUA	3	0.7
MUSOT	1	0.2
MUAOT	0	0

Table 12: Detachment events captured during a 10 μs long trajectory, in which a NP is freely able to interact with the protein. If the NP starts detached from the protein, the time to rich the aggregated state is not counted.

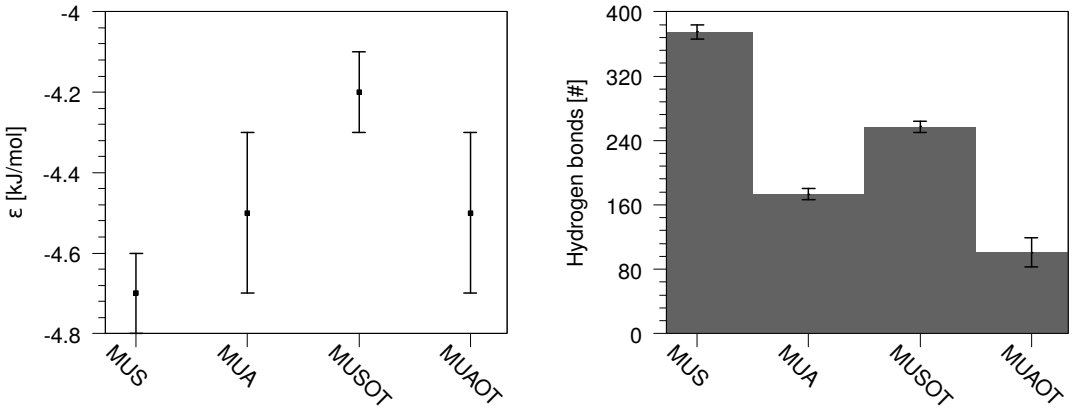

Figure 58: Left: Water confinement energy, ϵ. Right: Number of hydrogen bonds between NP and water molecules.

water molecules interacting with NP ligands can be qualitatively related to the experimental hydrodynamic radius (Figure 54). Indeed, as shown in Figure 58, water molecules have a stronger interaction with MUS NP than with MUA or OT-containing NPs. This suggests that water molecules are highly confined at MUS NP–water interface, discouraging the interaction with the protein: a thick and strongly confined water layer around the MUS NP needs to be removed before the MUS NP can effectively bind to ubiquitin. Moreover, the stronger water layer around the MUS NP can be related to the total number of hydrogen bonds that the NP can form with interfacial water molecules, as shown in Figure 58. Hence, the more structured interfacial water layer around the highly charged sulfonate NPs is responsible, in agreement with the experimental observations, for increasing the hydrodynamic radius, the number of the detachment events from ubiquitin and the time spent by the nanoparticle detached from ubiquitin.

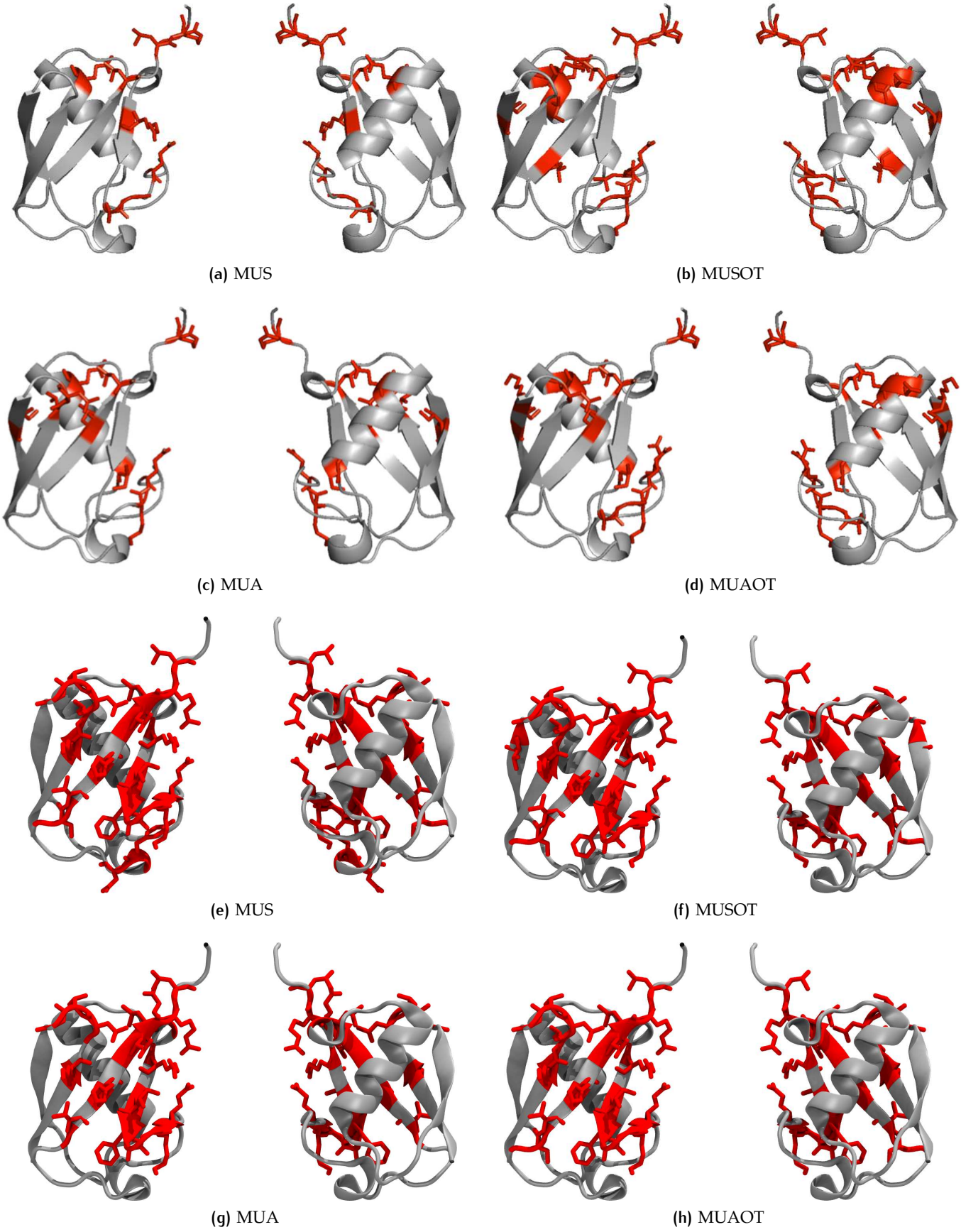

(a) MUS (b) MUSOT

(c) MUA (d) MUAOT

(e) MUS (f) MUSOT

(g) MUA (h) MUAOT

Figure 59: Local binding geometry represented in the atomistic 3D structure of ubiquitin from experimental results (a-d) and CG MD simulations (e-h). Residues involved in the NP–protein interaction are red-colored.

CONCLUSIONS

In this thesis, we used molecular dynamics simulations to investigate, at the molecular level, the interaction that occurs at the interface between small functionalized Au nanoparticles and different biological systems.

NANOPARTICLE – SOLVENT INTERACTIONS IN PHOTOPORATION APPLICATIONS

We studied the interaction of functionalized Au nanoparticles and water under intense, short-pulsed laser irradiation, to understand how surface functionalization influences the thermal gradient around the nanoparticle.

For bare Au nanoparticles and hydrophilic ligand-coated nanoparticles, the temperature profile exhibits a single steep descent at the Au–ligand interface. Instead, a different temperature profile is found in the case of fully hydrophobic ligands, which are able to retain a higher temperature in the volume occupied by the ligand shell. We have rationalized this result in terms of interfacial water dynamics at the three-component Au nanoparticle–ligand–water interface. The large water mobility registered only in the case of completely hydrophobic ligands prevents interfacial water from exchanging heat with the hot nanoparticle and ligands, thereby increasing the thermal resistance at the ligand–water interface and causing significant heating of the ligand shell. On the contrary, water is more effectively confined at the interface with hydrophilic ligands, promoting nanoparticle-to-solvent heat transfer.

We proposed a computational approach that could be used to predict which functionalization would be more efficient at creating a spatially confined hot region around the nanoparticle. Our approach is based on the use of short equilibrium molecular dynamics runs and it could be easily exported to the case of larger nanoparticles, coated by more massive organic ligands. These results, together with the knowledge of the nanoparticle absorbance, could finally allow the estimation of the temperature rise occurring in the biological components in direct contact

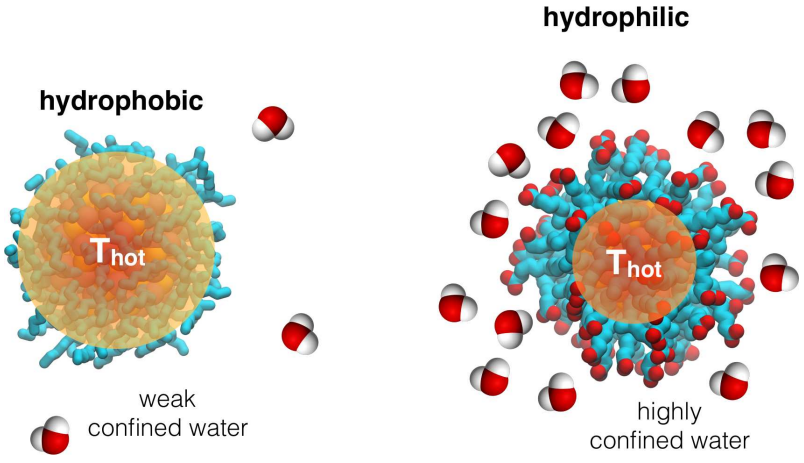

with theranostic Au nanoparticles, such as lipids and plasma membrane proteins in photoporation applications.

NANOPARTICLE – ZWITTERIONIC MEMBRANE INTERACTIONS

We studied the interaction between Au nanoparticles, functionalized by a mixture of hydrophobic and anionic ligands, and zwitterionic lipid membranes, to understand how surface functionalization (in particular, the use of sulfonate *vs.* carboxylate ligands) influences the molecular mechanisms and the thermodynamics of nanoparticle–lipid interactions. We found that nanoparticles can stably interact with zwitterionic model lipid membranes. Nevertheless, the interaction between charged (sulfonate) ligands and the lipid bilayer requires the overcoming of large free energy barriers, and implies significant deformations of the membrane structure. On the contrary, carboxylate ligands – whose protonation is enhanced during nanoparticle–membrane interaction – can interact with the membrane in a faster and less disruptive way.

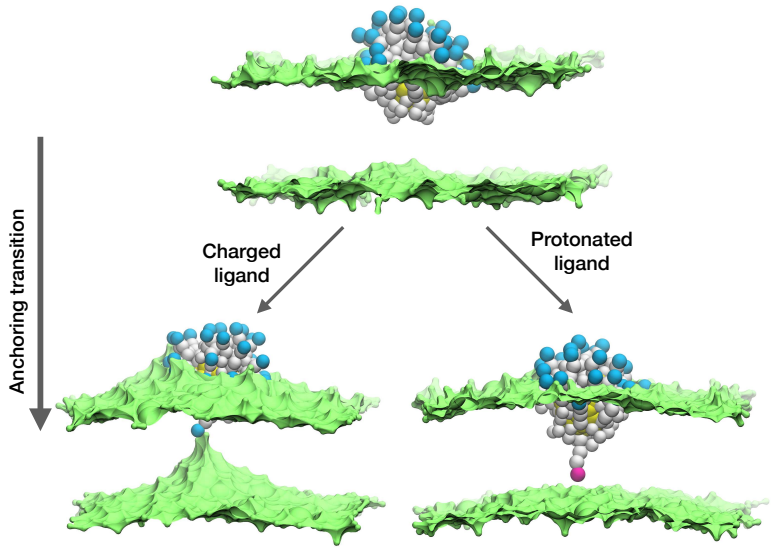

NANOPARTICLE – SERUM PROTEIN INTERACTIONS: THE CASE OF UBIQUITIN

We studied the interaction between Au nanoparticles, functionalized by a mixture of hydrophobic and anionic ligands, and ubiquitin, an important component of serum and of nanoparticles' protein coronas, to understand how surface functionalization influences the kinetics and thermodynamics of nanoparticle–protein binding.

We coupled our computational techniques to experimental results (nuclear magnetic resonance and analytical ultracentrifugation data) to concurrently determine protein binding geometry and binding energetics across a series of gold nanoparticles which differ in the surface chemistry and charge.

We found that all the gold nanoparticles considered here can stably interact

with ubiquitin within the microsecond time scale, and with a similar binding geometry. The kinetics of binding to the protein, though, differs depending on the nanoparticle surface charge. Interfacial water molecules are more bound around the nanoparticles with the largest negative charge (sulfonate ligands), and this reflects in an increase of their hydrodynamic radius and in fewer nanoparticle–protein binding events during unbiased simulations.

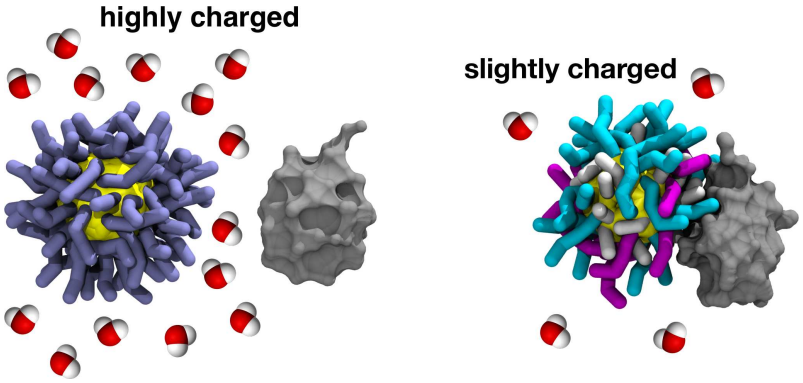

These results, which complement the increasing amount of experimental data on the subject of nanoparticle–bio interactions, contribute to shed light on the elusive molecular mechanisms that take place at the nano–bio interface.

BIBLIOGRAPHY

1. Wang, X., Liu, L.-H., Ramström, O. & Yan, M. Engineering Nanomaterial Surfaces for Biomedical Applications. *Experimental Biology and Medicine* **234,** 1128–1139 (Oct. 2009).
2. Gagner, J. E., Shrivastava, S., Qian, X., Dordick, J. S. & Siegel, R. W. Engineering nanomaterials for biomedical applications requires understanding the nano-bio interface: A perspective. *Journal of Physical Chemistry Letters* **3,** 3149–3158 (2012).
3. Navya, P. N. & Daima, H. K. Rational engineering of physicochemical properties of nanomaterials for biomedical applications with nanotoxicological perspectives. *Nano Convergence* **3,** 1–14 (2016).
4. Ramos, A. P., Cruz, M. A., Tovani, C. B. & Ciancaglini, P. Biomedical applications of nanotechnology. *Biophysical Reviews* **9,** 79–89 (2017).
5. Wang, Y., Cai, R. & Chen, C. The Nano-Bio Interactions of Nanomedicines: Understanding the Biochemical Driving Forces and Redox Reactions. *Accounts of Chemical Research* **52,** 1507–1518 (2019).
6. Zhou, Q., Zhang, L. & Wu, H. Nanomaterials for cancer therapies. *Nanotechnology Reviews* **6,** 473–496 (2017).
7. McNamara, K. & Tofail, S. A. M. Nanoparticles in biomedical applications. *Advances in Physics: X* **2,** 54–88 (Jan. 2017).
8. Liu, D., Yang, F., Xiong, F. & Gu, N. The Smart Drug Delivery System and Its Clinical Potential. *Theranostics* **6,** 1306–1323 (2016).
9. Yan, L., Zhao, F., Wang, J., Zu, Y., Gu, Z. & Zhao, Y. A Safe-by-Design Strategy towards Safer Nanomaterials in Nanomedicines. *Advanced Materials* **31,** 1–33 (2019).
10. Liao, H., Nehl, C. L. & Hafner, J. H. Biomedical applications of plasmon resonant metal nanoparticles. *Nanomedicine* **1,** 201–208 (Aug. 2006).
11. Chaloupka, K., Malam, Y. & Seifalian, A. M. Nanosilver as a new generation of nanoproduct in biomedical applications. *Trends in Biotechnology* **28,** 580–588 (2010).
12. Azam, A., Ahmed, A. S., Oves, M., Khan, M. S., Habib, S. S. & Memic, A. Antimicrobial activity of metal oxide nanoparticles against Gram-positive and Gram-negative bacteria: a comparative study. *International journal of nanomedicine* **7,** 6003–6009 (2012).
13. Hong, H., Shi, J., Yang, Y., Zhang, Y., Engle, J. W., Nickles, R. J., Wang, X. & Cai, W. Cancer-Targeted Optical Imaging with Fluorescent Zinc Oxide Nanowires. *Nano Letters* **11,** 3744–3750 (Sept. 2011).

14. Liu, T.-Y., Liao, H.-C., Lin, C.-C., Hu, S.-H. & Chen, S.-Y. Biofunctional ZnO Nanorod Arrays Grown on Flexible Substrates. *Langmuir* **22,** 5804–5809 (June 2006).

15. Wang, T., Jiang, H., Wan, L., Zhao, Q., Jiang, T., Wang, B. & Wang, S. Potential application of functional porous TiO2 nanoparticles in light-controlled drug release and targeted drug delivery. *Acta Biomaterialia* **13,** 354–363 (2015).

16. Tan, A. W., Pingguan-Murphy, B., Ahmad, R. & Akbar, S. A. Review of titania nanotubes: Fabrication and cellular response. *Ceramics International* **38,** 4421–4435 (2012).

17. Özkurt, Z. & Kazazoğlu, E. Zirconia Dental Implants: A Literature Review. *Journal of Oral Implantology* **37,** 367–376 (June 2010).

18. Bárcena, C., Sra, A. K. & Gao, J. Applications of magnetic nanoparticles in biomedicine. *Nanoscale Magnetic Materials and Applications,* 591–626 (2009).

19. Cloninger, M. J. Biological applications of dendrimers. *Current Opinion in Chemical Biology* **6,** 742–748 (2002).

20. Sapsford, K. E., Algar, W. R., Berti, L., Gemmill, K. B., Casey, B. J., Oh, E., Stewart, M. H. & Medintz, I. L. Functionalizing nanoparticles with biological molecules: Developing chemistries that facilitate nanotechnology. *Chemical Reviews* **113,** 1904–2074 (2013).

21. Thanh, N. T. & Green, L. A. Functionalisation of nanoparticles for biomedical applications. *Nano Today* **5,** 213–230 (2010).

22. Atukorale, P. U., Guven, Z. P., Bekdemir, A., Carney, R. P., Van Lehn, R. C., Yun, D. S., Jacob Silva, P. H., Demurtas, D., Yang, Y.-S., Alexander-Katz, A., Stellacci, F. & Irvine, D. J. Structure–Property Relationships of Amphiphilic Nanoparticles That Penetrate or Fuse Lipid Membranes. *Bioconjugate Chemistry* **29,** 1131–1140 (Apr. 2018).

23. Guven, Z. P., Silva, P. H. J., Luo, Z., Cendrowska, U. B., Gasbarri, M., Jones, S. T. & Stellacci, F. Synthesis and Characterization of Amphiphilic Gold Nanoparticles. *Journal of Visualized Experiments,* e58872 (July 2019).

24. Dahl, J. A., Maddux, B. L. S. & Hutchison, J. E. Toward Greener Nanosynthesis. *Chemical Reviews* **107,** 2228–2269 (June 2007).

25. Gupta, A., Moyano, D. F., Parnsubsakul, A., Papadopoulos, A., Wang, L. S., Landis, R. F., Das, R. & Rotello, V. M. Ultrastable and Biofunctionalizable Gold Nanoparticles. *ACS Applied Materials and Interfaces* **8,** 14096–14101 (2016).

26. Suk, J. S., Xu, Q., Kim, N., Hanes, J. & Ensign, L. M. PEGylation as a strategy for improving nanoparticle-based drug and gene delivery. *Advanced Drug Delivery Reviews* **99,** 28–51 (2016).

27. Williams, D. F. There is no such thing as a biocompatible material. *Biomaterials* **35,** 10009–10014 (2014).

28. Nel, A. E., Mädler, L., Velegol, D., Xia, T., Hoek, E. M., Somasundaran, P., Klaessig, F., Castranova, V. & Thompson, M. Understanding biophysicochemical interactions at the nano-bio interface. *Nature Materials* **8,** 543–557 (2009).

29. Yan, N., Xia, N., Liao, L., Zhu, M., Jin, F., Jin, R. & Wu, Z. Unraveling the long-pursued Au144 structure by x-ray crystallography. *Science Advances* **4,** eaat7259 (2018).

30. Rodriguez-Quijada, C., Sánchez-Purrà, M., De Puig, H. & Hamad-Schifferli, K. Physical Properties of Biomolecules at the Nanomaterial Interface. *Journal of Physical Chemistry B* **122,** 2827–2840 (2018).

31. Tsoi, K. M., MacParland, S. A., Ma, X.-Z., Spetzler, V. N., Echeverri, J., Ouyang, B., Fadel, S. M., Sykes, E. A., Goldaracena, N., Kaths, J. M., Conneely, J. B., Alman, B. A., Selzner, M., Ostrowski, M. A., Adeyi, O. A., Zilman, A., McGilvray, I. D. & Chan, W. C. W. Mechanism of hard-nanomaterial clearance by the liver. *Nature Materials* **15,** 1212–1221 (2016).

32. Yu, M., Song, W., Tian, F., Dai, Z., Zhu, Q., Ahmad, E., Guo, S., Zhu, C., Zhong, H., Yuan, Y., Zhang, T., Yi, X., Shi, X., Gan, Y. & Gao, H. Temperature- and rigidity-mediated rapid transport of lipid nanovesicles in hydrogels. *Proceedings of the National Academy of Sciences* **116,** 5362 LP –5369 (Mar. 2019).

33. Wagener, P., Jakobi, J., Rehbock, C., Chakravadhanula, V. S. K., Thede, C., Wiedwald, U., Bartsch, M., Kienle, L. & Barcikowski, S. Solvent-surface interactions control the phase structure in laser-generated iron-gold core-shell nanoparticles. *Scientific Reports* **6,** 23352 (2016).

34. Zheng, X.-Y., Zhao, K., Tang, J., Wang, X.-Y., Li, L.-D., Chen, N.-X., Wang, Y.-J., Shi, S., Zhang, X., Malaisamy, S., Sun, L.-D., Wang, X., Chen, C. & Yan, C.-H. Gd-Dots with Strong Ligand–Water Interaction for Ultrasensitive Magnetic Resonance Renography. *ACS Nano* **11,** 3642–3650 (Apr. 2017).

35. Yamanaka, T., De Nicola, A., Munaò, G., Soares, T. A. & Milano, G. Effect of the ligand's bulkiness on the shape of functionalized gold nanoparticles in aqueous solutions: A molecular dynamics study. *Chemical Physics Letters* **731,** 136576 (2019).

36. Tascini, A. S., Chiavazzo, E., Fasano, M., Asinari, P. & Bresme, F. Thermal transport across nanoparticle – fluid interfaces : the interplay of interfacial curvature and nanoparticle – fluid interactions †. *Physical Chemistry Chemical Physics* **19,** 3244–3253 (2017).

37. Soussi, J., Volz, S., Palpant, B. & Chalopin, Y. A detailed microscopic study of the heat transfer at a water gold interface coated with a polymer. *Applied Physics Letters* **106** (2015).

38. Baffou, G. & Rigneault, H. Femtosecond-pulsed optical heating of gold nanoparticles. *Physical Review B - Condensed Matter and Materials Physics* **84,** 1–13 (2011).

39. Lynch, I., Cedervall, T., Lundqvist, M., Cabaleiro-Lago, C., Linse, S. & Dawson, K. A. The nanoparticle-protein complex as a biological entity; a complex fluids and surface science challenge for the 21st century. *Advances in Colloid and Interface Science* **134-135,** 167–174 (2007).

40. You, C.-C., Chompoosor, A. & Rotello, V. M. The biomacromolecule-nanoparticle interface. *Nano Today* **2,** 34–43 (2007).

41. Monopoli, M. P., Åberg, C., Salvati, A. & Dawson, K. A. Biomolecular coronas provide the biological identity of nanosized materials. *Nature Nanotechnology* **7,** 779–786 (Dec. 2012).

42. Kitano, H., Mori, T., Takeuchi, Y., Tada, S., Gemmei-Ide, M., Yokoyama, Y. & Tanaka, M. Structure of Water Incorporated in Sulfobetaine Polymer Films as Studied by ATR-FTIR. *Macromolecular Bioscience* **5,** 314–321 (Apr. 2005).

43. Moyano, D. F., Saha, K., Prakash, G., Yan, B., Kong, H., Yazdani, M. & Rotello, V. M. Fabrication of Corona-Free Nanoparticles with Tunable Hydrophobicity. *ACS nano* **8,** 6748–6755 (2014).

44. Simonelli, F., Rossi, G. & Monticelli, L. Role of Ligand Conformation on Nanoparticle-Protein Interactions. *Journal of Physical Chemistry B* **123,** 1764–1769 (2019).

45. Abdelkhaliq, A., van der Zande, M., Punt, A., Helsdingen, R., Boeren, S., Vervoort, J. J. M., Rietjens, I. M. C. M. & Bouwmeester, H. Impact of nanoparticle surface functionalization on the protein corona and cellular adhesion, uptake and transport. *Journal of Nanobiotechnology* **16,** 70 (Dec. 2018).

46. Nakamura, H. & Watano, S. Direct permeation of nanoparticles across cell membrane: A review. *KONA Powder and Particle Journal* **2018,** 49–65 (2018).

47. Van Lehn, R. C., Atukorale, P. U., Carney, R. P., Yang, Y.-S., Stellacci, F., Irvine, D. J. & Alexander-Katz, A. Effect of Particle Diameter and Surface Composition on the Spontaneous Fusion of Monolayer-Protected Gold Nanoparticles with Lipid Bilayers. *Nano Letters* **13,** 4060–4067 (2013).

48. Berkowitz, M. *Biomembrane Simulations: Computational Studies of Biological Membranes* ISBN: 9781351060301 (CRC Press, 2019).

49. Sokolova, V., Kozlova, D., Knuschke, T., Buer, J., Westendorf, A. M. & Epple, M. Mechanism of the uptake of cationic and anionic calcium phosphate nanoparticles by cells. *Acta Biomaterialia* **9,** 7527–7535 (2013).

50. Jiang, Y., Huo, S., Mizuhara, T., Das, R., Lee, Y.-W., Hou, S., Moyano, D. F., Duncan, B., Liang, X.-J. & Rotello, V. M. The Interplay of Size and Surface Functionality on the Cellular Uptake of Sub-10 nm Gold Nanoparticles. *ACS Nano* **9,** 9986–9993 (Oct. 2015).

51. Verma, A., Uzun, O., Hu, Y., Hu, Y., Han, H.-S., Watson, N., Chen, S., Irvine, D. J. & Stellacci, F. Surface-structure-regulated cell-membrane penetration by monolayer-protected nanoparticles. *Nature Materials* **7,** 588–595 (2008).

52. Sabella, S., Carney, R. P., Brunetti, V., Malvindi, M. A., Al-Juffali, N., Vecchio, G., Janes, S. M., Bakr, O. M., Cingolani, R., Stellacci, F. & Pompa, P. P. A general mechanism for intracellular toxicity of metal-containing nanoparticles. *Nanoscale* **6,** 7052–61 (2014).

53. Goodman, C. M., McCusker, C. D., Yilmaz, T. & Rotello, V. M. Toxicity of Gold Nanoparticles Functionalized with Cationic and Anionic Side Chains. *Bioconjugate Chemistry* **15,** 897–900 (July 2004).

54. Leroueil, P. R., Berry, S. A., Duthie, K., Han, G., Rotello, V. M., McNerny, D. Q., Baker, J. R., Orr, B. G. & Banaszak Holl, M. M. Wide Varieties of Cationic Nanoparticles Induce Defects in Supported Lipid Bilayers. *Nano Letters* **8,** 420–424 (Feb. 2008).

55. Feng, Z. V., Gunsolus, I. L., Qiu, T. A., Hurley, K. R., Nyberg, L. H., Frew, H., Johnson, K. P., Vartanian, A. M., Jacob, L. M., Lohse, S. E., Torelli, M. D., Hamers, R. J., Murphy, C. J. & Haynes, C. L. Impacts of gold nanoparticle charge and ligand type on surface binding and toxicity to Gram-negative and Gram-positive bacteria. *Chem. Sci.* **6,** 5186–5196 (2015).

56. Bedrov, D., Smith, G. D., Davande, H. & Li, L. Passive Transport of C 60 Fullerenes through a Lipid Membrane: A Molecular Dynamics Simulation Study. *The Journal of Physical Chemistry B* **112,** 2078–2084 (Feb. 2008).

57. Wong-Ekkabut, J., Baoukina, S., Triampo, W., Tang, I. M., Tieleman, D. P. & Monticelli, L. Computer simulation study of fullerene translocation through lipid membranes. *Nature Nanotechnology* **3,** 363–368 (2008).

58. Wang, J., Zhang, L., Peng, F., Shi, X. & Leong, D. T. Targeting Endothelial Cell Junctions with Negatively Charged Gold Nanoparticles. *Chemistry of Materials* **30,** 3759–3767 (June 2018).

59. Wang, X., Wang, X., Bai, X., Yan, L., Liu, T., Wang, M., Song, Y., Hu, G., Gu, Z., Miao, Q. & Chen, C. Nanoparticle Ligand Exchange and Its Effects at the Nanoparticle–Cell Membrane Interface. *Nano Letters* **19,** 8–18 (Jan. 2019).

60. Xi, A. & Bothun, G. D. Centrifugation-based assay for examining nanoparticle–lipid membrane binding and disruption. *Analyst* **139,** 973–981 (2014).

61. Canepa, E., Salassi, S., De Marco, A. L., Lambruschini, C., Odino, D., Bochicchio, D., Canepa, F., Canale, C., Dante, S., Brescia, R., Stellacci, F., Rossi, G. & Relisi, A. *Anionic gold nanoparticles perturb phase separation and form ordered supramolecular aggregates in multidomain lipid membranes* (unpublished).

62. Tiwari, A., Prince, A., Arakha, M., Jha, S. & Saleem, M. Passive membrane penetration by ZnO nanoparticles is driven by the interplay of electrostatic and phase boundary conditions. *Nanoscale* **10,** 3369–3384 (2018).

63. Luchini, A., Gerelli, Y., Fragneto, G., Nylander, T., Pálsson, G. K., Appavou, M.-S. & Paduano, L. Neutron Reflectometry reveals the interaction between functionalized SPIONs and the surface of lipid bilayers. *Colloids and Surfaces B: Biointerfaces* **151,** 76–87 (2017).

64. Lee, S.-M., Kim, H. J., Kim, S. Y., Kwon, M.-K., Kim, S., Cho, A., Yun, M., Shin, J.-S. & Yoo, K.-H. Drug-loaded gold plasmonic nanoparticles for treatment of multidrug resistance in cancer. *Biomaterials* **35,** 2272–2282 (Feb. 2014).

65. Huang, X., Xu, Z., Mao, Y., Ji, Y., Xu, H., Xiong, Y. & Li, Y. Gold nanoparticle-based dynamic light scattering immunoassay for ultrasensitive detection of Listeria monocytogenes in lettuces. *Biosensors and Bioelectronics* **66,** 184–190 (Apr. 2015).

66. Giner-Casares, J. J., Henriksen-Lacey, M., Coronado-Puchau, M. & Liz-Marzán, L. M. Inorganic nanoparticles for biomedicine: where materials scientists meet medical research. *Materials Today* **19,** 19–28 (Jan. 2016).

67. Riley, R. S. & Day, E. S. Gold nanoparticle-mediated photothermal therapy: applications and opportunities for multimodal cancer treatment. *Wiley Interdisciplinary Reviews: Nanomedicine and Nanobiotechnology* **9,** e1449 (July 2017).

68. Dykman, L. & Khlebtsov, N. Gold nanoparticles in biomedical applications: Recent advances and perspectives. *Chemical Society Reviews* **41,** 2256–2282 (2012).

69. Dreaden, E. C., Alkilany, A. M., Huang, X., Murphy, C. J. & El-Sayed, M. A. The golden age: gold nanoparticles for biomedicine. *Chemical Society Reviews* **41,** 2740–2779 (2012).

70. Elahi, N., Kamali, M. & Baghersad, M. H. Recent biomedical applications of gold nanoparticles: A review. *Talanta* **184,** 537–556 (2018).

71. Jeong, H. H., Choi, E., Ellis, E. & Lee, T. C. Recent advances in gold nanoparticles for biomedical applications: From hybrid structures to multifunctionality. *Journal of Materials Chemistry B* **7,** 3480–3496 (2019).

72. Lin, L., Wang, M., Peng, X., Lissek, E. N., Mao, Z., Scarabelli, L., Adkins, E., Coskun, S., Unalan, H. E., Korgel, B. A., Liz-Marzán, L. M., Florin, E.-L. & Zheng, Y. Opto-thermoelectric nanotweezers. *Nature Photonics* **12,** 195–201 (2018).

73. Lin, X., Si, T., Wu, Z. & He, Q. Self-thermophoretic motion of controlled assembled micro-/nanomotors. *Physical Chemistry Chemical Physics* **19,** 23606–23613 (2017).

74. Koczula, K. M. & Gallotta, A. Lateral flow assays. *Essays in Biochemistry* **60** (ed Estrela, P.) 111–120 (June 2016).

75. Xiong, R., Raemdonck, K., Peynshaert, K., Lentacker, I., De Cock, I., Demeester, J., De Smedt, S. C., Skirtach, A. G. & Braeckmans, K. Comparison of gold nanoparticle mediated photoporation: vapor nanobubbles outperform direct heating for delivering macromolecules in live cells. *ACS nano* **8,** 6288–96 (June 2014).

76. Xiong, R., Samal, S. K., Demeester, J., Skirtach, A. G., De Smedt, S. C. & Braeckmans, K. Laser-assisted photoporation: fundamentals, technological advances and applications. *Advances in Physics: X* **1,** 596–620 (2016).

77. Teirlinck, E., Xiong, R., Brans, T., Forier, K., Fraire, J., Van Acker, H., Matthijs, N., De Rycke, R., De Smedt, S. C., Coenye, T. & Braeckmans, K. Laser-induced vapour nanobubbles improve drug diffusion and efficiency in bacterial biofilms. *Nature Communications* **9,** 1–12 (2018).

78. Lajunen, T., Viitala, L., Kontturi, L.-S., Laaksonen, T., Liang, H., Vuorimaa-Laukkanen, E., Viitala, T., Guével, X. L., Yliperttula, M., Murtomäki, L. & Urtti, A. Light induced cytosolic drug delivery from liposomes with gold nanoparticles. *Journal of Controlled Release* **203,** 85–98 (2015).

79. Molina, M., Asadian-Birjand, M., Balach, J., Bergueiro, J., Miceli, E. & Calderón, M. Stimuli-responsive nanogel composites and their application in nanomedicine. *Chemical Society Reviews* **44,** 6161–6186 (2015).

80. Cormier, S., Ding, T., Turek, V. & Baumberg, J. J. Dynamic- and Light-Switchable Self-Assembled Plasmonic Metafilms. *Advanced Optical Materials* **6,** 1800208 (July 2018).

81. Goodman, A. M., Hogan, N. J., Gottheim, S., Li, C., Clare, S. E. & Halas, N. J. Understanding Resonant Light-Triggered DNA Release from Plasmonic Nanoparticles. *ACS Nano* **11,** 171–179 (Jan. 2017).

82. Tuckerman, M. *Statistical Mechanics: Theory and Molecular Simulation* ISBN: 9780191523465 (OUP Oxford, 2010).

83. Leach, A. R. *Molecular Modelling: Principles and Applications* ISBN: 9780582382107 (Prentice Hall, 2001).

84. Frenkel, D. & Smit, B. *Understanding Molecular Simulation: From Algorithms to Applications* ISBN: 9780080519982 (Elsevier Science, 2001).

85. Allen, M. & Tildesley, D. *Computer Simulation of Liquids* ISBN: 9780198556459 (Clarendon Press, 1989).

86. Bussi, G., Donadio, D. & Parrinello, M. Canonical sampling through velocity rescaling. *The Journal of Chemical Physics* **126** (2007).

87. Hoover, W. G. Canonical dynamics: Equilibrium phase-space distributions. *Physical Review A* **31,** 1695–1697 (Mar. 1985).

88. Berendsen, H. J. C., Postma, J. P. M., Van Gunsteren, W. F., DiNola, A. & Haak, J. R. Molecular dynamics with coupling to an external bath. *The Journal of Chemical Physics* **81,** 3684 (1984).

89. Parrinello, M. & Rahman, A. Crystal Structure and Pair Potentials: A Molecular-Dynamics Study. *Phys. Rev. Lett.* **45,** 1196–1199 (14 Oct. 1980).

90. Parrinello, M. & Rahman, A. Polymorphic transitions in single crystals: A new molecular dynamics method. *Journal of Applied Physics* **52,** 7182–7190 (1981).

91. Abraham, M. J., Murtola, T., Schulz, R., Páll, S., Smith, J. C., Hess, B. & Lindah, E. Gromacs: High performance molecular simulations through multi-level parallelism from laptops to supercomputers. *SoftwareX* **1-2,** 19–25 (2015).

92. Laio, A. & Parrinello, M. Escaping free-energy minima. *Proceedings of the National Academy of Sciences* **99,** 12562–12566 (2002).

93. Laio, A. & Gervasio, F. L. Metadynamics: a method to simulate rare events and reconstruct the free energy in biophysics, chemistry and material science. *Reports on Progress in Physics* **71,** 126601 (2008).

94. Kästner, J. Umbrella sampling. *Wiley Interdisciplinary Reviews: Computational Molecular Science* **1,** 932–942 (2011).

95. Sugita, Y. & Okamoto, Y. Replica-exchange molecular dynamics method for protein folding. *Chemical Physics Letters* **314,** 141–151 (1999).

96. Grubmüller, H., Heymann, B. & Tavan, P. Ligand Binding: Molecular Mechanics Calculation of the Streptavidin-Biotin Rupture Force. *Science* **271,** 997–999. eprint: https://science.sciencemag.org/content/271/5251/997.full.pdf (1996).

97. Jarzynski, C. Nonequilibrium Equality for Free Energy Differences. *Phys. Rev. Lett.* **78,** 2690–2693 (14 Apr. 1997).

98. Tribello, G. A., Bonomi, M., Branduardi, D., Camilloni, C. & Bussi, G. PLUMED 2: New feathers for an old bird. *Computer Physics Communications* **185,** 604–613 (2014).

99. Marrink, S. J., Risselada, H. J., Yefimov, S., Tieleman, D. P. & de Vries†, A. H. The MARTINI Force Field: Coarse Grained Model for Biomolecular Simulations. *The Journal of Physical Chemistry B* **111,** 7812–7824 (2007).

100. Ewals, P. Die Berechnung optischer und elektrostatischer Gitterpotentiale. *Annalen der Physik* **369.3,** 253–287 (1921).

101. Darden, T., York, D. & Pedersen, L. Particle mesh Ewald: An $N \cdot \ln(N)$ method for Ewald sums in large systems. *The Journal of Chemical Physics* **98,** 10089–10092 (1993).

102. Essmann, U., Perera, L., Berkowitz, M. L., Darden, T., Lee, H. & Pedersen, L. G. A smooth particle mesh Ewald method. *The Journal of Chemical Physics* **103,** 8577–8593 (1995).

103. Cisneros, G. A., Karttunen, M., Ren, P. & Sagui, C. Classical Electrostatics for Biomolecular Simulations. *Chemical Reviews* **114,** 779–814 (2014).

104. Jorgensen, W. L., Madura, J. D. & Swenson, C. J. Optimized Intermolecular Potential Functions for Liquid Hydrocarbons. *Journal of the American Chemical Society* **106,** 6638–6646 (1984).

105. Jorgensen, W. L. & Tirado-Rives, J. The OPLS [optimized potentials for liquid simulations] potential functions for proteins, energy minimizations for crystals of cyclic peptides and crambin. *Journal of the American Chemical Society* **110,** 1657–1666 (Mar. 1988).

106. Berger, O., Edholm, O. & Jähnig, F. Molecular dynamics simulations of a fluid bilayer of dipalmitoylphosphatidylcholine at full hydration, constant pressure, and constant temperature. *Biophysical Journal* **72,** 2002–2013 (1997).

107. Tieleman, D. P., MacCallum, J. L., Ash, W. L., Kandt, C., Xu, Z. & Monticelli, L. Membrane protein simulations with a united-atom lipid and all-atom protein model: lipid–protein interactions, side chain transfer free energies and model proteins. *Journal of Physics: Condensed Matter* **18,** S1221–S1234 (June 2006).

108. Weiner, S. J., Kollman, P. A., Case, D. A., Singh, U. C., Ghio, C., Alagona, G. G. G., Profeta, S., Weiner, P., Weinerl, P. & Weiner, P. A new force field for molecular mechanical simulation of nucleic acids and proteins. *Journal of the American Chemical Society* **106,** 765–784 (Feb. 1984).

109. Cornell, W. D., Cieplak, P., Bayly, C. I., Gould, I. R., Merz, K. M., Ferguson, D. M., Spellmeyer, D. C., Fox, T., Caldwell, J. W. & Kollman, P. A. A Second Generation Force Field for the Simulation of Proteins, Nucleic Acids, and Organic Molecules. *Journal of the American Chemical Society* **117,** 5179–5197 (1995).

110. Berendsen, H. J., Grigera, J. R. & Straatsma, T. P. The missing term in effective pair potentials. *Journal of Physical Chemistry* **91,** 6269–6271 (1987).

111. Hess, B., Bekker, H., Berendsen, H. J. C. & Fraaije, J. G. E. M. LINCS: A linear constraint solver for molecular simulations. *Journal of Computational Chemistry* **18,** 1463–1472 (Sept. 1997).

112. iGem. *Membrane Modeling for XylE-transporter* http://2015.igem.org/Team:TU_Darmstadt/Project/Bio/Modeling/sec3.

113. Monticelli, L., Kandasamy, S. K., Periole, X., Larson, R. G., Tieleman, D. P. & Marrink, S.-J. The MARTINI Coarse-Grained Force Field: Extension to Proteins. *Journal of Chemical Theory and Computation* **4,** 819–834 (2008).

114. Periole, X., Cavalli, M., Marrink, S. J. & Ceruso, M. A. Combining an elastic network with a coarse-grained molecular force field: Structure, dynamics, and intermolecular recognition. *Journal of Chemical Theory and Computation* **5,** 2531–2543 (2009).

115. De Jong, D. H., Singh, G., Bennett, W. F., Arnarez, C., Wassenaar, T. A., Schäfer, L. V., Periole, X., Tieleman, D. P. & Marrink, S. J. Improved parameters for the martini coarse-grained protein force field. *Journal of Chemical Theory and Computation* **9,** 687–697. eprint: nn504795v (10.1021) (2013).

116. López, C. A., Rzepiela, A. J., de Vries, A. H., Dijkhuizen, L., Hünenberger, P. H. & Marrink, S. J. Martini Coarse-Grained Force Field: Extension to Carbohydrates. *Journal of Chemical Theory and Computation* **5,** 3195–3210 (2009).

117. Rossi, G., Monticelli, L., Puisto, S. R., Vattulainen, I. & Ala-Nissila, T. Coarse-graining polymers with the MARTINI force-field: polystyrene as a benchmark case. *Soft Matter* **7,** 698–708 (2 2011).

118. Marrink, S. J. & Tieleman, D. P. Perspective on the Martini model. *Chem. Soc. Rev.* **42,** 6801–6822 (16 2013).

119. Yesylevskyy, S. O., Schäfer, L. V., Sengupta, D. & Marrink, S. J. Polarizable Water Model for the Coarse-Grained MARTINI Force Field. *PLoS Comput Biol* **6,** 1–17 (June 2010).

120. Bereau, T. & Kremer, K. Automated Parametrization of the Coarse-Grained Martini Force Field for Small Organic Molecules. *Journal of Chemical Theory and Computation* **11,** 2783–2791. eprint: nn504795v (10.1021) (2015).

121. Bruininks, B. M. H., Souza, P. C. T. & Marrink, S. J. in *Biomolecular Simulations: Methods and Protocols* (eds Bonomi, M. & Camilloni, C.) 105–127 (Springer New York, New York, NY, 2019). ISBN: 978-1-4939-9608-7.

122. Alessandri, R., Souza, P. C., Thallmair, S., Melo, M. N., De Vries, A. H. & Marrink, S. J. Pitfalls of the Martini Model. *Journal of Chemical Theory and Computation* **15,** 5448–5460 (2019).

123. Simonelli, F., Bochicchio, D., Ferrando, R. & Rossi, G. Monolayer–Protected Anionic Au Nanoparticles Walk into Lipid Membranes Step by Step. *The Journal of Physical Chemistry Letters* **6,** 3175–3179 (2015).

124. Salassi, S., Simonelli, F., Bochicchio, D., Ferrando, R. & Rossi, G. Au Nanoparticles in Lipid Bilayers: A Comparison between Atomistic and Coarse-Grained Models. *Journal of Physical Chemistry C* **121,** 10927–10935 (May 2017).

125. Torchi, A., Simonelli, F., Ferrando, R. & Rossi, G. Local Enhancement of Lipid Membrane Permeability Induced by Irradiated Gold Nanoparticles. *ACS Nano* **11,** 12553–12561 (2017).

126. Salassi, S., Canepa, E., Ferrando, R. & Rossi, G. Anionic nanoparticle-lipid membrane interactions: the protonation of anionic ligands at the membrane surface reduces membrane disruption. *RSC Advances* **9,** 13992–13997 (2019).

127. Lopez-Acevedo, O., Akola, J., Whetten, R. L., Grönbeck, H. & Häkkinen, H. Structure and Bonding in the Ubiquitous Icosahedral Metallic Gold Cluster $Au_{144}(SR)_{60}$. *The Journal of Physical Chemistry C* **113,** 5035–5038 (2009).

128. Häkkinen, H. The gold–sulfur interface at the nanoscale. *Nature Chemistry* **4,** 443–455 (2012).

129. Pohjolainen, E., Chen, X., Malola, S., Groenhof, G. & Häkkinen, H. A Unified AMBER-Compatible Molecular Mechanics Force Field for Thiolate-Protected Gold Nanoclusters. *Journal of Chemical Theory and Computation* **12,** 1342–1350 (2016).

130. Tero, T.-R., Malola, S., Koncz, B., Pohjolainen, E., Lautala, S., Mustalahti, S., Permi, P., Groenhof, G., Pettersson, M. & Häkkinen, H. Dynamic Stabilization of the Ligand–Metal Interface in Atomically Precise Gold Nanoclusters Au68 and Au144 Protected by meta-Mercaptobenzoic Acid. *ACS Nano* **11,** 11872–11879 (Dec. 2017).

131. Yeagle, P. *The Membranes of Cells* ISBN: 9780128004869 (Elsevier Science, 2016).

132. Brust, M., Walker, M., Bethell, D., Schiffrin, D. J. & Whyman, R. Synthesis of thiol-derivatised gold nanoparticles in a two-phase Liquid–Liquid system. *Journal of the Chemical Society, Chemical Communications,* 801–802 (1994).

133. Sardar, R., Funston, A. M., Mulvaney, P. & Murray, R. W. Gold Nanoparticles: Past, Present, and Future. *Langmuir* **25,** 13840–13851 (Dec. 2009).

134. Jin, R. Quantum sized, thiolate-protected gold nanoclusters. *Nanoscale* **2,** 343–362 (2010).

135. Tsukuda, T. Toward an Atomic-Level Understanding of Size-Specific Properties of Protected and Stabilized Gold Clusters. *Bulletin of the Chemical Society of Japan* **85,** 151–168 (Feb. 2012).

136. Heinz, H., Vaia, R. A., Farmer, B. L. & Naik, R. R. Accurate simulation of surfaces and interfaces of FCC metals using 12–6 and 9–6 Lennard-Jones potentials. *Journal of Physical Chemistry* **112,** 17281 (2008).

137. Gupta, R. P. Lattice relaxation at a metal surface. *Physical Review B* **23,** 6265–6270 (June 1981).

138. Ferrando, R., Jellinek, J. & Johnston, R. L. Nanoalloys: From Theory to Applications of Alloy Clusters and Nanoparticles. *Chemical Reviews* **108,** 845–910 (2008).

139. Hautman, J. & Klein, M. L. Simulation of a monolayer of alkyl thiol chains. *The Journal of Chemical Physics* **91,** 4994–5001 (1989).

140. Jorgensen, W. L., Maxwell, D. S. & Tirado-Rives, J. Development and testing of the OPLS all-atom force field on conformational energetics and properties of organic liquids. *Journal of the American Chemical Society* **118,** 11225–11236 (1996).

141. Canongia Lopes, J. N., Pádua, A. A. & Shimizu, K. Molecular force field for ionic liquids IV: Trialkylimidazolium and alkoxycarbonyl-imidazolium cations; alkylsulfonate and alkylsulfate anions. *Journal of Physical Chemistry B* **112,** 5039–5046 (2008).

142. Fuchs, P. F., Hansen, H. S., Hünenberger, P. H. & Horta, B. A. A GROMOS parameter set for vicinal diether functions: Properties of polyethyleneoxide and polyethyleneglycol. *Journal of Chemical Theory and Computation* **8,** 3943–3963 (2012).

143. Fischer, J., Paschek, D., Geiger, A. & Sadowski, G. Modeling of aqueous poly (oxyethylene) solutions: 1. Atomistic simulations. *The Journal of Physical Chemistry B* **112,** 2388–2398 (2008).

144. Kawaguchi, S., Imai, G., Suzuki, J., Miyahara, A., Kitano, T. & Ito, K. Aqueous solution properties of oligo- and poly(ethylene oxide) by static light scattering and intrinsic viscosity. *Polymer* **38,** 2885–2891 (1997).

145. Tatur, S., Maccarini, M., Barker, R., Nelson, A. & Fragneto, G. Effect of Functionalized Gold Nanoparticles on Floating Lipid Bilayers. *Langmuir* **29,** 6606–6614 (2013).

146. Van Lehn, R. C., Ricci, M., Silva, P. H. J., Andreozzi, P., Reguera, J., Voïtchovsky, K., Stellacci, F. & Alexander-Katz, A. Lipid tail protrusions mediate the insertion of nanoparticles into model cell membranes. *Nature communications* **5,** 4482 (2014).

147. Van Lehn, R. C. & Alexander-Katz, A. Pathway for insertion of amphiphilic nanoparticles into defect-free lipid bilayers from atomistic molecular dynamics simulations. *Soft Matter* **11,** 3165–3175 (2015).

148. Marrink, S. J., Corradi, V., Souza, P. C., Ingólfsson, H. I., Tieleman, D. P. & Sansom, M. S. Computational Modeling of Realistic Cell Membranes. *Chemical Reviews* **119,** 6184–6226 (2019).

149. Rossi, G., Barnoud, J. & Monticelli, L. Polystyrene nanoparticles perturb lipid membranes. *Journal of Physical Chemistry Letters* **5,** 241–246 (2014).

150. Vijay-Kumar, S., Bugg, C. E. & Cook, W. J. Structure of ubiquitin refined at 1.8 Å resolution. *Journal of Molecular Biology* **194,** 531–544 (1987).

151. Javanainen, M., Martinez-Seara, H. & Vattulainen, I. Excessive aggregation of membrane proteins in the Martini model. *PLoS ONE* **12,** 1–20 (2017).

152. Mieszawska, A. J., Mulder, W. J. M., Fayad, Z. A. & Cormode, D. P. Multifunctional Gold Nanoparticles for Diagnosis and Therapy of Disease. *Molecular Pharmaceutics* **10,** 831–847 (2013).

153. Kriegel, I., Scotognella, F. & Manna, L. Plasmonic doped semiconductor nanocrystals: Properties, fabrication, applications and perspectives. *Physics Reports* **674.** Plasmonic Doped Semiconductor Nanocrystals: Properties, Fabrication, Applications and Perspectives, 1–52 (2017).

154. Keblinski, P., Cahill, D. G., Bodapati, A., Sullivan, C. R. & Taton, T. A. Limits of localized heating by electromagnetically excited nanoparticles. *Journal of Applied Physics* **100** (2006).

155. Riedinger, A., Guardia, P., Curcio, A., Garcia, M. A., Cingolani, R., Manna, L. & Pellegrino, T. Subnanometer local temperature probing and remotely controlled drug release based on Azo-functionalized iron oxide nanoparticles. *Nano Letters* **13,** 2399–2406 (2013).

156. Zhang, T., Sun, F., Guo, Z., Tang, D., Zheng, Z., Ptasinska, S., Zhang, X., Jobbins, M. M. & Luo, T. Molecular Bridge Enables Anomalous Enhancement in Thermal Transport across Hard-Soft Material Interfaces. *Advanced Materials* **26,** 6093–6099 (2014).

157. Hannah, D. C., Gezelter, J. D., Schaller, R. D. & Schatz, G. C. Reverse Non-Equilibrium Molecular Dynamics Demonstrate That Surface Passivation Controls Thermal Transport at Semiconductor-Solvent Interfaces. *ACS Nano* **9,** 6278–6287 (2015).

158. Ge, Z., Cahill, D. G. & Braun, P. V. Thermal conductance of hydrophilic and hydrophobic interfaces. *Physical Review Letters* **96,** 1–4 (2006).

159. Losego, M. D., Grady, M. E., Sottos, N. R., Cahill, D. G. & Braun, P. V. Effects of chemical bonding on heat transport across interfaces. *Nature materials* **11,** 502–6 (2012).

160. Park, J. & Cahill, D. G. Plasmonic Sensing of Heat Transport at Solid-Liquid Interfaces. *Journal of Physical Chemistry C* **120,** 2814–2821 (2016).

161. Patel, H. A., Garde, S. & Keblinski, P. Thermal resistance of nanoscopic liquid-liquid interfaces: Dependence on chemistry and molecular architecture. *Nano Letters* **5,** 2225–2231 (2005).

162. Alexeev, D., Chen, J., Walther, J. H., Giapis, K. P., Angelikopoulos, P. & Koumoutsakos, P. Kapitza Resistance between Few-Layer Graphene and Water: Liquid Layering Effects. *Nano Letters* **15,** 5744–5749 (2015).

163. Huang, D., Ma, R., Zhang, T. & Luo, T. Origin of Hydrophilic Surface Functionalization-Induced Thermal Conductance Enhancement across Solid–Water Interfaces. *ACS Applied Materials & Interfaces* **10,** 28159–28165 (Aug. 2018).

164. Zhang, T., Gans-Forrest, A. R., Lee, E., Zhang, X., Qu, C., Pang, Y., Sun, F. & Luo, T. Role of Hydrogen Bonds in Thermal Transport across Hard/Soft Material Interfaces. *ACS Applied Materials & Interfaces* **8,** 33326–33334 (Dec. 2016).

165. Stocker, K. M., Neidhart, S. M. & Gezelter, J. D. Interfacial thermal conductance of thiolate-protected gold nanospheres. *Journal of Applied Physics* **119** (2016).

166. Ferrando, R. & Baletto, F. Structural properties of nanoclusters: Energetic, thermodynamic, and kinetic effects. *Reviews of Modern Physics* **77,** 371–423 (2005).

167. Hung, S. W., Kikugawa, G. & Shiomi, J. Mechanism of temperature dependent thermal transport across the interface between self-assembled monolayer and water. *Journal of Physical Chemistry C* **120,** 26678–26685 (2016).

168. Chiavazzo, E., Fasano, M., Asinari, P. & Decuzzi, P. Scaling behaviour for the water transport in nanoconfined geometries. *Nature Communications* **5,** 1–11 (2014).

169. Swartz, E. T. & Pohl, R. O. Thermal boundary resistance. *Reviews of Modern Physics* **61,** 605–668 (July 1989).

170. Chen, X., Munjiza, A., Zhang, K. & Wen, D. Molecular Dynamics Simulation of Heat Transfer from a Gold Nanoparticle to a Water Pool. *The journal of physical chemistry. C* **118,** 1285–1293 (2014).

171. Kuang, S. & Gezelter, J. D. Simulating interfacial thermal conductance at metal-solvent interfaces: The role of chemical capping agents. *Journal of Physical Chemistry C* **115,** 22475–22483 (2011).

172. Cardellini, A., Fasano, M., Chiavazzo, E. & Asinari, P. Interfacial water thickness at inorganic nanoconstructs and biomolecules: Size matters. *Physics Letters A* **380,** 1735–1740 (Apr. 2016).

173. *BioMembNP repository* `https://bitbucket.org/biomembnp/biomembnp`.

174. Luzar, A. Resolving the hydrogen bond dynamics conundrum. *Journal of Chemical Physics* **113,** 10663–10675 (2000).

175. Voloshin, V. P. & Naberukhin, Y. I. Hydrogen bond lifetime distributions in computer-simulated water. *Journal of Structural Chemistry* **50,** 78–89 (Feb. 2009).

176. Pascal, T. A., Lin, S. T. & Goddard, W. A. Thermodynamics of liquids: Standard molar entropies and heat capacities of common solvents from 2PT molecular dynamics. *Physical Chemistry Chemical Physics* **13,** 169–181 (2011).

177. Lin, S. T., Blanco, M. & Goddard, W. A. The two-phase model for calculating thermodynamic properties of liquids from molecular dynamics: Validation for the phase diagram of Lennard-Jones fluids. *Journal of Chemical Physics* **119,** 11792–11805 (2003).

178. Heikkilä, E., Martinez-Seara, H., Gurtovenko, A. A., Vattulainen, I. & Akola, J. Atomistic simulations of anionic $Au_{144}(SR)_{60}$ nanoparticles interacting with asymmetric model lipid membranes. *Biochimica et Biophysica Acta - Biomembranes* **1838,** 2852–2860 (2014).

179. Van Lehn, R. C. & Alexander-katz, A. Energy landscape for the insertion of amphiphilic nanoparticles into lipid membranes : A computational study. *PloS one* **14,** e0209492 (2019).

180. Gkeka, P., Angelikopoulos, P., Sarkisov, L. & Cournia, Z. Membrane Partitioning of Anionic, Ligand-Coated Nanoparticles Is Accompanied by Ligand Snorkeling, Local Disordering, and Cholesterol Depletion. *PLoS Computational Biology* **10** (2014).

181. Khavrutskii, I. V., Gorfe, A. A., Lu, B. & McCammon, J. A. Free Energy for the Permeation of Na^+ and Cl^- Ions and Their Ion–Pair through a Zwitterionic Dimyristoyl Phosphatidylcholine Lipid Bilayer by Umbrella Integration with Harmonic Fourier Beads. *Journal of the American Chemical Society* **131,** 1706–1716 (2009).

182. De Jong, D. H., Baoukina, S., Ingólfsson, H. I. & Marrink, S. J. Martini straight: Boosting performance using a shorter cutoff and GPUs. *Computer Physics Communications* **199,** 1–7 (Feb. 2016).

183. Moglianetti, M., Ponomarev, E., Szybowski, M., Stellacci, F. & Reguera, J. Co-precipitation of oppositely charged nanoparticles: the case of mixed ligand nanoparticles. *Journal of Physics D: Applied Physics* **48,** 434001 (Nov. 2015).

184. MacCallum, J. L., Bennett, W. F. D. & Tieleman, D. P. Distribution of amino acids in a lipid bilayer from computer simulations. *Biophysical journal* **94,** 3393–3404 (2008).

185. Koivisto, J., Chen, X., Donnini, S., Lahtinen, T., Häkkinen, H., Groenhof, G. & Pettersson, M. Acid–Base Properties and Surface Charge Distribution of the Water-Soluble Au ₁₀₂ (p MBA) ₄₄ Nanocluster. *The Journal of Physical Chemistry C* **120,** 10041–10050 (2016).

186. Salvati, A., Pitek, A. S., Monopoli, M. P., Prapainop, K., Bombelli, F. B., Hristov, D. R., Kelly, P. M., Åberg, C., Mahon, E. & Dawson, K. A. Transferrin-functionalized nanoparticles lose their targeting capabilities when a biomolecule corona adsorbs on the surface. *Nature Nanotechnology* **8,** 137–143 (2013).

187. Mahmoudi, M., Sheibani, S., Milani, A. S., Rezaee, F., Gauberti, M., Dinarvand, R. & Vali, H. Crucial role of the protein corona for the specific targeting of nanoparticles. *Nanomedicine* **10,** 215–226 (2015).

188. Bekdemir, A., Abriata, L. A. & Stellacci, F. *Protein binding geometry is correlated to local nanoparticles surface but not to global binding constants* (unpublished).

189. Carney, R. P., Kim, J. Y., Qian, H., Jin, R., Mehenni, H., Stellacci, F. & Bakr, O. M. Determination of nanoparticle size distribution together with density or molecular weight by 2D analytical ultracentrifugation. *Nature Communications* **2** (2011).

190. Bekdemir, A. & Stellacci, F. A centrifugation-based physicochemical characterization method for the interaction between proteins and nanoparticles. *Nature Communications* **7,** 1–8 (2016).